The Spaghetti Calorimeter

Research, Development, Application

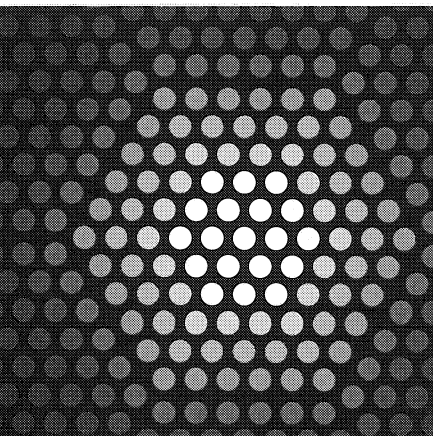

Christine V. Scheel

The Spaghetti Calorimeter

Research, Development, Application

The Spaghetti Calorimeter

Research, Development, Application

ACADEMISCH PROEFSCHRIFT

TER VERKRIJGING VAN DE GRAAD VAN DOCTOR
AAN DE UNIVERSITEIT VAN AMSTERDAM
OP GEZAG VAN DE RECTOR MAGNIFICUS
PROF. DR. P. W. M. DE MEIJER
TEN OVERSTAAN VAN EEN DOOR HET COLLEGE VAN DEKANEN INGESTELDE
COMMISSIE IN HET OPENBAAR TE VERDEDIGEN IN DE AULA DER UNIVERSITEIT
OP DONDERDAG 22 DECEMBER 1994 TE 10:30 UUR

door

Christine Veronica Scheel

geboren te Philadelphia, Pennsylvania, USA

Promotores: Prof. Dr. J.J. Engelen
Prof. Dr. R. Wigmans (Texas Tech University)

Faculteit der Natuur- en Sterrenkunde

The work described in this thesis is part of the research programme of 'het Nationaal Instituut voor Kernfysica en Hoge-Energie Fysica' (NIKHEF-H) in Amsterdam. The author was financially supported by 'de Stichting voor Fundamenteel Onderzoek der Materie' (FOM).

To my parents

Contents

Chapter 1

The Appetizer: Introduction

1.1 Detectors for particle physics experiments

"What does spaghetti have to do with physics?" you may ask. Let me just tell you about it briefly, to whet your appetite for the rest of this thesis.

First, I have to tell you a little bit about particle physics, also called high-energy physics. Matter, the stuff that makes up everything in the universe, can be broken down into smaller and smaller pieces. Galaxies can be broken down into stars and planets, planets can be broken down into different levels from the atmosphere to the core, and each level can be categorized according to its molecular composition. Each molecule can be described by the atoms (the chemical elements) contained within it. An atom, in turn, is made up of a nucleus containing protons and neutrons, surrounded by a cloud of electrons. These are some of the particles that particle physicists want to study. But we have gone even one step deeper, to a world made up of quarks and leptons and the forces that hold them together. So far, these are the smallest constituents of matter that we have evidence for, but they may not be the most basic building blocks of matter. Knowledge about these particles is not only interesting to particle physicists, it also provides cosmologists with clues about the creation of the universe. Going smaller also takes us back in time, to the first moments of the universe before the quarks were bound together into protons, neutrons, and other hadrons.

In order to investigate particles and their behavior, scientists have had to stretch their experimental techniques to the limits. Particle physicists today build machines that accelerate particles (usually protons or electrons) to high speed and energy. By colliding these particles onto stationary particles in a block of material (called a *fixed target*) or into each other (in a *collider*), the combined energy of the particles in the collision works to break them up and to create more uncommon particles. These particles are not the basic ones that make up ordinary atoms (electrons, protons, and neutrons), and they cannot exist for long. They quickly break up (or *decay*) into more stable particles. From the number of produced particles, their masses, and their lifetimes, among other properties, we can learn about *their* constituents, the leptons and the quarks, and how they interact with each other. The best description so far

of how all of these particles fit together and why and how they behave is found in a theory called the Standard Model. Many experiments have been conducted and have confirmed many parts of the Standard Model, but not all of its predictions have been verified. Most importantly, the model has yet not been disproven.

Subatomic particles are too small to be seen by the naked eye, or even with magnification. In order to "see" particles and their movements, many devices have been invented and constructed. They are all based on the interaction of a particle with the construction material, which then produces a detectable (usually visual or electronic) picture of the particle path. Over the years, particle energies have become higher and higher in order to produce more exotic particles, and the rate of the production of these particles has increased in order to collect a larger sample of interactions (called *events*) for study. The particle detectors have also had to be able to respond to these energies and rates, so that today the design of these devices has become a science itself, investigating and implementing basic physics concepts.

Usually, in an experiment, particle physicists use several different detectors, and then combine all the information to determine what kind of particles have been produced. The most common detectors measure the path that a particle travels, in order to reconstruct the collisions and decays. These are called *tracking* detectors. In such a detector, a charged particle interacts with the detector material, which leaves the atoms and molecules ionized, or excited, which can be observed. Another type of detector, called a *calorimeter*, directly measures the energy of a particle as it absorbs it. A calorimeter is composed of a material (usually quite dense and in a large amount) in which a particle produces a shower of more and more particles which leave their energy in the calorimeter in such a way that is observable (usually in the form of light or electric charge). The relation between this *signal* and the energy is known, thus providing a measurement of the original particle's energy. This is analogous to finding the caloric content of food, where one burns the food away to find the heat content, measured in units of calories. In "high energy" particle physics, energy is usually measured in units of giga-electron-volt (GeV), which is only 0.000000000004 calories[1]. In some calorimeters, the energy of the particle is dissipated in the same process that makes the observable signal. Others are made of two types of material: one material with a high density to propagate the interactions and absorb the particle energy and the other to generate the signal. This concept is behind the "spaghetti" calorimeter. It is composed of lead (which is very dense) in which the shower is produced and of many plastic "scintillating" fibers, which produce light when charged particles from the shower pass through it. The amount of light produced gives the energy of the particle. The fibers in this detector are 1 mm in diameter, and when they extend out the end of the lead structure look very much like spaghetti, hence the name. With this detector, all kind of particles, with or without charge, can be detected, making it a very useful detector in a high-energy physics experiment.

[1] This is the calorie as known in the U.S. Elsewhere, the unit giving the same measure is called a kilocalorie.

1.2 Thesis overview

In this thesis, I will describe the construction, testing, and use of the spaghetti calorimeter. It was constructed in order to test the compensating calorimetry principle for the construction of a state-of-the-art calorimeter that is able to achieve excellent hadronic energy resolution. The geometry is unusual, in that it uses scintillating plastic fibers embedded in lead, instead of the more usual structure composed of alternating plates of lead and scintillator. Only electromagnetic calorimeters had previously used this geometry, whereas the spaghetti calorimeter was proposed for the detection of both electromagnetic and hadronic showers. The research was aimed toward eventually building a suitable calorimeter of this type for an experiment at one of the next generation of proton colliders, such as the Superconducting Supercollider (SSC)[2] in Texas and the Large Hadron Collider (LHC) at CERN in Geneva. However, this calorimeter is also useful for other types of experiments, as in the example used in this thesis.

After testing it, the largest spaghetti calorimeter prototype from the research and development project described in this thesis was put into the experiment WA89 at CERN. This is a fixed target experiment at the Σ^- beam coming from Super Proton Synchrotron (SPS). It is intended primarily for the study of charmed baryons, with the study of hyperon resonances and exotic multi-quark states also possible. The experimental apparatus consists basically of tracking detectors, the Omega magnetic spectrometer, a ring-imaging Čerenkov counter for particle identification, and an electromagnetic calorimeter. The spaghetti calorimeter was added for the identification and energy measurement of neutral hadrons, in particular neutrons, which cannot be detected by any of the other detectors. From this measurement, it is possible to find interesting particles that eventually result in a neutron, especially via the decay channels $\Sigma^{\pm} \rightarrow n\pi^{\pm}$. This may include the detection of charmed baryons, hyperon resonances, and the proposed H dibaryon (*e.g.*, $H \rightarrow \Sigma^- p$, then $\Sigma^- \rightarrow n\pi^-$).

Preparing a physics experiment is a little like preparing a meal – a feast, in the case of particle physics, where the apparatus can be as big as a house and the number of people involved can be in the hundreds.

First, you get an idea for the menu, depending on the occasion and the number of people attending. This involves reading many recipes, which are either used directly or inspire a new creation, all relying on the basic cooking skills. It's a similar process for new experiments and detectors, the recipes being physics journals and books, complemented by lectures, colleagues, and experience. The detector should be designed with its purpose in mind. The designer should also know the basic concepts behind the detector. This is the aim of the following chapter, which provides the background on calorimetry, as well as the motivation for the special geometry of the spaghetti calorimeter.

Once the recipe has been proposed, the next step is to collect the necessary ingre-

[2] The SSC project has now been cancelled.

dients, making sure they are the proper ones that will taste and look good in the dish. The basic active ingredient in making the spaghetti calorimeter is the "spaghetti"– plastic scintillating fibers. Chapter 3 describes scintillating fibers with an emphasis on characteristics important for the calorimeter.

If you are preparing a banquet for many people, you would want to try out your recipes ahead of time, to make sure you have the correct ingredients in the right proportions and to learn the specific culinary techniques for this dish. You can do this by preparing it for a smaller amount of people. Only then can you prepare the the real feast. The same applies for a detector, where the first versions for testing are usually much smaller than the final one for the experiment. Small prototypes of the spaghetti calorimeter were built and run in a test beam. From this, we learned how to build better, larger calorimeters in a more efficient way. The final calorimeter was built originally as a prototype and tested as such. In chapter 4, the calorimeter and its performance are presented, the results of more than two years of research and development. The focus is on results relevant to neutron detection in WA89.

Finally, you are ready for the feast. This is the true test: will people enjoy the food and it's presentation? The test of the spaghetti calorimeter here is its placement in the experiment WA89 and the particle physics that can be learned using the information it provides. This is presented in the last chapter, preceded by a short description of the experiment. Then the calibration of the calorimeter with electrons and protons is discussed in detail, as the correct conversion from light to an energy value is crucial. Before using the calorimeter in the search for various decay channels, it was possible to measure the performance for $\Sigma^- \rightarrow n\pi^-$ using the Σ^- particles from the beam that did not interact in the target. It is reconstructed by taking the invariant mass, using the information about the neutron provided by the calorimeter, in addition to information on the π^- and Σ^- provided by the other detectors. Finally, the results are drawn together and discussed, along with a summary of later developments.

Bon Appetit!

Chapter 2

The Recipe: Calorimetry

A calorimeter is an instrumented block of matter that absorbs the energy of a particle and produces a related signal, thus providing a measure of this energy. Typically several mechanisms for energy loss are involved for a single particle, including production of secondary particles. These particles may in turn produce particles, resulting in a cascade effect. Construction of a calorimeter that provides an accurate energy measurement with high precision relies on understanding the processes involved in a shower and the calorimeter response to a shower. This will be described in detail in this chapter.

A calorimeter is usually an important part of a high energy physics experiment for its useful properties, as follows:

- The relative precision of the energy measurement in a calorimeter improves with increasing energy, in contrast to the precision of momentum measurements based on the deflection of the particle in a magnetic field.
- A calorimeter can detect both charged and neutral particles.
- It can provide particle identification.
- With fine segmentation, it can provide information about the particle's momentum vector, supplementing (or replacing) tracking detectors in an experiment.
- Depending on the construction and materials, it can have a fast response time. This is essential in a high-rate environment. It can also provide the information needed immediately for on-line event selection by a trigger.
- It can be made quite compact, especially when using dense materials, and the size needed to contain the showers increases only logarithmically with energy.

A calorimeter can be constructed from a single material, which both absorbs the particles and produces an observable signal; this is called a *homogeneous* calorimeter. A *sampling* calorimeter, on the other hand, consists of more than one type of material:

passive materials, which only absorb energy, and an active part, which absorbs energy in an observable way. In this way, the shower energy is only sampled to produce a signal. The emphasis in this chapter will be on sampling calorimeters.

2.1 Interaction of particles with matter

In order to understand how a calorimeter works, one must examine the details of how particles interact in matter. These interactions can be divided into two groups, electromagnetic (e.m.) and strong interactions. An e.m. shower is produced by a particle that interacts only electromagnetically, such as a photon or an electron. A hadron, on the other hand, may produce shower particles that interact according to either strong or e.m. processes.

2.1.1 Electromagnetic showers

The principal mechanisms by which particles that interact only electromagnetically lose their energy in matter include well-understood effects, which are governed by the laws of quantum electrodynamics [1].

For photons, these processes are [2, 3]:

- The photoelectric effect, when the photon is absorbed by an atomic electron which is subsequently ejected from the atom. The cross section for this effect is proportional to Z^5, where Z is the atomic number of the material.
- Compton scattering, when the photon is scattered by an electron and transfers part of its energy to this electron.
- Pair production, when the photon is transformed into an e^+e^- pair in the presence of a nucleus. The energy of the photon must be at least twice the rest mass of the electron (1.022 MeV).

The mechanisms by which electrons and positrons may lose their energy are:

- Collision loss from inelastic scattering of the electron or positron on an atom, resulting either in ionization of the atom, if the energy transfer is sufficient, or in excitation of the atomic electrons [4]. The energy loss is described by the Bethe-Bloch formula [5].
- Bremsstrahlung, the emission of electromagnetic radiation when the electron or positron is scattered in the electric (Coulomb) field of a nucleus. The emitted photon then carries a (usually small) fraction of the energy, and the electron is scattered at a (usually small) angle. The energy and angle of the emitted photon depend on the strength of the Coulomb field, which depends on the Z of the absorber medium [6].

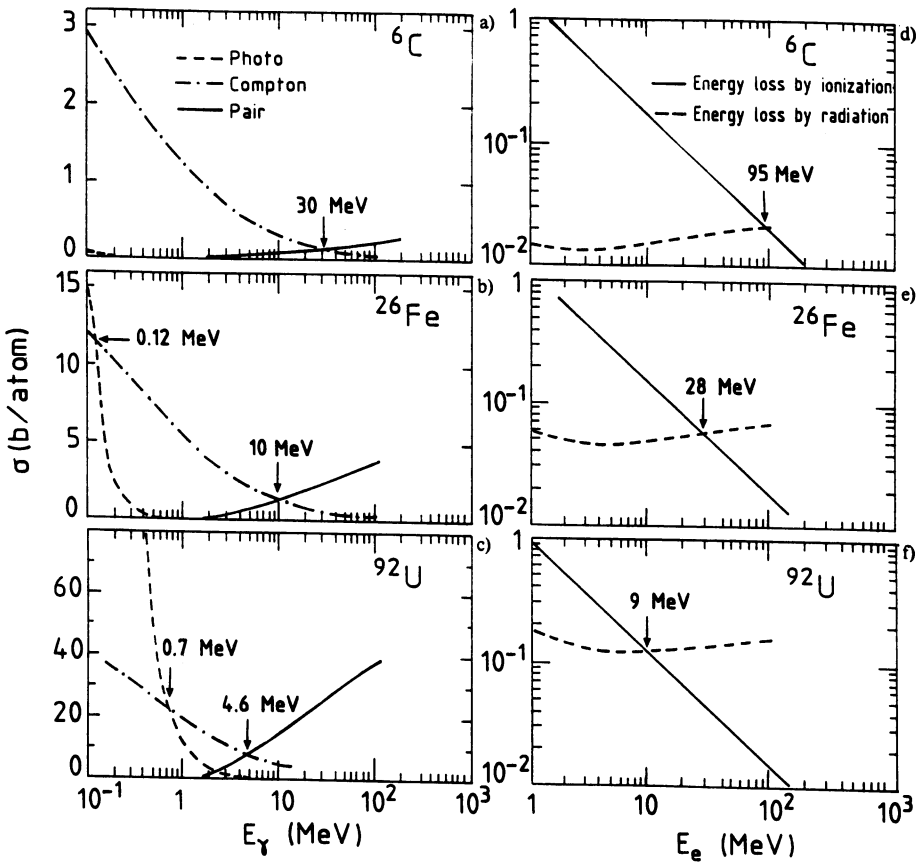

Figure 2.1: *The cross sections for the photoelectric effect, Compton scattering, and pair production as a function of the incident photon energy in carbon (a), iron (b), and uranium (c). The fractional energy loss by ionization and bremsstrahlung as a function of the electron energy in carbon (d), iron (e), and uranium (f) [7].*

The probabilities for these processes depend on energy and strongly on the density of electrons in the medium, which is given by Z, as shown in fig. 2.1. As the photon or electron loses its energy, different processes are favored, propagating the shower until all the energy has been lost. At relatively high energies ($\geq$ 10 MeV), pair production is the dominant process for photons, while for electrons and positrons bremsstrahlung is the principal process of energy loss. More and more particles are produced by these processes, but the average energy of these particles decreases as the shower continues. When a shower particle's energy is low enough, other energy loss mechanisms dominate, namely Compton scattering and the photoelectric effect for photons and ionization for electrons and positrons. The transition occurs approximately when the average energy of the shower particles is equal to the critical energy ϵ_c. It is defined as the energy at which the cross sections for ionization and bremsstrahlung are equal and is given approximately by [8]

$$\epsilon_c \text{ [MeV]} \approx \frac{550}{Z}, \tag{2.1}$$

with a precision better than 10% for Z between 13 and 92. When the average energy of the shower particles reaches ϵ_c, the number of particles is at its maximum. The longitudinal development of the shower can be described in an almost material-independent way in terms of the radiation length X_0, for high-energy ($>$ 1 GeV) showers. The radiation length is defined according to the differential equation for energy loss by radiation per unit length

$$\frac{\Delta E}{\Delta x} = -\frac{E}{X_0}, \tag{2.2}$$

which yields

$$E = E_0 e^{-x/X_0}, \tag{2.3}$$

where E_0 is the energy of the incident particle. Thus, X_0 is the distance over which a high-energy electron loses, on average, 63.2% of its energy. A photon on average travels $\frac{9}{7}X_0$ before converting into an e^+e^- pair. The radiation length can be approximated by [8]

$$X_0 \text{ [g/cm}^2\text{]} \approx \frac{180A}{Z^2}, \tag{2.4}$$

which is accurate within 10% for Z between 13 and 92. This formula expresses the strong Z-dependence of the radiation length, and therefore of the dimensions of e.m. showers. For example, the radiation length of carbon ($Z = 6$) is 18.8 cm, while that of lead ($Z = 82$) is only 5.6 mm. Electromagnetic shower detectors are usually constructed using a high-Z material in order to be compact.

The e.m. shower development is reliably simulated by the EGS4 Monte Carlo program [9]. Examples of such simulations of the longitudinal energy deposit are shown in fig. 2.2 for an electron showering in three materials with widely differing Z values. One sees that the distribution, when given in terms of X_0, is similar for different materials, with the maximum occurring when the average particle energy is ϵ_c. The maximum of

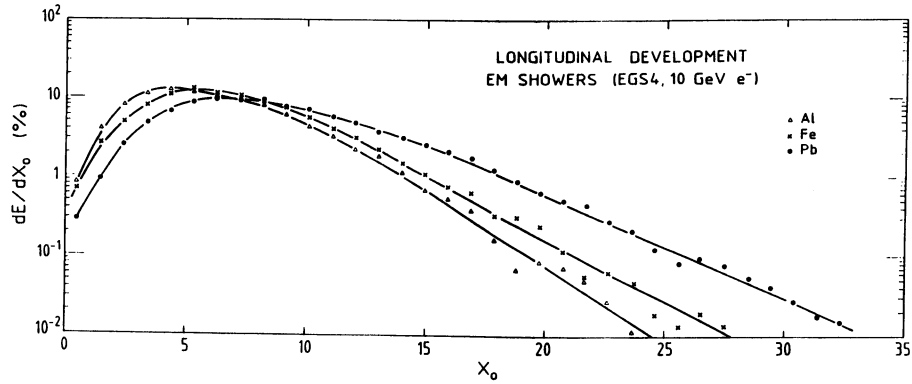

Figure 2.2: *The longitudinal development of a 10 GeV electron shower in aluminum, iron, and lead. Results of EGS4 calculations [7].*

the shower (in units of X_0) occurs at

$$t_{\max}\ [X_0] = \ln(\frac{E_0}{\epsilon_c}) + C, \tag{2.5}$$

where $C_e = -0.5$ for electron-induced showers and $C_\gamma = +0.5$ for photon-induced showers. Fig. 2.2 shows that the shower maximum occurs deeper in for lead ($Z = 82$) than for aluminum ($Z = 13$), since particle multiplication in lead continues until lower energies (see eq. 2.1). After the maximum, the shower energy deposition in lead also decreases at a slower rate than in aluminum, so that the total length of the shower in units of X_0 is greater.

The lateral spread of an e.m. shower is caused primarily by the multiple Coulomb scattering of electrons in the absorber. A measure of the average deflection experienced by electrons during multiple scattering near the critical energy after traversing one X_0 is given by the Molière radius R_M. It can be calculated according to [8]

$$R_M = \frac{E_s X_0}{\epsilon_c}, \tag{2.6}$$

where E_s, at 21.2 MeV, is a constant appearing in multiple scattering theory. This can be approximated by

$$R_M\ [\mathrm{g/cm^2}] \approx \frac{7A}{Z}, \tag{2.7}$$

with a precision better then 10% for Z between 13 and 92. In the early part of the shower, the lateral coverage is confined to a core of radius $\sim 1 R_M$, then spreading out from the shower axis beyond the shower maximum, as shown in fig. 2.3

2.1.2 Hadronic showers

When a hadron passes through matter, it interacts with the nuclei of the medium through strong interaction processes. This opens up a variety of possible ways for

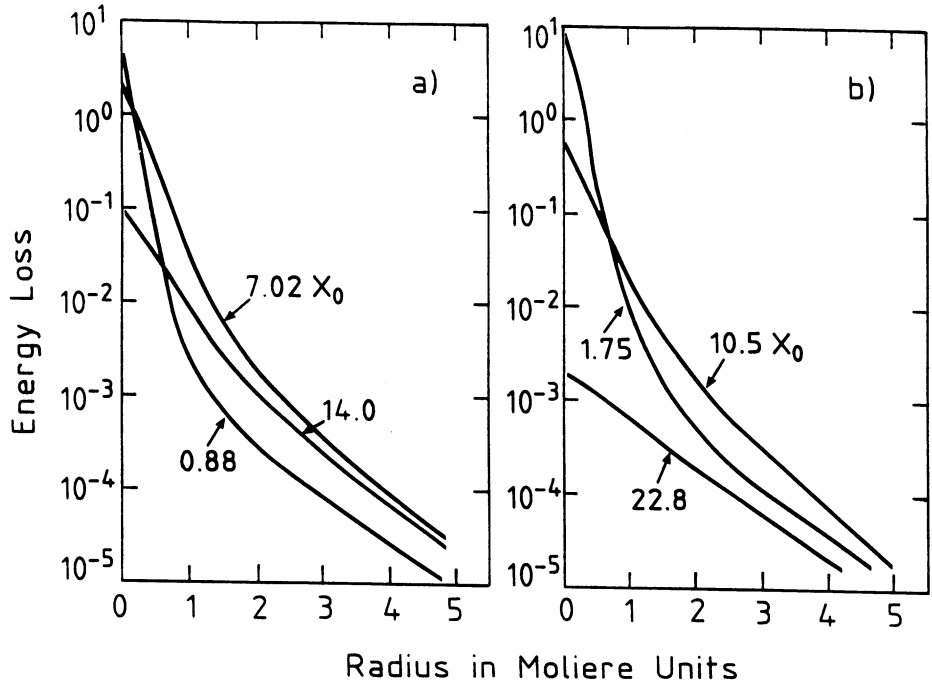

Figure 2.3: *The lateral profile of a 1 GeV e.m. shower at different depths in lead, as given by Monte Carlo calculations [8, 10].*

hadronic showers to develop, making them more difficult to describe and predict than e.m. showers. Basically, when a hadron enters the absorber, it interacts with a nucleus in such a way as to produce many secondary particles. These particles then either lose their energy by starting new reactions and creating more particles or by ionizing the surrounding media, propagating a shower until all the incident energy is spent.

A high-energy hadron striking an atomic nucleus will, in general, produce more particles of different types. Pions and other hadrons may be created if the energy transfer is high enough. The excitation energy of the remaining nucleus may be dissipated by evaporating free nucleons (typically with a kinetic energy of a few MeV) and by emitting γs, the majority which will have an energy below 2 MeV. In uranium, the nucleus can also undergo fission, and produce many slow (few MeV) neutrons in the process.

The charged particles from the hadronic shower (such as $K^{\pm}$, $\pi^{\pm}$, p, etc.) lose some energy by ionization before interacting with a nucleus. If the particle energy is less than 2 GeV, the particle may lose its energy only by ionization [6].

Neutrons only lose energy through strong interactions with nuclei [2, 11]. High energy neutrons ($\gtrsim$ 10 MeV) generally interact by elastic or inelastic collisions. Neutrons at lower energy are most likely to be captured by a nucleus, which then emits γs.

In uranium, neutrons at low energies may also be absorbed to cause fission, in turn producing slow neutrons. One may envision a high energy neutron traveling through the absorber medium, losing most of its kinetic energy through collisions. If it survives until its energy is very low (on the order of an eV), it is then captured, and deposits its remaining energy with the capturing nucleus, thus returning the nuclear binding energy that was needed for its original release. This process of thermalization is relatively slow ($\sim$1 μs), so that the neutron may travel a long distance before being captured. If the absorber is not large enough (which is usually the case), neutrons may escape altogether. The relative probabilities of these processes depend strongly on the choice of materials. The interaction of neutrons in matter turns out to be very important in determining the hadronic signal in a calorimeter and will be discussed later (sect. 2.4).

Some of the secondary particles, such as π^0s and ηs, have decay products that interact only electromagnetically, producing e.m. showers. This e.m. component, initiated mainly by neutral pions, shows up in a prompt energy deposition early in the shower [6]. On an event-by-event basis, the fraction of the energy lost through e.m. interactions may vary by a large amount, depending on which initial processes occur.

The distribution of the hadron energy deposit is similar to that of an e.m. shower deposit in shape, but its dimensions scale roughly with the nuclear interaction length λ_I [12]. A rough estimate [5] can be made using

$$\lambda_I \text{ [g/cm}^2\text{]} \approx 35A^{1/3}. \tag{2.8}$$

The nuclear interaction length governs both the lateral and longitudinal dimensions of the hadronic shower. The interaction lengths for some materials of interest, as well as other useful quantities, are listed in table 2.1.

Material	Z	A	λ_I [cm]	X_0 [cm]	R_M [cm]	ϵ_c [MeV]	ρ [g/cm^3]
Polystyrene	–	–	79.5	42.4	8.25	109	1.032
Argon	18	39.95	83.7	14.0	6.51	45.6	1.40
Iron	26	55.85	16.8	1.76	1.36	27.4	7.87
Lead	82	207.19	17.1	0.56	1.25	9.51	11.35
Uranium	92	238.03	10.5	0.32	0.81	8.36	18.95

Table 2.1: *Some properties describing shower dimensions for some typical calorimeter materials [5, 13].*

The longitudinal shower maximum occurs at a distance from the detector front, t_{max} which may be parametrized by [14]

$$t_{\max} \ [\lambda_I] \approx 0.2 \ln E + 0.7, \tag{2.9}$$

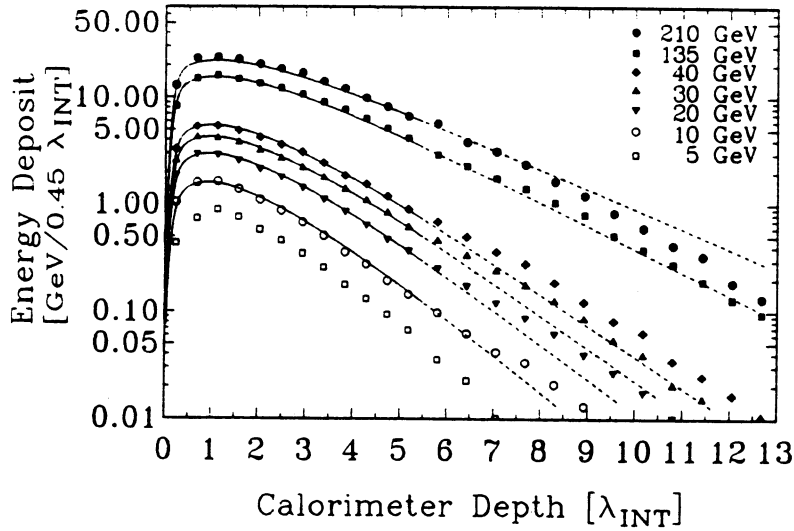

Figure 2.4: *Longitudinal energy distribution for 5-210 GeV pion showers in a calorimeter with a uranium-scintillator section up to $5\lambda_I$ followed by an iron-scintillator section; the curves were obtained by a parametrization [15, 16].*

where E is the energy of the incoming hadron in GeV. The depth required to contain on average 95% of the energy is [14]

$$t_{95\%}\ [\lambda_I] \approx t_{max} + 2.5E^{0.13}, \tag{2.10}$$

with t_{max} in units of λ_I and E in GeV. An experimental measurement of the longitudinal profile in a calorimeter is shown in fig. 2.4, for different energies.

The lateral energy deposit profile, as seen in fig. 2.5, shows a highly energetic, relatively collimated core due to π^0 production in the shower, with a halo produced by shower particles of lower energy which move further away from the shower axis. The lateral dimensions scale with λ_I, but also depend on the energy of the incident particle. In a high-energy shower, the fraction of the energy carried by π^0s is large (see above) and the core is more prominent compared to the halo.

The shower dimensions can be used to distinguish between hadronic and e.m. showers most easily in materials with large Z. In this case, the ratio λ_I/X_0 is high and the hadronic showers are much longer and wider than the e.m. showers.

2.2 Calorimeter response in sampling calorimeters

In a calorimeter, showers produce signals that give information about the incident particles. Some fraction of the energy of the shower goes toward excitation of the active medium, which generates an observable signal usually in the form of photons (from

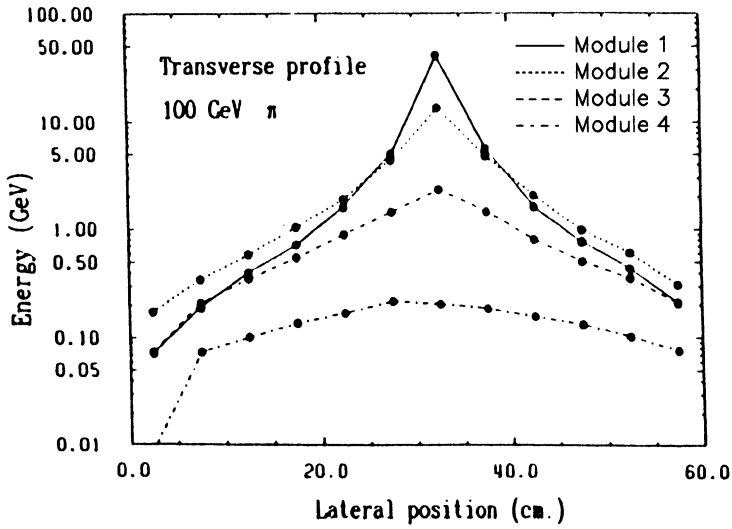

Figure 2.5: *Lateral shower profile for pions showering in a uranium-scintillator calorimeter at different depths. Each module is $1.5\lambda_I$ deep [17].*

scintillation or Čerenkov light), ionization charge, or electron-hole pairs (in semiconductors). The efficiency of this process depends on the type of shower particle producing the signal in a particular material, leading to differing signal characteristics produced by e.m. and hadronic showers. The signal generated by a shower can be understood as combination of the signals from the different particles within the shower. The response (*i.e.*, the average signal per unit of deposited energy) of each is, in general, not the same and change with energy, and thus it is useful to compare them to the response of a minimum ionizing particle (MIP), which is always the same for a specific calorimeter. A MIP is a fictitious particle which loses its energy by ionizing at the minimum rate dE/dx, independent of energy. An actual charged particle loses energy at a rate depending on the energy, as shown by the curves in fig. 2.6, where dE/dx is given by the Bethe-Bloch formula [5]. The signal produced by a MIP will be represented here by *mip*, given as part of a signal ratio. For example, the calorimeter response to an electromagnetic shower (represented by e) can be compared to the response to a muon (μ) by comparing e/mip to μ/mip.

The calorimetric response also depends on the type and amount of materials used to build the calorimeter. Here, the discussion will be limited to sampling calorimeters. A convenient way of describing a sampling calorimeter, and the usual geometry for such a calorimeter, is by using a "sandwich" structure. It is composed of planes consisting of alternately passive and active material with constant thicknesses. Only the ionizing particles crossing into the active layers produce the signal. One can describe the extent of this process in a calorimeter by a *sampling fraction*, the fraction of the total energy

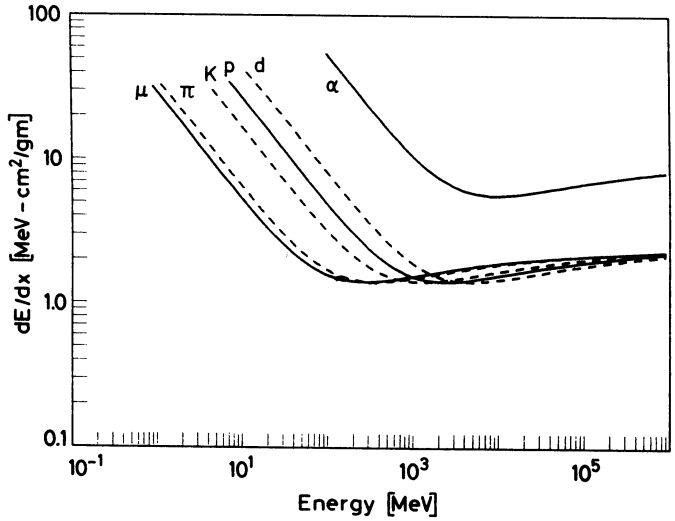

Figure 2.6: *Energy loss dE/dx due to ionization as a function of energy.*

deposited by ionization loss in the active layers. The sampling fraction for MIPs is an unambiguous number that is used to compare different calorimeters. It can be calculated as:

$$f_{\text{samp}} = \frac{\Delta E_{\text{MIP,act}}}{\Delta E_{\text{MIP,act}} + \Delta E_{\text{MIP,abs}}}, \tag{2.11}$$

where $\Delta E_{\text{MIP,act}}$ and $\Delta E_{\text{MIP,abs}}$ are the mean energy depositions by a MIP in one active layer and in one absorber layer, respectively. This sampling fraction is roughly equal to the mass ratio of active to passive materials in the calorimeter [7]. Typical sampling fractions are 5-10% for scintillator-based calorimeters and $\sim 10^{-4}$% for gaseous calorimeters.

In the following discussion of calorimetric response, only the average behavior of the shower particles is considered. In an actual shower, there are fluctuations in the energy deposit which are reflected in the uncertainty of the energy measurement, the *energy resolution*, the subject of a later section.

2.2.1 Response to electromagnetic showers

The signal from an e.m. shower should be proportional to the energy of the entering particle. This can be understood by seeing the shower as made up of smaller showers, which produce signals that can be added up to be the total signal. For instance, a photon of energy E enters the calorimeter and can produce an electron and a positron of equal energy $E/2$, which then produce their own showers. A secondary shower produces the same signal as a shower initiated by a particle with the same energy, so that the signal produced by the initial photon is twice that of the signal produced by a

particle with energy $E/2$. Therefore, the signal is proportional to the incident energy, and the calorimetric measurement of the particle energy is possible.

Since a signal from an e.m. shower results from the ionization of the active material by the electrons and positrons in the shower, one would expect the shower to be sampled like a MIP, *i.e.*, $e/mip = 1$. This, however, is not true, especially in calorimeters with high-Z absorber and low-Z active material. Simulations with EGS4 [18] have shown that most of the energy is deposited in the calorimeter by soft electrons (with energy less than ϵ_c), which have been produced by Compton scattering and the photoelectric effect. Most of them, however, do not contribute to the signal, for the following reason. A large fraction of the soft shower electrons are produced by photons via the photoelectric effect, but only those produced in or near the active material give rise to a signal. The range of electrons with energy of 0.1-1 MeV is less than a millimeter. In a calorimeter composed of high-Z absorber and low-Z active material, most of the low-energy photons (> 1 MeV) interact in the absorber, since the cross section for this process is proportional to Z^5, whereas the cross section for ionization by charged particles is proportional to Z. Of these, only the small fraction occurring in the boundary region contributing to the signal. In effect, the calorimeter is less efficient at detecting the low energy part of the shower, which is the major part. The high-energy particles are sampled like MIPs, but they are fewer in number. Therefore, the average calorimeter response to the e.m. shower is less than the response to a MIP. Results of simulations and data support this decrease in e/mip with increasing absorber Z, as shown in fig. 2.7. A typical calorimeter with high-Z absorber has an e.m. sampling fraction $e/mip \approx 0.6$ [19].

2.2.2 Response to hadronic showers

In general, the signal produced by a hadronic shower in a calorimeter is not linear with the energy of the incident particle. The fraction of total energy in the e.m. component of the shower increases with increasing energy (sect. 2.1.2), and its contribution to the signal increases likewise. This results in a disproportionately large total signal at high energy. It will be shown later (sect. 2.4) that the signal is only proportional to the energy for hadronic calorimeters in which the average response to the e.m. component (e) of the shower is the same as the response to the non-e.m. component (h). In general, this is not true, because a large fraction ($\sim 40\%$ [11]) of the energy dissipated in the non-e.m. component of the hadronic shower does not produce a signal. This *invisible energy* includes nuclear binding energy loss (the energy needed to release nucleons from the nucleus, target recoil energy, and the energy carried by neutrons, neutrinos and muons that escape the calorimeter. Therefore, the non-e.m. response is usually less than the e.m. response ($e/h > 1$).

The signal produced by the e.m. component of the hadronic shower is generated the same way as an electron-induced shower, with the same e/mip (sect. 2.2.1). The non-e.m. signal is produced by ionizing hadrons, soft neutrons, and soft γs, with normalized sampling fractions ion/mip, n/mip, and γ/mip, respectively. The processes in which

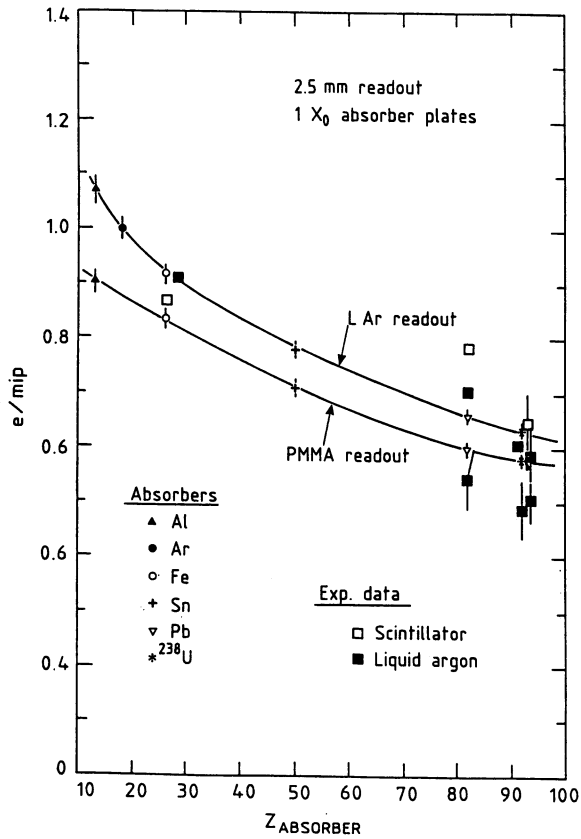

Figure 2.7: *The e/mip ratio as a function of the Z of $1X_0$ of absorber in a sampling calorimeter, with 2.5 mm of either liquid argon or scintillator as readout material. The solid lines are the results of EGS4 simulations; the squares represent experimental data [11].*

these particles are created in the shower were discussed in sect. 2.1.2. The e/h signal ratio can be written in terms of the these components as [18]

$$\frac{e}{h} = \frac{e/mip}{f_{\text{ion}}(ion/mip) + f_{\text{n}}(n/mip) + f_{\gamma}(\gamma/mip)}, \tag{2.12}$$

where f_{ion}, f_{n} and f_{γ} are the average fractions of the energy in the non-e.m. component deposited in the form of ionizing hadrons, neutrons, and nuclear γ's, respectively.

In practice, the e/h ratio cannot be directly measured. It can be inferred from the so-called e/π signal ratio, the ratio between the signal from an electron shower and the signal from a pion shower (including the e.m. component) produced by incident

particles of the same energy. The two ratios are related by

$$\frac{e}{\pi}(E) = \frac{e}{(1 - f_{\text{e.m.}})h + f_{\text{e.m.}}e} = \frac{e/h}{f_{\text{e.m.}}(e/h - 1) + 1}. \tag{2.13}$$

The fraction $f_{\text{e.m.}}$ of the pion energy that is dissipated by e.m. processes changes from event to event, but the average fraction $\langle f_{\text{e.m.}} \rangle$ increases with increasing initial energy approximately according to the empirical expression [20]

$$\langle f_{\text{e.m.}} \rangle = 0.1 \ln E \tag{2.14}$$

for E between 10 and 100 GeV. Alternatively, it may be expressed by following a power law [21]:

$$\langle f_{\text{e.m.}} \rangle = 1 - E^{(m-1)}, \tag{2.15}$$

where E is in units of GeV and $m \approx 0.85$. (See sect. 4.4.4 for a measurement of this fraction.) Since $\langle f_{\text{e.m.}} \rangle$ depends on the energy, e/π is energy-dependent but e/h is not.

In the non-e.m. part of the shower, γs are produced from nuclear de-excitation, fission reactions, inelastic scattering, and neutron capture (sect. 2.1.2). They have, in general, energies below 2 MeV, and so they are also sampled inefficiently, as described for soft γs from e.m. showers in calorimeters with a high-Z absorber and low-Z readout (sect. 2.2.1). The average γ/mip ratio is therefore smaller than e/mip. In a calorimeter with high-Z absorber, $\gamma/mip \approx 0.3$ [19].

The efficiency ion/mip for the conversion of charged hadron ionization energy into a signal is close to 1, since these particles behave like MIPs. The ratio deviates from unity for several reasons relating to the particular calorimeter [11]:

- The range of low-energy protons may be smaller than the absorber thickness, hence reducing p/mip.
- Many of these particles are non-relativistic, and thus the sampling fraction is greater than the MIP sampling fraction (see fig. 2.6). This effect is dependent on the energy and Z of the material.
- Saturation or recombination effects in the readout material decrease the ion/mip ratio. This occurs in particular in calorimeters composed of liquid argon or scintillators.
- If the Z of the absorber is much higher than the Z of the active material, then low-energy hadrons lose some energy by multiple scattering in the absorber. The cross section for multiple electron scattering increases with increasing Z, thus reducing ion/mip in high-Z absorbers.

In general, if the calorimeter is not saturating, $ion/mip \approx 1$, decreasing to ~ 0.8 for a saturating calorimeter [11].

The neutron sampling fraction n/mip depends on the nuclear characteristics of the calorimeter materials. Soft neutrons may induce a signal in the active material through

elastic scattering when recoil charged particles ionize the material. In the few MeV range, this is the most frequent reaction [11], but the sampling is inefficient ($n/mip \ll 1$) except in materials containing hydrogen. In a calorimeter with hydrogenous active material, neutron-proton elastic scattering occurs almost exclusively in this layer, and practically all the energy transferred to the recoil proton contributes to the signal, resulting in a high n/mip value. The neutron sampling fraction may also depend on the readout gate width, which, if too short, may not allow for 100% neutron capture. In a scintillator, which saturates, typical n/mip values range from 1 to 2, whereas, in a liquid argon, which contains no hydrogen, $n/mip \approx 0$ [19].

Invisible energy ($\sim$ 40%) and ionization by charged hadrons comprise most of the energy dissipated in the non-e.m. part of a hadronic shower. The latter fraction $f_{\rm ion}$ depends on the material, roughly increasing as Z/A. It ranges from $\sim$ 40% in uranium and lead to $\sim$ 60% in iron [11].

At low energies, neutron production by nuclear interactions is greater than proton production since the nuclear Coulomb barrier prevents these protons from escaping. In addition, in a high-Z material, there are more neutrons in the target nuclei. Therefore, one expects a significant fraction of the non-e.m. energy to be carried by soft neutrons. The fraction $f_{\rm n}$ of total non-e.m. energy carried by neutrons with kinetic energy less than 20 MeV is 8-15%, increasing with the Z of the absorber [11].

The fraction f_γ of non-e.m. energy carried by low-energy γs from nuclear deexcitation is small, usually 2-3% [11]. It is especially high in uranium due to fission γs.

In a non-uranium calorimeter with a high-Z absorber, eq. 2.12 is approximately [22]

$$\frac{e}{h} = \frac{e/mip}{0.41 + 0.2(n/mip)}. \tag{2.16}$$

In summary, the non-e.m. component of the hadronic signal is dominated by the signal from ionizing hadrons, but the neutrons also play an important role, especially in optimizing the response of a calorimeter. These particles, along with the γ contribution, have low energy and mainly contribute to the signals from the later part of the shower. The signal from the early part of the shower is dominated by the e.m. shower component.

2.3 Energy resolution

The energy resolution gives the uncertainty in a calorimetric measurement and is usually written as σ/E (*i.e.*, as a fraction of the incident energy). For sampling calorimeters, it can be broken down according to the source of the fluctuations on this measurement, as follows.

- Intrinsic fluctuations in the shower development and the shower processes from event to event.

- Sampling fluctuations, which are fluctuations in the the parts of the shower and the total amount of the energy that is deposited in the active material.
- Statistical fluctuations in the number of photoelectrons contributing to the signal.
- Instrumental effects, such as the uncertainty in the calibration, stability of the electronics, fluctuations in shower leakage, and non-uniformity in calorimeter response, which should be eliminated in the calorimeter design and usage.

The calorimetric measurement is statistical in nature, since a shower is made up of many different processes which produce a signal in the calorimeter. Statistical uncertainty σ depends on the number n processes which occur,

$$\sigma = \sqrt{n}. \tag{2.17}$$

In a linear calorimeter, the number of processes is proportional to the energy E deposited in the active medium, which is proportional to the signal. Assume more specifically that S is the signal produced by a 1 GeV shower consisting of n shower particles, with resolution as given above. Another shower with incident energy E GeV would produce (in a linear calorimeter) a signal $S' = ES$ resulting from $n' = En$ shower particles, measured with resolution $\sigma_{S'} = \sqrt{En}$. The energy resolution can be expressed

$$\frac{\sigma_E}{E} = \frac{\sigma_{S'}}{S'} = \frac{\sqrt{En}}{En} = \frac{1}{\sqrt{E}}\frac{1}{\sqrt{n}} = \frac{C}{\sqrt{E}}, \tag{2.18}$$

where C is a constant and E is given in GeV. Gaussian fluctuations in the processes contributing to the calorimeter signals will contribute to the energy resolution as $1/\sqrt{E}$. Therefore, the energy resolution improves with increasing energy. For example, if the active material is scintillator, the light signal is given by the number n of photoelectrons produced. If on average 1000 photoelectrons are produced for an incident particle energy of 1 GeV, the contribution of photoelectron statistics to the energy resolution amounts to $3.2\%/\sqrt{E}$. The intrinsic shower fluctuations and the sampling fluctuations, both based on statistical processes, contribute to energy resolution in the same way, proportional to $1/\sqrt{E}$.

The contribution to the energy resolution due to instrumental effects may be independent of the energy of the incident particle, appearing as a constant. Others may contribute an amount dependent on energy. This must be determined for each particular effect.

In general, the variance of each contribution to the resolution is added together to find the total variance (the square of the resolution), *i.e.*

$$\left(\frac{\sigma}{E}\right)^2 = \left(\frac{\sigma}{E}\right)_1^2 + \left(\frac{\sigma}{E}\right)_2^2 + \left(\frac{\sigma}{E}\right)_3^2 + \cdots, \tag{2.19}$$

or, in a shorthand notation, each resolution term is said to be added quadratically:

$$\frac{\sigma}{E} = \left(\frac{\sigma}{E}\right)_1 \oplus \left(\frac{\sigma}{E}\right)_2 \oplus \left(\frac{\sigma}{E}\right)_3 \oplus \cdots, \tag{2.20}$$

provided that the terms are not correlated to each other. However, some sources of fluctuations may be correlated to some degree, and their contributions to the resolution may have to be be added linearly, or in some intermediate way. The above expression is usually only approximate. The actual relation between all sources of fluctuations is, on the whole, difficult to determine, but eq. 2.20 usually describes the data well.

In the following sections, the specific sources of fluctuations in e.m. and hadronic showers in sampling calorimeters are discussed in detail.

2.3.1 Electromagnetic energy resolution

In a typical sampling calorimeter, the main contribution to the e.m. energy resolution is due to sampling fluctuations. The signal is only produced in the active layers and is therefore determined by the number of charged tracks crossing these layers. There are statistical fluctuations around this number, so the resolution is proportional to $1/\sqrt{E}$.

Charged shower particles can be sampled in three ways:

i. All soft electrons produced in the active material contribute to the signal. Their number is proportional to ratio of the volume of active material and passive material, or $t_{\text{act}}/t_{\text{abs}}$ in the case of a sandwich calorimeter. Their range is short compared to the layer thicknesses, so they do not cross into another active plane. Their fluctuations vary with the total number of such particles. For a fixed t_{act}, the fluctuations are $\sigma/E \propto \sqrt{t_{\text{abs}}}$, and, for a fixed t_{abs}, the contribution to the resolution by these fluctuations is $\sigma/E \propto 1/\sqrt{t_{\text{act}}}$.

ii. Soft electrons, again with a short range, produced in the absorber near the boundary with the the active layer may cross this boundary and produce a signal. Their number is proportional to the surface area of the active/passive boundary. For a sandwich calorimeter, this number is inversely proportional to the absorber thickness t_{abs}, except for very thin absorbers (< 1 mm); for a calorimeter with fiber active material, the number is proportional to the diameter $\varnothing$ of the fibers. Their fluctuations then scale as $\sqrt{t_{\text{abs}}}$ and $\sqrt{\varnothing}$, respectively, for a fixed sampling fraction.

iii. Fast shower particles created via $\gamma \rightarrow e^+e^-$ may traverse one or more active planes. Since the n particles are produced in pairs, the number of processes contributing to the signal (by traveling through only one active layer) is $n/2$. Their contribution to the sampling fluctuations is then $\sqrt{2/n}$. If the absorber layer is very thin ($< 1X_0$), the e^+e^- pair may traverse more active layers, and the fluctuations are larger since the processes are fewer in number.

Simulations with EGS4 [7] have shown that the number of e^+e^- pairs is small compared to the soft electrons created by the Compton and photoelectric effects in calorimeters with high-Z absorber. The charged particle crossings are therefore uncorrelated, so the sampling fluctuations are the fluctuations in the number of different shower particles

contributing to the signal. This is supported by experimental results, in which almost no correlation was found between signals of subsequent layers [23, 24]. Therefore, the sampling fluctuations are determined mainly by the soft shower electrons sampled as in the second case. The number of different shower particles contributing to the signal is proportional to f_{samp}, therefore, for a calorimeter composed of low-Z active layers and high-Z passive layers, the sampling term can be expressed in terms of the sampling fraction as [22]

$$\left(\frac{\sigma(E)}{E}\right)_{\text{samp}} \propto \frac{1}{\sqrt{f_{\text{samp}}}}\frac{1}{\sqrt{E}}. \tag{2.21}$$

A contribution to the energy resolution from photoelectron statistics, as described in the previous section, may also be significant. On the other hand, the contribution from intrinsic shower fluctuations is small, as the e.m. shower processes are many.

The total resolution for the energy measurement of e.m. showers in an ideal calorimeter should fit the expression

$$\left(\frac{\sigma(E)}{E}\right)^2 = \left(\frac{\sigma(E)}{E}\right)^2_{\text{intr}} + \left(\frac{\sigma(E)}{E}\right)^2_{\text{samp}} = \frac{C^2_{\text{intr}} + C^2_{\text{samp}}}{E}, \tag{2.22}$$

where C_{intr} and C_{samp} are constants. However, as no calorimeter is perfect, its energy resolution usually has some contribution from fluctuations due to instrumental effects. Some effects may contribute to the energy resolution in a way that depends on E. For example, in LAr calorimeters, the resolution due to noise is proportional to $1/E$ and may be large. Other effects contribute to σ/E as as a constant term, which may dominate at high energies. Examples of such effects are non-uniformity in the signal, calibration errors, and pedestal uncertainties.

The energy resolution can be written in the general form

$$\frac{\sigma(E)}{E} = \sqrt{\frac{C_1^2}{E} + C_2^2} = \frac{C_1}{\sqrt{E}} \oplus C_2, \tag{2.23}$$

where the first term is the resolution due all statistical fluctuations and the second term is due to other fluctuations uncorrelated to the first term. If the constant term is correlated to the scaling term, it may be added linearly, *i.e.*,

$$\frac{\sigma(E)}{E} = \frac{C_1}{\sqrt{E}} + C_2. \tag{2.24}$$

In most practical calorimeters, neither expression is completely correct, since realistic fluctuations do not follow such simple expressions. See sect. 4.3.4 for experimental determination of the resolution.

2.3.2 Hadronic energy resolution

The hadronic energy resolution is determined mainly by intrinsic and sampling fluctuations. The fluctuations in hadronic shower development are greater than those for an

e.m. shower. This is not only because the shower is produced by relatively few interactions, but because processes develop very differently. There are large, non-Gaussian fluctuations in the e.m. fraction of a hadron shower, largely dependent on the nuclear interactions early in the shower (sect. 2.1.2). The fraction of energy that does not produce a signal, *i.e.*, invisible energy (sect. 2.2.2), varies from event to event with an average of ~40%. These fluctuations contribute to the resolution in a statistical way, proportional to $1/\sqrt{E}$. In addition, the average fraction $f_{\text{e.m.}}$ of the particle energy carried by electromagnetically interacting shower particles (eq. 2.14, 2.15) is a function of energy. If the calorimeter response to the e.m. energy deposit differs from the response to the non-e.m. energy deposit, the non-Gaussian event-to-event fluctuations in this fraction cause a deviation from $1/\sqrt{E}$ scaling, which can be parametrized as [11]

$$\left(\frac{\sigma(E)}{E}\right)_{\text{intr}} = \frac{A}{\sqrt{E}} + B, \tag{2.25}$$

where A and B are constants.

The sampling fluctuations are roughly twice as large for hadronic showers than for e.m. showers in the same calorimeter. In a sandwich calorimeter, the sampling term of the energy resolution approximately follows the empirical relation [24]

$$\left(\frac{\sigma(E)}{E}\right)_{\text{samp}} \approx 11.5\%\sqrt{\frac{\Delta E\ [\text{MeV}]}{E}}, \tag{2.26}$$

where ΔE is the energy lost by a MIP crossing one layer of the calorimeter.

In general, one may then write the hadronic resolution as

$$\frac{\sigma(E)}{E} = \frac{C_{\text{intr}}}{\sqrt{E}} \oplus \frac{C_{\text{samp}}}{\sqrt{E}} + C \tag{2.27}$$

or as

$$\frac{\sigma(E)}{E} = \frac{C_{\text{intr}}}{\sqrt{E}} \oplus \frac{C_{\text{samp}}}{\sqrt{E}} \oplus C, \tag{2.28}$$

where the first term is due to the intrinsic fluctuations in hadronic shower process, the second term comes from sampling fluctuations, and the last term is the constant term due to fluctuations in $f_{\text{e.m.}}$. There is some debate as to whether this term should be added linearly (if correlated to the scaling term) or quadratically (uncorrelated). Experimental evidence with heavy ions in a calorimeter supports linear addition [25], while Monte Carlo studies and detailed calculations support quadratic addition [26]. As in the e.m. case, both expressions are likely to be oversimplified descriptions.

Detector imperfections are not included, but may also contribute to the energy resolution, as discussed for the e.m. energy resolution. Another frequent source of fluctuations in the hadronic shower signal results from the shower leakage. This contributes to the energy resolution in an energy-dependent way, since the shower dimensions are energy dependent and the fluctuations are usually non-Gaussian.

The hadronic energy resolution is limited by the intrinsic and sampling fluctuations in the calorimeter. A constant term may dominate at high-energies and, therefore, this term should be reduced as much as possible. This can be done by eliminating instrumental contributions, leaving only a constant term due to the fluctuations in $f_{\text{e.m.}}$. It turns out the effect of these fluctuations on the resolution can be reduced by building a compensating calorimeter, the subject of the next section.

2.4 Compensating hadronic calorimeters

The art of making a high-precision calorimeter to measure hadronic energy was initiated with the observation that, for certain uranium/scintillator calorimeters, one could obtain a surprisingly good energy resolution and linearity [23, 27]. It turned out that, rather than being a property of this particular combination of material, the excellent performance was a result of having equal responses from the e.m. and non-e.m. components of an hadronic shower, *i.e.*, $e/h = 1$ [11, 28]. This is the condition to have a *compensating* calorimeter, where, in the usual terminology, a calorimeter is *undercompensating* if $e/h > 1$ and *overcompensating* if $e/h < 1$. As discussed in sect. 2.2.2, most practical calorimeters are undercompensating.

2.4.1 Compensation

In a non-compensating calorimeter, the fluctuations in the e.m. fraction of hadronic showers contribute greatly to the energy resolution (sect. 2.3.2). Fig. 2.8 shows this more explicitly. If a hadronic shower consisted of purely an e.m. or a non-e.m. shower, the signal distributions would appear as one of the curves in the top picture for a non-compensating calorimeter and in the bottom figure for a compensating one. In reality, hadronic showers contain both components, in varying fractions for each individual shower, so that the actual response lies somewhere between the e.m. and non-e.m. distributions. For example, the hadronic shower may consist of mostly π^0-production therefore its response would be close to the mean of the e.m. distribution. If the shower is propagated mostly by strong interactions, the signal is close to the mean of the non-e.m. distribution. From fig. 2.8*a*, it is seen that, when $e/h \neq 1$, there is quite a difference between the signals from these two extreme types of showers and that all the signals would be distributed between. In a compensating calorimeter, fig. 2.8*b*, this source of fluctuations has been eliminated: the average signal distribution is centered around the same mean value, independent of the e.m. fraction.

In addition, the signal from a non-compensating calorimeter is not proportional to the incident particle energy, since $\langle f_{\text{e.m.}} \rangle$ increases with energy (eq. 2.14, 2.15). A compensating calorimeter is not sensitive to $f_{\text{e.m.}}$ in its response, and therefore its signal is linear with energy.

The consequences of $e/h \neq 1$ in a hadronic calorimeter include:

- a contribution to the energy resolution due to fluctuations in $f_{\text{e.m.}}$;

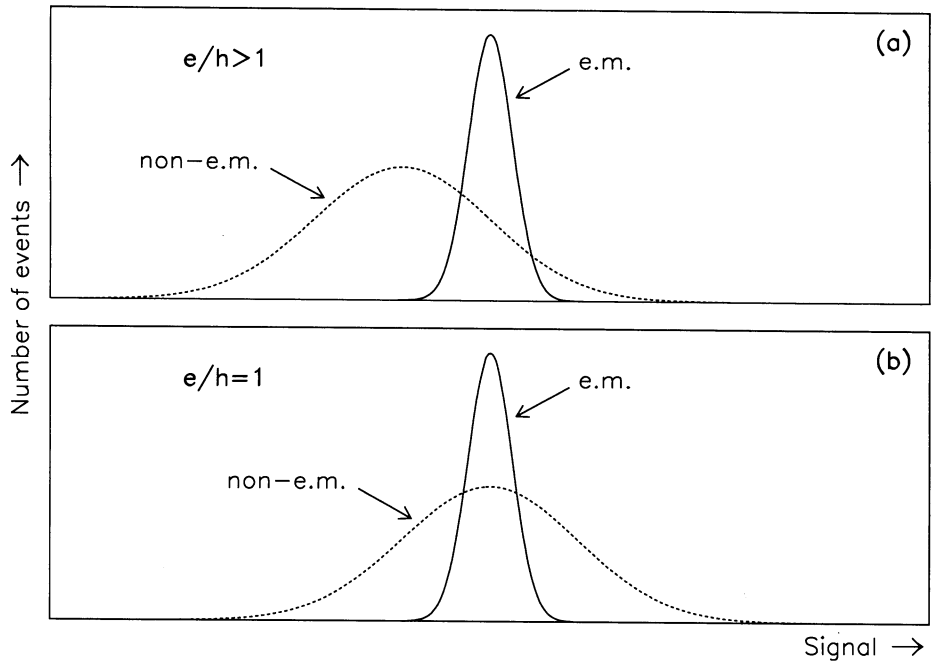

Figure 2.8: *(a) The signal distributions for purely e.m. (solid line) and non-e.m. (dashed line) showers in a non-compensating calorimeter. The actual response to a hadronic shower is a combination of both components according to the highly fluctuating fraction* $\langle f_{\text{e.m.}} \rangle$*, so that the actual distribution appears somewhere between these two extreme cases. (b) The signal distributions in a compensating calorimeter. The actual hadronic signal distribution has this average, independent of* $\langle f_{\text{e.m.}} \rangle$*.*

- a non-linear response with energy;
- a non-Gaussian signal distribution;
- deviations from scaling with $1/\sqrt{E}$, which dominate the energy resolution at high energies;
- energy dependence of the measured e/π signal ratios (eq. 2.13).

Therefore, a compensating calorimeter is desirable for high-precision hadron detection.

2.4.2 How to reach compensation

Several methods can be employed to make a calorimeter compensating, usually in order to reduce e/h towards unity. One may increase the non-e.m. response and/or

decrease the e.m. response by adjusting the values of the terms in eq. 2.12. The major mechanisms that can be exploited are:

i. The non-e.m. response (via f_γ, f_n) can be increased by using a fissionable material as an absorber, such as depleted uranium. The extra energy created in the nuclear fission reaction can be detected in the readout material.

ii. The e.m. response (e/mip) can be decreased by combining a low-Z active material with a high-Z absorber in order to suppress the response from photoelectric effect in the active material (as described in sect. 2.2.1). The signal produced by photoelectrons can be further suppressed by inserting a thin layer of low-Z material between the active and passive layers. This way the photoelectrons produced near the border of the passive material are absorbed in the extra layer and never enter the active part.

iii. The non-e.m. response can be increased (through n/mip) by using an hydrogenous material as the active component. In such a material, the cross section for elastic neutron scattering, with the energy released in this process going toward producing a signal (sect. 2.2.2). The most common material used for this purpose is plastic scintillator.

Changing the e/h ratio is only possible with sampling calorimeters, since it depends on having certain combinations of materials in a certain volume ratio. Once the materials have been chosen, preferably a high-Z absorber and a low-Z active material, the e/h value can be tuned by varying the relative amounts of these materials. In the case of a sandwich calorimeter, this is achieved by varying the thicknesses of the layers. This is shown in fig. 2.9 for lead calorimeters, where it is seen that, with a hydrogenous active material, n/mip (especially the component from recoil protons) increases with the ratio of the the thicknesses of the passive and active layers ($R_d = t_{\text{abs}}/t_{\text{act}}$), *i.e.*, with decreasing sampling fraction. As a result, e/h decreases, reaching $e/h = 1$ at some point. For example, one should be able to make a compensating calorimeter out of lead and scintillator (curve 7 in fig. 2.9*b*) with $R_d \approx 4$. In this figure, it is also seen that the calorimeters without hydrogenous readout (liquid argon, silicon) cannot be made compensating by varying the sampling fraction.

The detection of neutrons by the active material is particularly important for compensation. It is useful to have a high-Z absorber which produces these neutrons in abundance, which can then be detected by the active material. In this way, a high-Z absorber and hydrogenous active material work together to achieve compensation.

The use of a hydrogenous active material works in another way to reduce fluctuations. For every neutron released by a nucleus (with the potential to interact in the active material), some "invisible" energy is lost, resulting a correlation between the energy carried by these neutrons and the binding energy. This is confirmed by simulation, as shown in fig. 2.10. It follows that the invisible binding energy loss is correlated to the energy deposited in the scintillator through by the neutrons (fig. 2.11), reducing

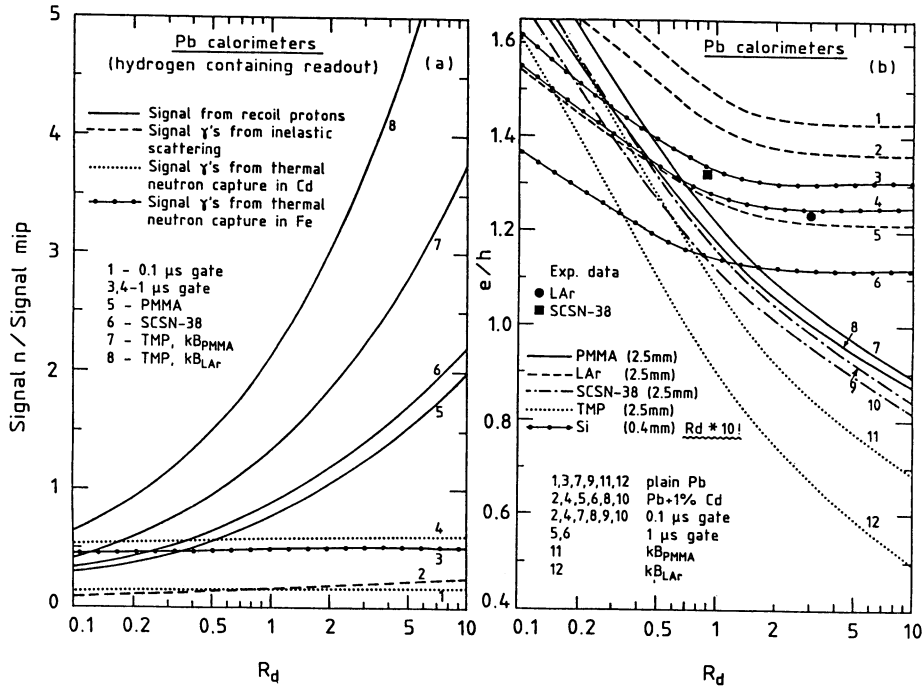

Figure 2.9: *(a) The normalized neutron sampling fraction n/mip as a function of the ratio R_d of the thicknesses of the passive and active layers, in lead calorimeter. The solid lines give the contribution from recoil protons for calorimeters using plastic scintillator (5, 6) and warm liquids (7, 8). The other lines give the other contributions for SCSN-38. (b) The e/h ratio as a function of R_d for lead calorimeters with various readout materials. Lines are the results of simulations; points are experimental results [11].*

the intrinsic shower fluctuations, as well as boosting the low non-e.m. energy deposit. The degree of the correlation depends on the Z of the active material and whether the active material contains hydrogen.

2.4.3 A compensating lead/scintillator calorimeter

Uranium calorimeters were the first compensating calorimeters built and used. Once it was realized that one could theoretically build a compensating calorimeter out of other materials [30, 31, 11], a compensating lead calorimeter was investigated [32]. In a calorimeter, lead ($Z = 82$) has similar properties to uranium ($Z = 92$), except that nuclear fission does not occur in lead. A compensating uranium/scintillator calorimeter has $R_d = t_{\text{abs}}/t_{\text{act}} \approx 1$ [33, 34], with an effective λ_I of ~20 cm, the same as a compensating lead calorimeter, with the predicted $R_d \approx 4$ (fig. 2.9). Therefore, compensating lead

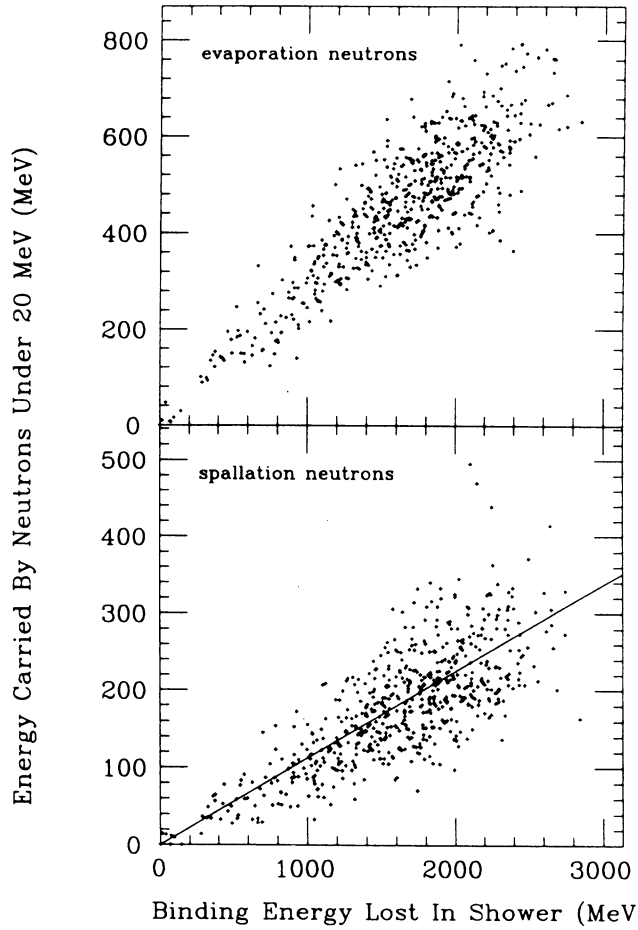

Figure 2.10: *The correlation of the energy carried by evaporation (top) and spallation (bottom) neutrons below 20 MeV with the binding energy lost in 5 GeV π^- showers in a uranium-scintillator calorimeter. The curve shows the average trend of the Monte Carlo data [29].*

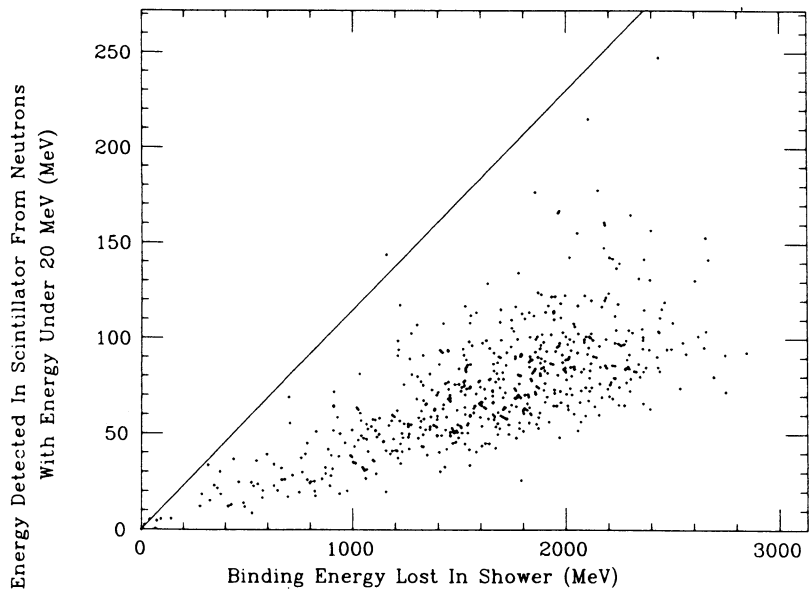

Figure 2.11: *The neutron energy detected in the scintillator versus the binding energy loss, in the same case as fig. 2.10. The solid line is same one as in fig. 2.10, to show the amount of energy from the neutrons deposited in the scintillator [29].*

and uranium calorimeters are equally compact, in spite of the differences in the density of the the absorber material. Lead is more practical for building a calorimeter, since it is abundant, cheap, and easy to handle. In addition, there is no radioactive noise, as there is in uranium, to contribute to the energy resolution, although this noise can be very useful by providing a constant and uniform calibration source.

A sandwich calorimeter composed of 10 mm thick lead plates and 2.5 mm thick scintillator sheets built by the ZEUS Calorimeter Group confirmed predictions for compensation and its consequences [32]. The e/π signal ratio was measured to be 1.05 ± 0.04 for $E > 10$ GeV. Compensation is also evident since the pion energy resolution scales with $1/\sqrt{E}$ up to 75 GeV, as shown in fig. 2.12. The resulting resolution for hadrons was $(44.2 \pm 1.3)\%/\sqrt{E}$, with E in GeV, while for e.m. showers $(23.5 \pm 0.2)\%/\sqrt{E}$ was measured. Using the signals produced by muons, the e/mip ratio was calculated to be 0.67 ± 0.03, in good agreement with Monte Carlo predictions of $e/mip = 0.65$. The resolutions due to sampling and intrinsic fluctuations were also determined [24] and are listed in table 2.2, along with the resolutions for a compensating calorimeter composed of uranium (3.2 mm layers) and scintillator (3.0 mm layers), for comparison. It is interesting to note that the intrinsic hadronic resolution for the lead calorimeter ($\sim$13%) is considerably better than that for the uranium calorimeter ($\sim$20%). This is explained by the fact that the correlation between kinetic neutron energy and lost bind-

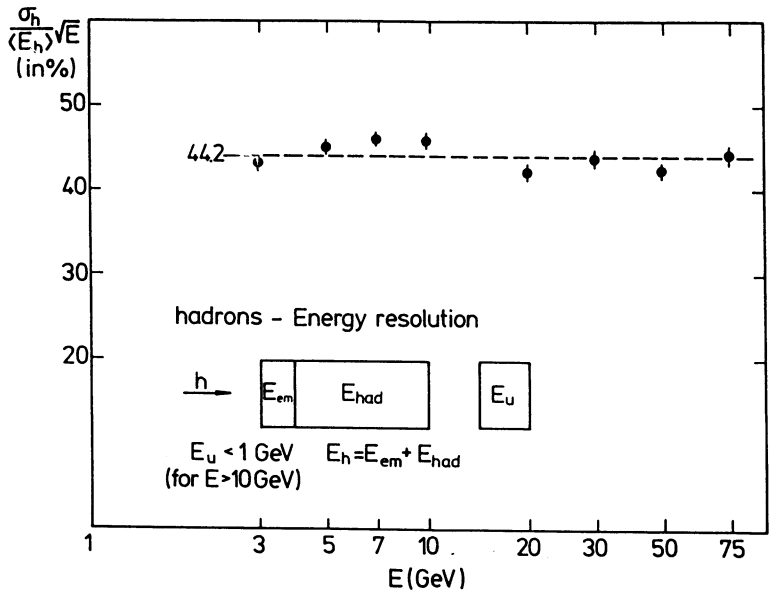

Figure 2.12: *The energy resolution for hadrons vs. the beam energy in a compensating lead/scintillator sandwich calorimeter [32].*

ing energy, which determines the intrinsic resolution, is worse for neutrons resulting from fission processes than for neutrons evaporating from the target nuclei themselves. Other advantages of using lead instead of uranium concern neutrons, the key element in making compensation. Lead produces fewer neutrons since it does not fission. This leads to less radiation damage to surrounding electronics by escaping neutrons. In addition, the neutron signal in a lead calorimeter is generally faster, than in a uranium calorimeter. The signal by neutrons in a lead calorimeter is produced mainly by recoil protons, a fast process (~10 ns), whereas, in uranium, neutron capture, with a time scale of ~1 μs, plays a major role in the signal [35]. This is because the cross section for neutron capture in lead is much smaller (0.17 b) than that in uranium (2.7 b). In lead, thermal neutrons therefore escape the detector before being captured in it [11].

The hadronic energy resolution for this compensating calorimeter is one of the best measured, but the e.m. energy resolution is much worse than good e.m. sampling calorimeters. This is because a small sampling fraction (3.8%) is necessary to satisfy the compensation condition, which then causes the sampling fluctuations to contribute much more to the resolution (sect. 2.3.1). Another calorimeter built by the ZEUS Collaboration with layers of 4 mm of lead and 5 mm of scintillator ($f_{\text{samp}} = 16.4\%$) in the e.m. section was also tested [34]. The e.m. resolution was measured to be $12.7\%/\sqrt{E} \oplus 1.2\%$. Therefore, a thicker readout layer and a much larger sampling fraction reduces the e.m. energy resolution greatly, at the expense of losing compensa-

	lead	uranium
e.m. total	23.5 ± 0.2	17.5
e.m. intrinsic	0.3 ± 5.1	2.2 ± 4.8
e.m. sampling	23.5 ± 0.5	16.5 ± 0.5
had. total	44.2 ± 1.3	34.5
had. intrinsic	13.4 ± 4.7	20.4 ± 2.4
had. sampling	41.2 ± 0.9	31.1 ± 0.9

Table 2.2: *The scaling factor of the resolution* $(\sigma/E)\sqrt{E}$ *for compensating lead and uranium sandwich calorimeters, both with scintillator as readout. Listed are the total resolution terms and the resolution due to intrinsic and sampling fluctuations. Other (instrumental) contributions to the total measured resolution are not listed [24, 34, 32].*

tion.

Another way to reduce the sampling fluctuations is to sample the shower more frequently, which increases the number N of shower particles detected and hence reduces the σ/E (sect. 2.3.1). This can be achieved by decreasing the layer thicknesses while keeping the same sampling ratio R_d. The active layer thickness, however, needs to be thick enough for easy construction and sufficient and uniform light output (thinner layers result in more reflections and thus greater light attenuation and more non-uniformities), and to keep the *e/mip* low for compensation (see sect. 2.2.1). In practice, the lowest acceptable limit for a calorimeter is 1-2 mm of scintillator [36]. A calorimeter with this readout thickness decreases sampling fluctuations from $1/\sqrt{N}$ to $1/\sqrt{2.5N} = 0.63/\sqrt{N}$, predicting an e.m. resolution of $\sim 13\%/\sqrt{E}$, much-improved over the $\sim 23\%/\sqrt{E}$ measured for the calorimeter with 2.5 mm thick scintillator layers [24].

One may also increase the sampling frequency by using scintillating fibers embedded in lead. The sampling contribution to the e.m. energy resolution is then smaller by a factor $1/\sqrt{2}$ with fibers than with plates, where the fiber diameter and the scintillator plate thickness are the same (*i.e.*, $\varnothing = t_{\rm act}$ in sect. 2.3.1). This was the motivation for the so-called "spaghetti" calorimeter. It turns out that the use of fibers has additional advantages, which are discussed in the next chapter.

Chapter 3

The Spaghetti: Plastic Scintillating Fibers

For a long time, scintillating material has been an important component in many detectors for high energy physics experiments. Scintillating *fibers*, as opposed to the more common blocks of scintillator, have existed for particle detection since the '50s, but have been successfully used only in the last decade [37, 38]. This is mainly a consequence of the improvement in the quality of the fibers in that time. An array of fibers has an obvious application in tracking detectors, since it can provide fine-grain position information. Fibers have also proven useful in calorimetry. Success with lead/scintillating-fiber e.m. calorimeters has encouraged the application of this combination to hadron calorimeters.

In this chapter, I first review the basic properties of scintillators and the optics of fibers. Then some applications for calorimetry are discussed, with the advantages and disadvantages of using fibers. Finally, the investigations into the actual fiber performance and characteristics are described, with the conclusions derived from these studies.

3.1 Scintillation and fibers

3.1.1 Scintillation mechanism

A scintillator is essentially composed of a material that emits light when excited. In organic compounds, this process of fluorescence occurs at the molecular level, when an excited molecule emits light as it decays to its ground state [39]. In this way, one can measure the light produced after an ionizing particle excites the molecules of the scintillator in order to measure some property of the particle.

In a typical fluorescing material, the light emission spectrum and the absorption spectrum overlap significantly, allowing a large part of the emitted light to be reabsorbed. The resulting light yield may be too small to be detected with any precision, especially after traveling through a large quantity of material to the light detector.

With the addition of other solutes to the base material, however, a more efficient light yield can be obtained. These solutes (called dyes) absorb the emitted light and re-emit at longer wavelengths, so that the incident and final spectra have little overlap. A typical plastic scintillator is composed of a base scintillating material, such as polystyrene or polyvinyltoluene (PVT), plus one or two wavelength-shifting dyes. The absorption and emission spectra of a typical plastic scintillating fiber is shown in fig. 3.1. The base material of this fiber is polystyrene.

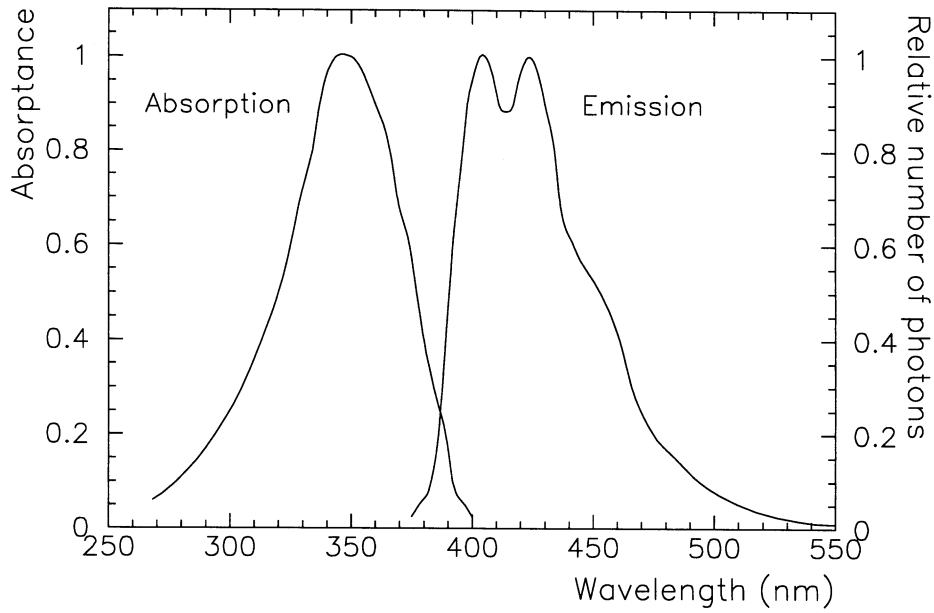

Figure 3.1: *The absorption and emission spectra for fiber type SCSF38, with a base material of polystyrene. The excitation source had a wavelength of 353 nm [40].*

Excitation of the scintillator base material is usually achieved by ionization by charged particles. According to Birks' model of scintillation, the light output per unit length dL/dx is a function of the specific ionization dE/dx [2]:

$$\frac{dL}{dx} = \frac{A(dE/dx)}{1 + k_B(dE/dx)}, \tag{3.1}$$

where A is the absolute scintillation efficiency and k_B is the parameter relating the density of ionization centers with dE/dx. For small dE/dx, this reduces to

$$\frac{dL}{dx} \propto \frac{dE}{dx}. \tag{3.2}$$

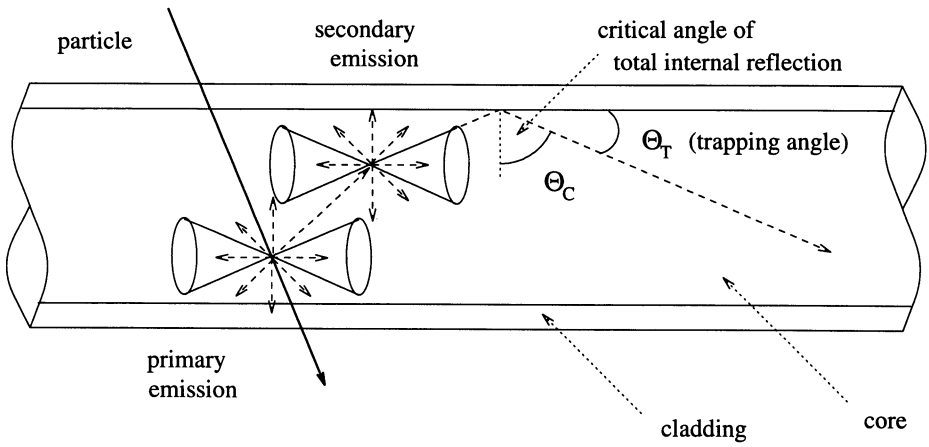

Figure 3.2: *The optics of light emission and transmission in a plastic scintillating fiber.*

A large specific ionization results in saturation:

$$\frac{dL}{dx} = \frac{A}{k_B}. \tag{3.3}$$

The light output reaches a constant, regardless of additional ionization energy.

3.1.2 Scintillating fibers

A plastic scintillating fiber consists of a *core* made of a doped scintillator, surrounded by an outer layer, called the *cladding*, of a non-scintillating material (fig. 3.2). The refractive index of the cladding (n_{clad}) is lower than that of the core material (n_{core}), so that the fiber becomes a light guide by total internal reflection. The critical angle θ_C, the minimum angle at which light is totally reflected at the interface of the two materials, is derived from Snell's law to be

$$\theta_C = \sin^{-1}\left(\frac{n_{\text{clad}}}{n_{\text{core}}}\right). \tag{3.4}$$

The light contained in the cone defined by $\theta_T = 90° - \theta_C$ therefore is guided to the end of the fiber. This trapping angle is typically 21° for $n_{\text{core}} = 1.59$ (polystyrene) and $n_{\text{clad}} = 1.48$ (PMMA[1]), and defines a trapping cone of 3.5% of the total light emitted at the fiber axis.

Light in a fiber is attenuated before reaching the light detector mainly by absorption and to a lesser degree by reflective losses at the core-cladding interface. The light

[1] polymethylmethacrylate, an acrylic plastic

intensity I measured a distance z from the source (from the primary scintillation of intensity I_0) is often expressed by

$$I(z) = I_0 e^{-z/\lambda_{\text{att}}}, \tag{3.5}$$

where λ_{att} is the attenuation length of the fiber. This expression, however, is only an approximation. The attenuation length actually depends on the wavelength of the emitted light. This is due to reabsorption of the components that lie in the region of overlap between the emission and absorption spectra of the fiber (see fig. 3.1). In eq. 3.5, λ_{att} is integrated over all the emitted wavelengths to which the light detector is sensitive. One should also include a term accounting for light that travels through the fiber cladding by reflection at the cladding-air interface, according to the attenuation length of the cladding λ_{clad}:

$$I(z) = I_0 e^{-z/\lambda_{\text{att}}} + I_1 e^{-z/\lambda_{\text{clad}}}, \tag{3.6}$$

where I_1 is the initial intensity of the light traveling this way. The cladding attenuation length is usually much shorter, since there are likely to be imperfections in the outer surface of the fiber which degrade the reflectivity of the cladding-air interface. The core-cladding interface is more protected. When $z \gg \lambda_{\text{clad}}$, the light traveling through the cladding does not reach the light detector and is therefore negligible [41, 42].

3.2 Fibers for calorimetry

The first applications of scintillating fibers in calorimetry were with e.m. calorimeters made of lead or lead alloys, with the fibers running at various angles from 0° to 90° with respect to the particle direction [43, 44]. The combination of lead and fibers was chosen for several reasons:

i. The lead scintillator combination is very dense ($X_0 \sim 1$ cm typically), making a compact calorimeter.

ii. Scintillators have an intrinsically fast response time.

iii. A high sampling frequency reduces the sampling term of the e.m. energy resolution (eq. 2.22). This is easier to achieve with fibers than with extremely thin scintillator layers in a sandwich geometry.

iv. The fibers are flexible and can be easily coupled to a light detector (*e.g.*, a photomultiplier), without losing hermeticity in the calorimeter (especially if the fibers are oriented close to or in the direction of the particle).

v. There exist scintillators that are radiation hard up to relatively high doses.

The most successful of these lead/scintillating-fiber e.m. calorimeters could compete with lead glass calorimeters in their performance, achieving an energy resolution of $4.7\%/\sqrt{E}$, with a volume ratio of lead to fibers to glue of 35:50:15 [44].

When the concepts of compensating hadron calorimetry were understood and were being applied to lead/scintillator calorimeters, the use of fibers was seen as a way to improve the hadronic energy resolution, as well as the e.m. resolution (sect. 2.3.2). This idea initiated the Spaghetti Calorimeter project [36]. The other properties listed above for e.m. calorimeters also apply for hadronic shower detection.

The basic design for the spaghetti calorimeter called for fibers of 1 mm diameter, which are easy to handle and provide the necessary sampling frequency to achieve good energy resolution. The fibers run (almost) parallel to the particle direction, with readout located in the back, providing hermeticity. They are arranged as a lattice in lead where each fiber is equidistant to the others, as seen in fig. 3.3. The proportion of lead and fibers is 4:1 in volume to satisfy the compensation condition. This makes the calorimeter compact, with an effective radiation length of 7.5 mm and a nuclear interaction length of 21 cm. An hexagonal module shape was chosen because it approximates a circle (symmetric in 2π), but can be stacked to make a hermetic detector. The cross section covers an area of 48.7 cm^2, allowing the fibers to be bundled in the back to fill an area approximately equal to the useful surface of a standard photomultiplier (PM) photocathode. A total of 1141 fibers fills one module.

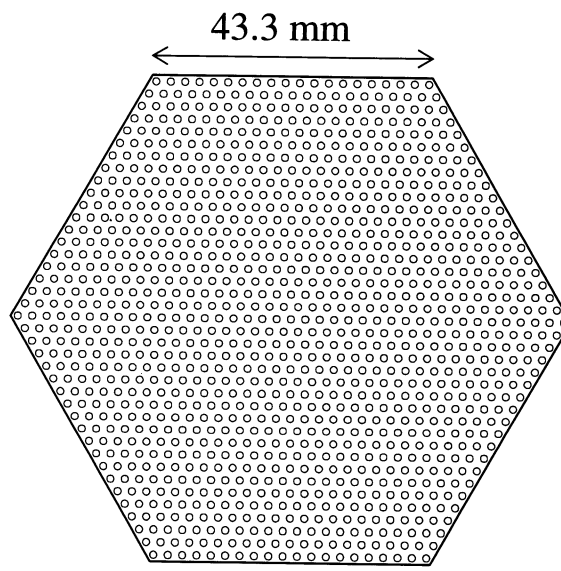

Figure 3.3: *The cross-section of one spaghetti calorimeter module. The fiber diameter is 1.0 mm and the distance between each is 2.2 mm, for a total of 1141 fibers.*

The intrinsic calorimeter performance may be improved by the use of fibers, but fibers can also deteriorate the performance through instrumental imperfections (bad fiber quality) or through particular intrinsic properties of the fibers. In the ideal calorimeter, the signal should be the same, independent of where a particle enters, requiring the fibers to have similar characteristics. In a calorimeter with fibers running parallel to the particles, non-uniformity among the fibers affects mainly the e.m. energy resolution, since only a small number of fibers are involved in producing a signal from an e.m. shower with its small dimensions. On the other hand, the fiber attenuation length is especially important for hadronic showers in a calorimeter of this geometry. Unlike e.m. showers, hadronic showers have large fluctuations in their starting point and depth (sect. 2.1.2), therefore the resulting signals (from particles of the same type and energy) can differ since they are attenuated over different lengths before reaching the light detector. A long fiber attenuation length would minimize these fluctuations. The light yield of the fibers, on the other hand, while lower than for scintillator blocks, is not a limiting factor for this type of calorimeter [45], since no separate, inefficient wavelength shifters are needed to transport the light to the PMs. Another potential disadvantage, high doses of radiation may cause a deterioration of both the fiber attenuation length and light yield in a non-uniform way, especially, but not exclusively, for the supercollider generation of detectors. Therefore, the fibers should be sufficiently radiation resistant for the application (sect. 3.3.3).

No glue is used in this design, to avoid damage to the fibers [46]. In addition, this allows the fibers to be replaced without dismantling the entire calorimeter, a possible scenario for regions of high radiation damage.

One can estimate some requirements for scintillating fibers in a compensating calorimeter. According to an EGS4 simulation of e.m. showers [47], if the response between fibers varies by no more than 6%, then the calorimeter should be able to measure the electron response with a 1% precision, and hence limit the effect of fiber-to-fiber fluctuations on the e.m. energy resolution to 1%, independent of energy.

One can also estimate the attenuation length required to limit the contribution to the hadronic energy resolution by longitudinal shower fluctuations. To first order, such fluctuations contribute $\lambda_I/\lambda_{\rm att}$ to the energy resolution for single protons and 50% more for single pions [12]. A more detailed study of these effects is described in [48]. The effect of these fluctuations to the lineshape of the signal distribution for pions was parametrized in agreement with experimental data. By varying the attenuation length in the parametrization, the curves in fig. 3.4 were found, where the energy resolution is taken from the $\sigma_{\rm RMS}$. Compensation is assumed, so that the entire constant term can be attributed to the attenuation length effect. From this, one sees that for attenuation lengths greater than 7 m, the resulting constant term is less than 5%. The energy-dependent term remains the same. Ideally, the fiber attenuation length should be longer than 15 m to limit the constant term to 2%. In practice, as it shall be shown, this was not easy to achieve with the fibers that were on the market at the time of the calorimeter construction. In sect. 4.4.2, it is shown how the effect of the attenuation on the hadronic shower signal can be removed on an event-by-event basis in this type

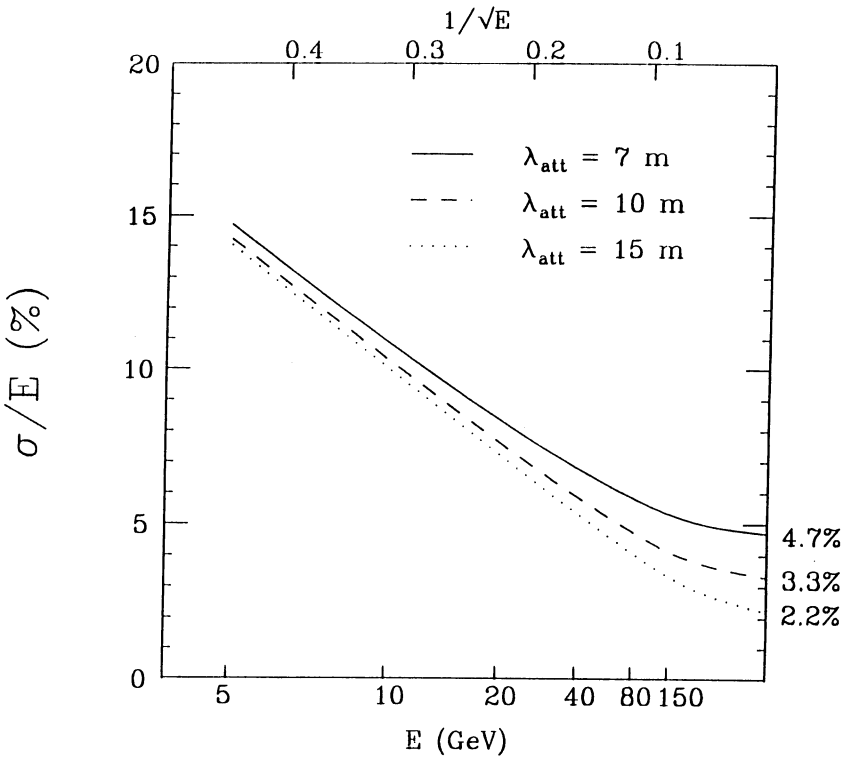

Figure 3.4: *The estimated energy resolution for pions in a compensating spaghetti calorimeter for various fiber attenuation lengths, according to a parametrization of the signal distribution lineshape. The lines are best fits to the calculations [48].*

of calorimeter.

Some ways of improving the fiber response are known [47]. The optical quality of the fiber should be good. They should be manufactured to be as similar as possible, both chemically and mechanically. Imperfections in the core-cladding interface should be minimized, as they deteriorate the uniformity and increase attenuation of the light before reaching the light detector. The effective attenuation length of a fiber can be increased by putting a yellow filter between the fibers and the photodetector. This cuts off the short wavelength (blue) component of the light, which is highly attenuated due to reabsorption. In addition, if the light traveling to the open end of the fiber is reflected (by a mirror of some kind), the effective attenuation length increases further. This is seen by including the light reflected by a mirror with a reflection efficiency R in the attenuation expression (eq. 3.5)

$$I(z) = I_0 \left[e^{-z/\lambda_{\rm att}} + R e^{-(2L-z)/\lambda_{\rm att}} \right] \tag{3.7}$$

where L is the total fiber length. This is frequently approximated by a single exponential

$$I(z) \approx I_0 e^{-z/\lambda_{\text{eff}}}, \tag{3.8}$$

where λ_{eff} is the effective attenuation length. We studied these techniques, with the results presented in the next section.

Even if the fibers are perfectly uniform, the rest of the readout chain may also introduce non-uniformities. Non-uniformity of the PM photocathode may deteriorate the energy resolution in the same way as large fiber-to-fiber fluctuations. A light guide for mixing the light helps minimize these effects. These elements were also investigated and the results are discussed in sect. 3.4.

In summary, the requirements ruling the choice of fiber and readout [49] were as follows, according to the chosen design of the calorimeter.

i. The fibers in the calorimeter should be uniform in their light response to within 6% to limit the contribution of fiber-to-fiber fluctuations to the energy resolution to the 1% level.

ii. The effective attenuation length should be sufficiently long, more than 7 m, in order to limit the effects of fluctuations in shower depth, such that the constant term of the energy resolution is less than 5% (quadratic fit).

iii. The fibers need to be robust, in order to withstand handling, machining, and polishing without damage.

iv. The diameter should be within 2% of 1.0 mm to fit into the modules, as well as to be uniform.

v. The optical readout (*i.e.*, light guide and photomultiplier) should should be uniform over the surface of a calorimeter module. In addition, it should minimize the variations in signal due to calorimeter non-uniformity.

3.3 Fiber studies

The fiber requirements for the calorimeter were satisfied as well as possible at the time by a type of fiber called SCSF38.[2] It has a polystyrene core surrounded by an acrylic cladding 29 μm thick, with the absorption and emission spectra shown in fig. 3.1. The emission spectrum peaks around a wavelength of 420 μm (blue), as shown in fig. 3.5a. When a yellow filter[3] is inserted between the fiber and the photodetector, the short wavelengths are cut, leaving an emission spectrum peaking at 460 nm (fig. 3.5b). The fiber response [47] is fast enough (the decay time of the wavelength shifting dyes is 2 ns), even for first-level trigger purposes. The fibers were cut into 2.2 m long pieces

[2] also known as SCSN38, manufactured by Kuraray Co. Ltd., Tokyo, Japan

[3] Kodak Wratten #3, cuts wavelengths below 450 nm

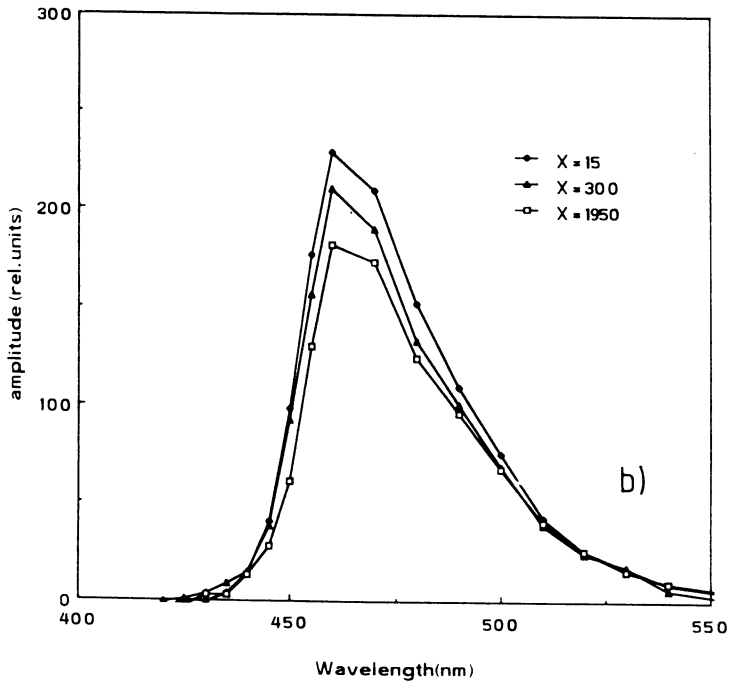

Figure 3.5: *The emission spectrum for an SCSF38 scintillating fiber, measured at several distances from the point of excitation, with a yellow filter inserted before the photodetector. The fibers were excited with a UV laser. Measurement described in ref. [47].*

during production and shipped unbent, minimizing damage to the fiber by bending. In addition, the shipments were divided according to preform[4] and "sub-preform" (*e.g.*, first tenth of the preform, second tenth, etc.). Fibers from the same preform, especially from the same part of the preform, are most similar to each other.

These fibers fulfilled the requirements on mechanical tolerance and robustness. The fiber attenuation length and light yield needed to be measured and improved, if necessary, to satisfy the requirements for the calorimeter energy resolution. For the construction of a calorimeter, the results from these measurements were used to combine similar batches together into modules, aiming to minimize fiber-to-fiber fluctuations within one module. Variations between the average signal from different modules were to be normalized later during inter-modular calibration. Also, the measurement of

[4] Fibers begin their scintillating lives as a preform, a polished block of the core scintillator material surrounded by a layer of the cladding material. The fiber is pulled from the preform as it softens at a sufficiently high temperature. When it cools and hardens, it is rolled up or cut into pieces at the end of the manufacturing process.

a certain percentage of fibers provided quality control where batches not meeting the requirements are rejected. These measurements are described in the following sections.

3.3.1 Measurement of single fibers

A system was devised and constructed to measure the light yield and attenuation length of individual fibers. Inside a light-tight box, a fiber was placed in a groove on a tray, with one end placed inside a holder which was fixed to the PM housing. Inside the PM housing, a cylindrical Plexiglas light guide coupled the fiber to the PM. This end of the fiber was polished by hand to ensure a reproducible optical contact with the light guide. The other end was only cut with a sharp blade. The photocathode of the PM[5] was sensitive to light of up to 650 nm, peaking at 450 nm. A yellow filter[2] was placed between the PM and the light guide, allowing light emission in the wavelength range of the photocathode sensitivity. A few mm above the fiber, a collimated ultraviolet (UV) lamp (emitting at 256 nm) was mounted on a track running along the fiber length, propelled by a motor. A potentiometer, over a constant initial voltage, turned with the motor wheel, so that the resulting voltage was proportional to the the position of the source. A computer recorded this position and the current from the PM at various positions (usually every 10 cm) along the fiber length.

A UV light source was used for the measurements since the resulting scintillation light intensity from a fiber is conveniently high, allowing fast measurements with reproducible results. Dedicated measurements yielded the same attenuation length for fiber excitation by a radioactive source. A photodiode mounted next to the UV bulb measured the lamp's stability to be better than 0.2%.

The measured light yield I from a typical fiber as a function of the distance z from the PM is shown in fig. 3.6. The two attenuation components, from the core and from the cladding, are apparent (eq. 3.6). The much steeper part of the curve comes from the shorter attenuation length of the cladding light, and disappears after $\sim$50 cm. Since most of the scintillation light from a shower in this calorimeter is produced more than 50 cm away from the PM, the attenuation length of the core λ_{att} is the important quantity. Therefore, fits to the simple attenuation expression (eq. 3.5) were made for z from 60 to 215 cm, as shown by the curve of the fit on fig. 3.6. The two unknown parameters of the fit, λ_{att} and I_0, are anti-correlated, and hence the resulting values are not independent.

The reproducibility of the measurement was checked by remeasuring the same fiber, taking it out of the box between measurements. The resulting spread in attenuation length was 7% and in light output 12%. The contributing factors to this spread due to the apparatus and technique were investigated, and some were eliminated before these measurements, but some remained unknown or uncorrectable.

A sample (5-10%) of the fibers from each sub-preform was measured with this setup. The average attenuation length after many such measurements on individual

[5] Philips XP2081B

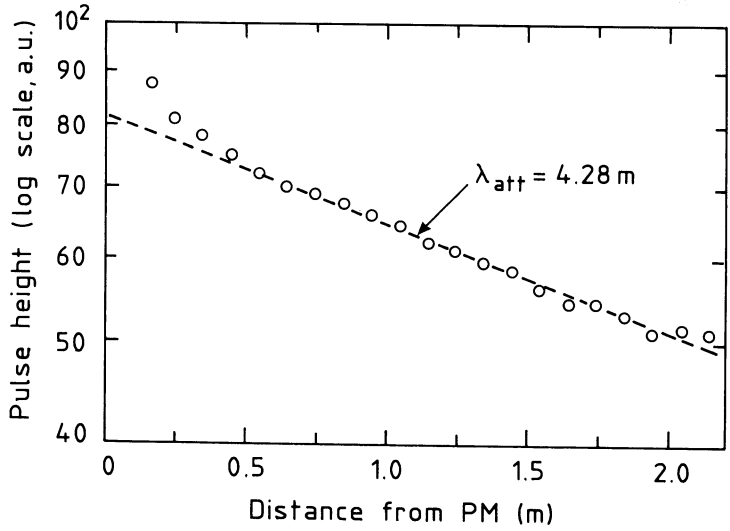

Figure 3.6: *The light output from a 2.2 m long SCSF38 fiber as a function of the distance between the UV light source and the PM. The curve is an exponential fit over the range 0.6 to 2.15 m. See text for details of the measurement.*

fibers (using the yellow filter) was 4.3 m, with an RMS spread within one sub-preform of ~22%. The spread in the value of I_0 was ~12%. One reason for such a large spread was the difference in the preparation of the open end of the fiber. The procedure was made to be as reproducible as possible while still being fast, but was not perfect. One consequence is that the reflectivity of the open end (a semi-smooth interface with air) differed from fiber to fiber and affected the fit to one exponential, which neglects (the usually small) reflection coefficient.

When the open end of the fiber was polished and a good mirror attached (see next section for details), the effective attenuation length increased by a factor of 2. This technique was therefore adopted for use in the calorimeter.

3.3.2 Measurement of fiber bundles

Before insertion in the calorimeter, the fibers were prepared in the following way. For each set of fibers coming from the same sub-preform, the average light yield and attenuation length were known from the single fiber measurements. Sub-preforms with similar characteristics were then grouped together for each individual calorimeter module. Several methods of applying a mirror to the fibers were investigated, the best accomplished by sputtering aluminum onto a polished surface. By measuring single fibers before and after aluminization in this way, the average reflection coefficient was found to be 85±4%. In order to polish and aluminize the fibers without damaging them, each group corresponding to a single module was bunched together and held

fixed by mechanical clamps. An industrial firm machined one end of each "rod" with a diamond-edged saw, effectively polishing the surface. Finally, another company sputtered aluminum on this end, and the fibers were ready for the calorimeter assembly.

Before and after a rod was polished and aluminized, its attenuation curve was measured, in effect giving the average characteristics of this group of fibers. The rods with the best attenuation length and light yield were identified for placement in the center of the calorimeter (where the test beam measurements are concentrated). In addition, the reflection coefficient could be determined by comparing the two measurements. The measurement was done in the following way. The rod was covered with a light-tight black cloth and placed on a 3 m long tray. The tray was motorized so it could move through an annular ^{60}Co source. The non-aluminized end (or the end not designated for aluminization) was coupled through an hexagonal light guide to a PM of the type to be used for the calorimeter. The measurement was otherwise the same as for individual fibers. The PM signal was measured every 5 cm and a fit to a single exponential function (eq. 3.8) was made to the data points between 105 and 205 cm from the PM, excluding the cladding attenuation effects. The reflection coefficient was determined by taking the signal closest to the open end of the rod, *i.e.*, $z \approx L$, before and after aluminization. The ratio of these values should be $1 + R$, following

$$\frac{I_{alum}(L)}{I_{non-alum}(L)} = \frac{I_0(e^{-L/\lambda_{att}} + Re^{-L/\lambda_{att}})}{I_0 e^{-L/\lambda_{att}}} = 1 + R. \tag{3.9}$$

Repeated measurements on rods without taking them out of the apparatus resulted in attenuation lengths varying by $\sim$ 3%. This setup therefore gave more reliable measurements than that for the single fiber measurements. The optical contact was less critical for such a large number of fibers, and the mechanical structure of the rods did not allow for the bending that was common with single fibers. The absolute position of the rod with respect to the source however had a larger uncertainty, since the tray was not fixed to the moving treads and often needed repositioning. Some alignment was done off-line by normalizing the end of the rod, signified by a large dip in signal when the rod was completely out of the source, to the same position.

After the measurement of 124 rods (see fig. 3.7), the average effective attenuation length was found to double after the aluminization procedure, from 3.3 m to 6.6 m, with a spread of the values over $\sim$22%. The value of I_0 also increased by 40%. The average reflection coefficient was found to be 93% with a σ_{RMS} of 10%. This value includes the effects of the polishing as well as of the mirror. Note that the region of the fit differs from that of the single fiber measurements. In addition, cross-talk between adjacent fibers is present in the rod measurements, making comparison with single fiber measurements difficult. These differences may account for the different values of $\lambda_{\rm att}$. Also, it should be noted that the distance over which the measurements were performed were much shorter than $\lambda_{\rm att}$, leading to large, asymmetric uncertainties in $\lambda_{\rm att}$. However, the results before and after aluminization were surprisingly consistent, considering that as much as a few weeks passed between between measurements on the same rod. The information, most applicable towards hadronic shower uniformity, was

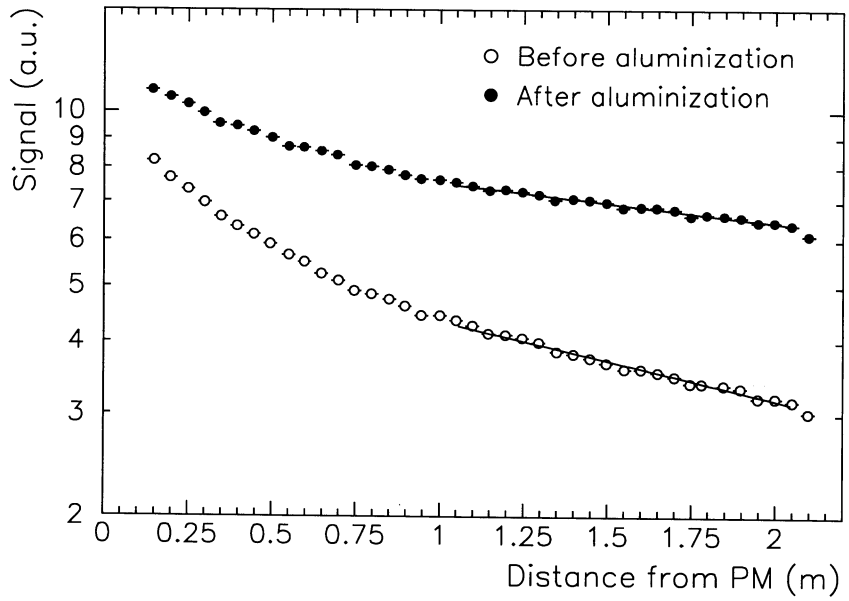

Figure 3.7: *The signal from a rod of fibers as a function of the distance between the PM and the ^{60}Co source, before (open circles) and after (closed circles) aluminization of the open end. The curves are the results of exponential fits from 1.05 to 2.05 m.*

used for the construction of the calorimeter. The rods with the highest attenuation lengths were placed in the central area of the calorimeter.

3.3.3 Radiation damage of fibers

Excessive radiation can damage plastic scintillator such as to decrease its light output. This may be due to loss in the light production and/or loss in the transmission of the light. A decrease in emission occurs when the number of scintillator molecules is lowered after some have been destroyed. Decrease in transmission is caused by increased absorption by the base plastic, especially in the UV and blue regions. In blue fibers, such as SCSF38, radiation damage mainly affects the transmission [50].

The subject of radiation damage in scintillating fibers is far from conclusive, with many results inconsistent or conflicting. Each scintillator composition has a different resistance. In addition, many factors can affect the extent of radiation damage in a particular scintillator. These factors, many dependent on each other, include the dose, the dose rate, the atmosphere before, during, and after irradiation, the temperature, and the size of the sample. The most reliable test of radiation damage of scintillating fibers in a calorimeter is therefore to irradiate such a calorimeter under conditions closest to the expected experimental conditions.

With fiber calorimeters, one wants to know how radiation damage affects the calorimeter performance, as gauged by the energy resolution. With radiation damage tests, the aim is to determine a limit on the irradiation after which the calorimeter performance degrades unacceptably. Tests and simulations were made with fibers alone as part of the research and development effort for the fiber calorimeter, from which the damage to a fiber detector under LHC conditions was extrapolated [50]. Radiation damage of an LHC calorimeter will result mainly from e.m. showers instigated by γs from π^0 decay, since all their energy is deposited in the early part of the calorimeter [51, 52]. Therefore, dose profiles similar to those deposited by e.m. showers were used in the tests. Favorable results were found for realistic detector parameters, allowing up to 7 Mrad for a decrease of 10% in the light output. At this dose level, a contribution of 0.8% to the constant term of the e.m. energy resolution and a 0.2% degradation of the hadronic energy resolution were found. Most of the radiation damage tests, like this one, are geared toward LHC conditions [53, 54], with none specifically simulating the hyperon beam conditions. It is estimated that a spaghetti calorimeter in the CERN hyperon beam (sect. 5.1.2) receives 10-100 krad in the most irradiated module from non-interacting 330 GeV beam particles (hadrons), over a running period of $2\frac{1}{2}$ weeks. This is well below the limits found in the studies above. For the initial beam period in WA89, the radiation dose should then not cause any visible damage to the fibers in the calorimeter. This is confirmed by the results presented in chapter 5.

3.4 Fiber readout

Non-uniformity of the calorimeter response is also minimized by reducing VARiations in the light collection from the fibers. The quantum efficiency of a typical PM photocathode may vary by more than a factor 2 over the sensitive area. This effect can be averaged by mixing the light coming from a fiber bunch before coupling it to the PM with the aid of a light guide. The behavior of the light in the light guide was therefore studied in order to understand and optimize this process.

In the tests, a single scintillating fiber, excited by a UV lamp, was scanned across the surface of a cylindrical Plexiglas light guide, which was coupled to a PM. It was found that the light mixing was not uniform. Light entering near the edge of the light guide was reflected (with some loss) at the Plexiglas-air interface more frequently than light entering the center of the light guide before reaching the PM. This non-uniformity was considerably reduced when a light guide with a square or hexagonal cross section was used. Fig. 3.8 shows the result of such a scan across a round and an hexagonal cylindrical light guide coupled to the same PM. In the circular light guide, the light entering near the edge may be reflected many times in a helical path to the other end. In a polygonal light guide, the path of the reflections is less symmetric, resulting in fewer reflections and hence less reflective loss before exiting the light guide.

The length of the light guide can also be optimized to reduce the effects of photocathode non-uniformity. Scans over hexagonal light guides of various lengths were

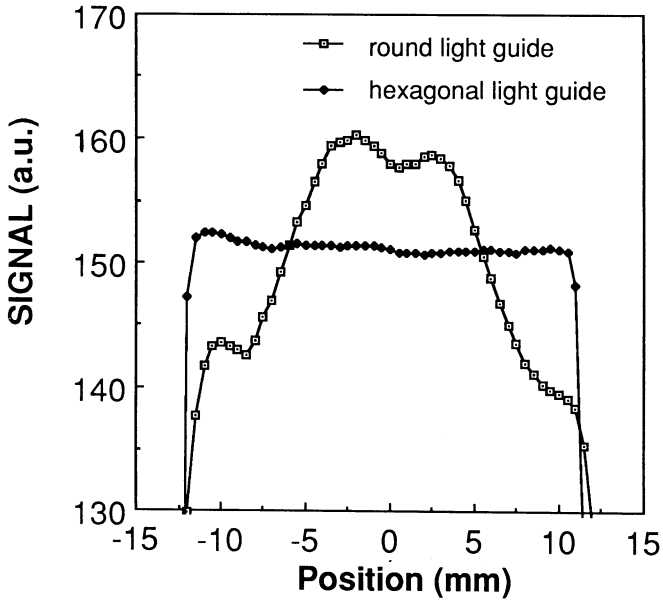

Figure 3.8: *The response to a fiber scanning the surface of a circular and of an hexagonal light guide of the same length, using the same PM [49].*

made, shown in fig. 3.9. The shorter light guides mix the light insufficiently and show some of the non-uniformity of the photocathode surface. An hexagonal light guide 79 mm long and 42 mm apex-to-apex was finally selected as the optimal choice for this calorimeter.

The tests above were made using a PM with a particularly non-uniform photocathode. For the calorimeter, PMs of type XP2282B[6] were individually selected for their smooth photocathode efficiency. In addition, the spectral range of this PM is from 300 to 650 nm, peaking at about 400 nm, matching the emission spectrum of an SCSF38 fiber with a yellow filter. Its gain is relatively low, between 10^4 and 10^5, but is sufficient for the calorimeter's large light yield ($\sim 470 \pm 25$ photoelectrons/GeV) [45].

3.5 Conclusions of fiber studies

Drawing upon results of the various studies presented in this chapter, the calorimeter design calls for fibers to be inserted into the lead without glue, which may damage the plastic fibers. The fibers are grouped in a module such that the fiber-to-fiber differences in light output are minimal. The end of each fiber opposite the light detector is polished and sputtered with aluminum. The fiber readout includes an hexagonal light guide of

[6] Philips, 8-stage

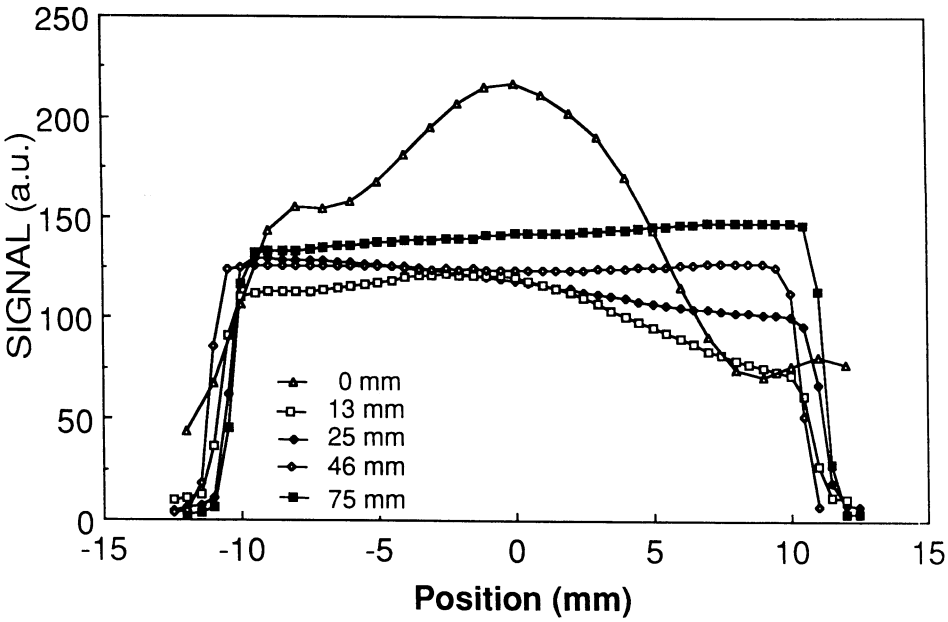

Figure 3.9: *The response to a fiber scanning the surface of hexagonal light guides (25 mm apex to apex) of various lengths [49].*

optimal length to couple the fibers to a PM, which is equipped with a highly uniform photocathode. A yellow filter between them is used to cut the highly attenuated blue light emitted by the fibers. The next step is to build and test the calorimeter.

Chapter 4

The Preparation: A lead and scintillating fiber calorimeter

With lead (and its good intrinsic resolution) and fibers (and their high sampling capability), it is possible to build a precision compensating calorimeter fulfilling the following characteristics:

- good energy resolution,
- a linear response within the required energy range,
- hermeticity, with all readout in the back of the detector,
- good particle identification,
- fast signal production,
- construction with materials that are inexpensive, easy to work with, radiation resistant, and long-lasting.

The SPAghetti CALorimeter (SPACAL) project set forth to build a calorimeter with these goals in mind, aiming for use of this technique in a supercollider environment. It was not originally intended for use in the hyperon beam experiment WA89 (chap. 5), but this environment is less harsh, with a lower rate and energy than a supercollider. Hence, the requirements are not as stringent as for a supercollider experiment.

The calorimeter performance was gauged by a series of beam tests on several prototypes and the final calorimeter, in which many of its properties were measured. The final, 155-tower calorimeter, originally built as a prototype to contain a full hadronic shower, is the one used in WA89. In this chapter, the construction and performance in a test beam are described, with emphasis on those characteristics especially important for neutron detection in WA89. Some of the interesting measurements made with the smaller prototypes are also presented. All the results from the SPACAL research and development program can be found in ref. [49, 50, 55, 56, 57, 58, 59, 60, 61, 62].

4.1 Construction

Several small lead/scintillating-fiber calorimeter prototypes were constructed according to the basic design described in sect. 3.2. The cross section of one detector cell (the same for all the prototypes), as shown in fig. 3.3, is a hexagon measuring 86 mm apex to apex, containing 1141 scintillating plastic fibers of 1 mm diameter. The fiber-to-lead volume ratio is 1:4, resulting in $X_0 = 7.5$ mm and $\lambda_I = 21$ cm. The first modules were only 20 cm long (26.6 X_0), intended for the detection of e.m. showers. Later, modules of 2 m ($9.5\lambda_I$) in length were built, providing the depth necessary to contain hadronic showers at a sufficient level. Next, a 20-cell, 2 m long prototype (fig. 4.1) was constructed as one piece, with no modular segmentation. This prototype contained full e.m. showers. Finally, the same method of construction was used for the 155-cell calorimeter, the full hadronic/e.m. calorimeter (fig. 4.2). It consists of a central tower (numbered 1) surrounded by seven concentric hexagonal rings, the last one incomplete.

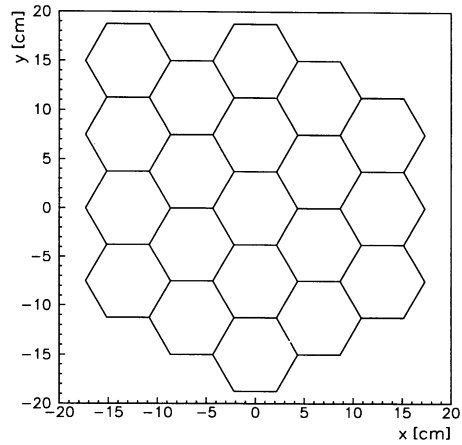

Figure 4.1: *Cross-sectional view of a 20-tower calorimeter prototype. The beam direction is into the page.*

Several methods of constructing the lead modules were used [49]. Since no glue is used in the design, a module was to be made, then the fibers inserted later. To build the first modules, molten lead was poured into an hexagonally shaped cylindrical mold around 1141 steel tubes, held in their equidistant positions by spacers placed every 10 cm. This technique was successful for the short e.m. modules, but, for a longer module, it was difficult to keep the tubes from getting displaced during the molding process, especially if the spacers were further apart than 10 cm. In such a case (fig. 4.3, left), the fibers were no longer equidistant between the spacers, which leads to non-uniform sampling and an increase in the energy resolution. A more successful method involves the extrusion of 2 m long lead plates with grooves, as shown in fig. 4.4. Ideally,

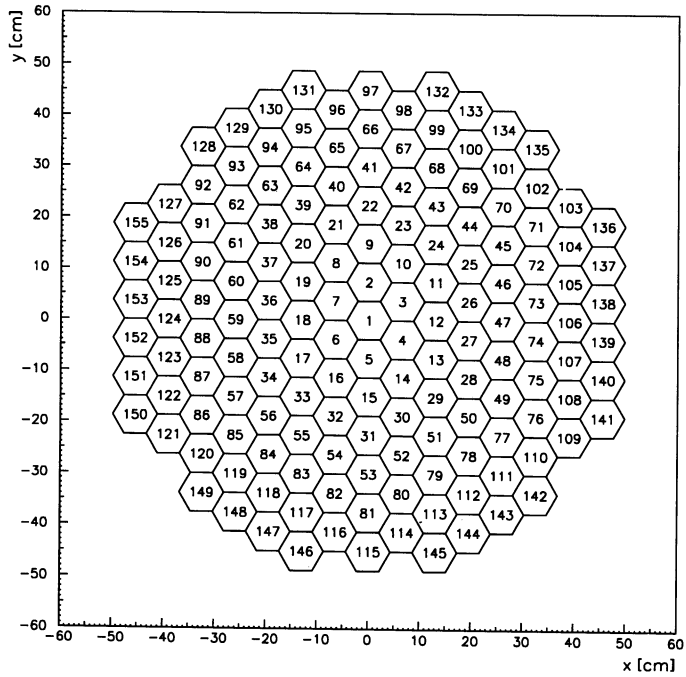

Figure 4.2: *Cross-sectional view of SPACAL. The beam direction is into the page.*

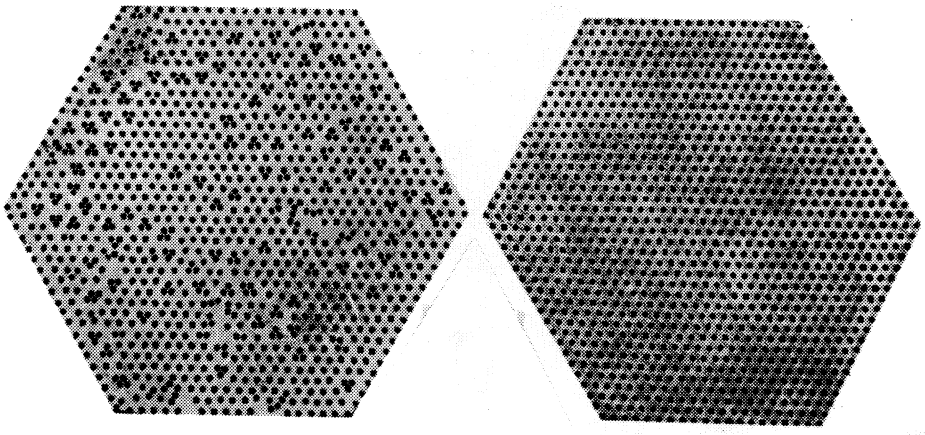

Figure 4.3: *The lateral cross section, at a certain depth, of SPACAL modules made according to the casting method (left) and the extrusion method (right) [49].*

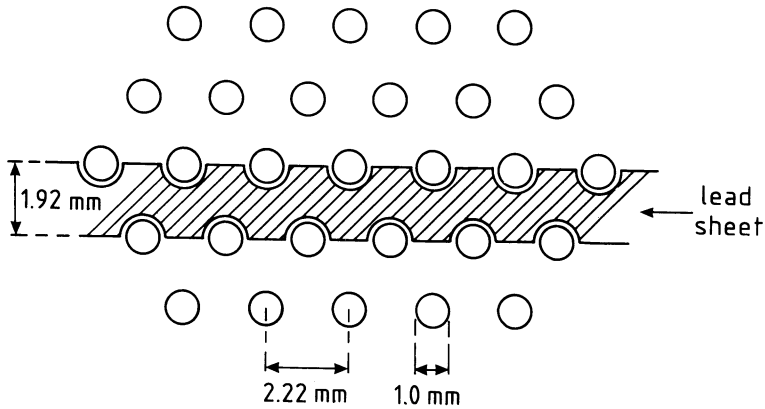

Figure 4.4: *Detail of cross-section of a lead/scintillating fiber calorimeter constructed using the extrusion technique.*

the sheets are tinned and soldered together in an oven to form a module. This was a successful technique for one of the small modular prototypes (fig. 4.3, right). This stage of the process, however, had not been fully operational at the time of the construction of the 20- and 155-cell prototypes. (See [45] for a description of modules successfully constructed by this method.) These prototypes were therefore built as one structure, by piling alternate layers of lead sheets and fibers, held together mechanically. Groups of fibers making up approximately the same hexagonal shape as a module were grouped together for the readout.

The SCSN38 fibers, polished and machined at the front end (chap. 3), were inserted into the modular prototypes; in the case of the large prototypes, they were laid out in the grooves of the lead sheets during the piling. The readout of the fibers was the same in both cases. The 1141 fibers from the detector cell were grouped together into an hexagonal bunch, as shown in fig. 4.5, and held together by a clamp. An aluminum hexagonal tube, with the same dimensions as a module, houses a Plexiglas light guide and a PM (sect. 3.4) within molded foam and mu-metal (fig. 4.6).

4.2 Test beam setup and data treatment

4.2.1 The beam line

The beam tests with the SPACAL prototypes took place in the H2 beam line of the SPS at CERN. High-precision beams of electrons and negative pions between 5 and 150 GeV were sent into the calorimeters. The momentum of the beam was known to $\Delta p/p = 0.7\%$ at 5 GeV and to 0.1% at 150 GeV. At energies higher than 40 GeV, the beams were very clean, with few ($\ll 1\%$) electrons (pions) in the pion (electron) beam. This was different for the beams with the lowest energies (5 and 9.7 GeV), which

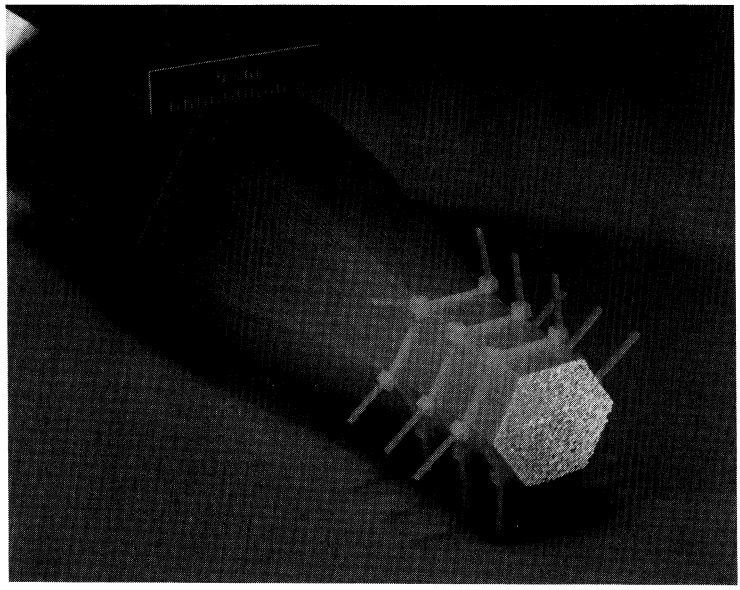

Figure 4.5: *The back end of a calorimeter cell, before the readout is attached. The fibers extended 15 cm past the lead and were grouped together to form an hexagonal shape amounting to 23% of the lateral cross section of a tower.*

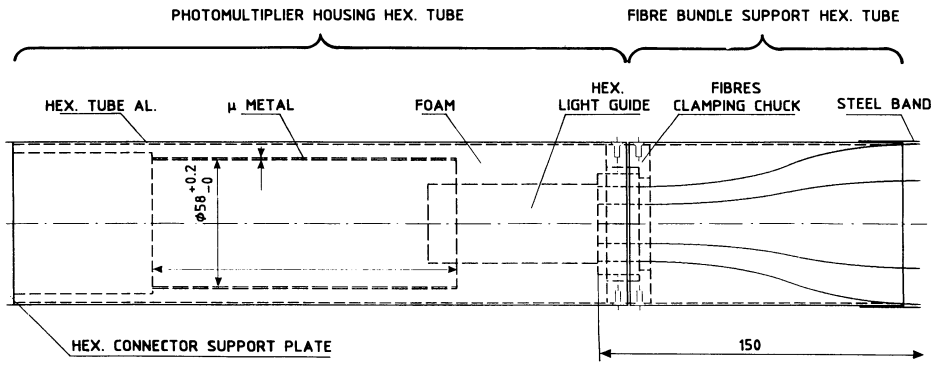

Figure 4.6: *The mechanical structure of the readout of a calorimeter tower.*

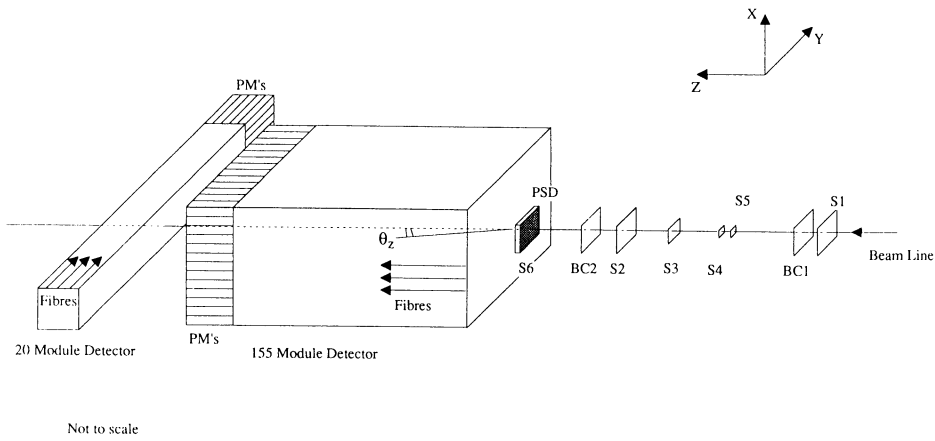

Figure 4.7: *Layout of the beam line, not to scale. See text for details.*

required cuts to reject the contaminating particles. The pion beams also contained a significant fraction of muons, ranging from 2% at 150 GeV to 80% at 5 GeV.

The layout of the beam line for the tests with the large calorimeter is shown in fig. 4.7. The elements upstream of the calorimeter were arranged in essentially the same way for the tests of the smaller prototypes. A coincidence of a combination of the scintillator counters S1 to S5 defined the trigger for the data readout. The small finger counters S4 and S5 were left out of the trigger when the rate of particles was low (usually at low energy). The two proportional wire chambers BC1 and BC2 recorded the position of the beam particles with a precision of ~0.5 mm. A pre-shower detector (PSD) was installed ~12 cm upstream of the calorimeter. For the tests with the 155-tower calorimeter, it consisted of an absorber of $1.14X_0$ of tungsten and $0.53X_0$ of lead, followed by a scintillation counter (S6). The signals from S6 provide discrimination between electrons and pions, since electrons usually shower in the absorber and pions only deposit a MIP signal. The PSD signal was included in the trigger at the lowest beam energies (5 and 9.7 GeV).

The detector was placed on a support that could move horizontally and vertically with a precision of ~1 mm. The detector could also be rotated to change the angle θ_z between the fiber and beam directions to better than 0.1 mrad. It was nominally placed with fibers running $\theta_z = 3°$. The smaller, 20-tower version of the large calorimeter was placed downstream with the fibers running perpendicular to the beam direction for muon detection and longitudinal leakage measurements.

The signals from the PMs were treated as shown schematically in fig. 4.8. Inside the base, the anode signal was passively split into two outputs, one going to a linear adder[1] with the other PMs from the same ring of towers, the other providing the individual PM signal. Both this output and the output from the linear adder (the sum of each

[1] LeCroy 628

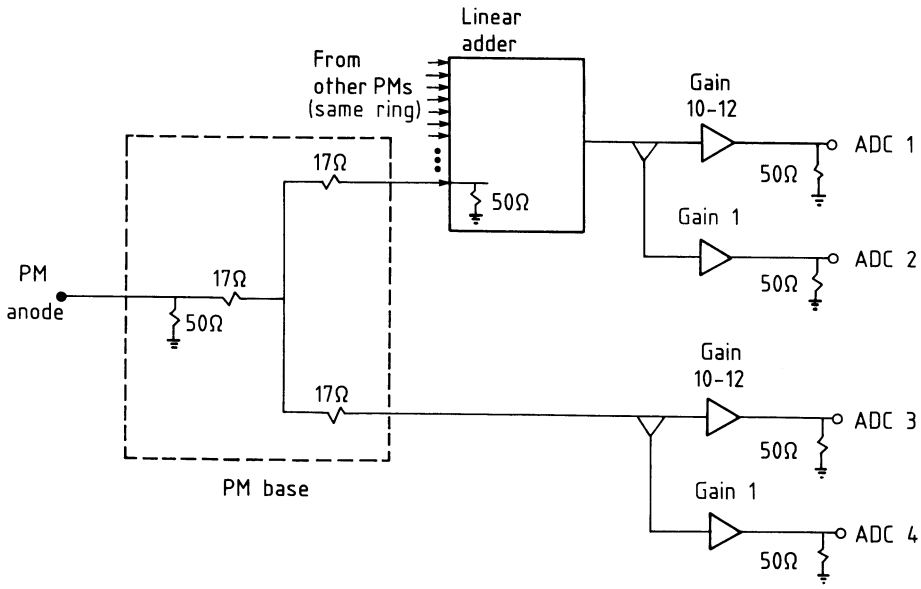

Figure 4.8: *The handling of the photomultiplier signals. See text for details.*

ring) were then handled in the same way. They were first divided into two by an active splitter. One output was amplified by a known factor between 10 and 12 before being digitized by a 12-bit charge ADC[2]; the other was only buffered and digitized. The amplification provides finer resolution on small signals, increasing the effective number of bits by 3-4.

Sparse data readout was enabled by recording only signals more than 4 counts above the pedestal value from each tower. This resulted in an underestimation of the sum of the signals, since small energy deposits were not included. The low-energy hadronic shower energy measurements were especially affected. For the study of lateral shower profiles and the e/h determination, an estimation of the missing energy was made and added to the initial energy measurement [56, 61].

4.2.2 Calibration of the calorimeter

The first step of the calibration was to adjust the high voltage level of each PM to reach a certain gain. About 1500 electrons of 40 GeV were sent into the center of each tower. The gain of the PMs in the central region was set to deliver ~4 pC/GeV, and was increased gradually moving away from the center, up to ~20 pC/GeV in the outer ring. The ADC gain was 4 counts/pC. This scheme increases the sensitivity to the smaller energy deposits in the outer rings, assuming a particle entering the central

[2] LeCroy system 2280, with 2282E modules

region of the calorimeter. Otherwise, the dynamic range of the ADCs is not sufficient to detect both the large and small energy deposits. For the tests with the 20-tower calorimeter, the gains were all set (by the same method) to ~4 pC/GeV.

The data taken at the final voltage was then used off-line to determine precise calibration constants for all the towers. These were found by a matrix calculation based on the energy sharing between the towers, a method that is described in detail later in sect. 5.3.3. For the 20-tower calorimeter, the constants were only determined by the mean of a Gaussian fit to the signal distribution of each tower when the beam enters its center. The accuracy of the calibration was limited by the signal uniformity over a tower of ~3% [58].

4.2.3 Event selection

In order to ensure that only events induced by one of the desired single particles were used in the analysis, it was necessary to make a selection of the data samples in the following ways.

Cuts were made to ensure that a single particle was entering the calorimeter at a time. The pulse heights of the signals from the scintillators S1, S2, and S3 were required to be between 0.5 and 1.7 the MIP value. The positions measured by the two beam chambers had to agree within 1 cm in both x- and y-directions. In addition, beam halo particles were removed by cuts on the beam chamber positions.

Cuts on the pulse height from the pre-shower detector (S6) removed electron (pion) contamination of the pion (electron) beams. For pions, which act like MIPs in the PSD, the pulse height was required to be less than twice the MIP value, while for electrons it was required to be more than that.

Muons were removed from electron or pion beams by requiring the energy deposit in the leakage calorimeter to be less than 125 MeV [59]. Muons traversing this detector were measured to deposit more than this amount, while electrons deposited no energy in the leakage calorimeter. This cut also removed pions having a significant amount of longitudinal leakage. After showering in the $9.5\lambda_I$ deep SPACAL, the fraction of pions depositing more than 125 MeV in the leakage calorimeter ranged from $< 1\%$ at 10 GeV to $\sim 14\%$ at 150 GeV.

Additional cuts to remove muons using the calorimeter information supplemented the cut on the leakage detector measurement or were used in place of this cut for the study of shower leakage. Other cuts were also necessary for the lowest energies where this method was less efficient. Muons were easily detected at high energies since they deposited less energy in the calorimeter than electrons and pions did, making a cut only on the energy possible. At the lowest energies (5 and 9.7 GeV) the muon signals were very close to the pion signals, and so we needed another selection criterion, which makes use of the difference in lateral energy deposit patterns between pions and muons. The criterion is the fraction f_n of the energy contained in the n towers with the highest energy deposit. The fraction f_6 is plotted against the full calorimeter signal in fig. 4.9 for the 9.7 GeV pion and electron beams. In the top plot for pion beam, there is a clear

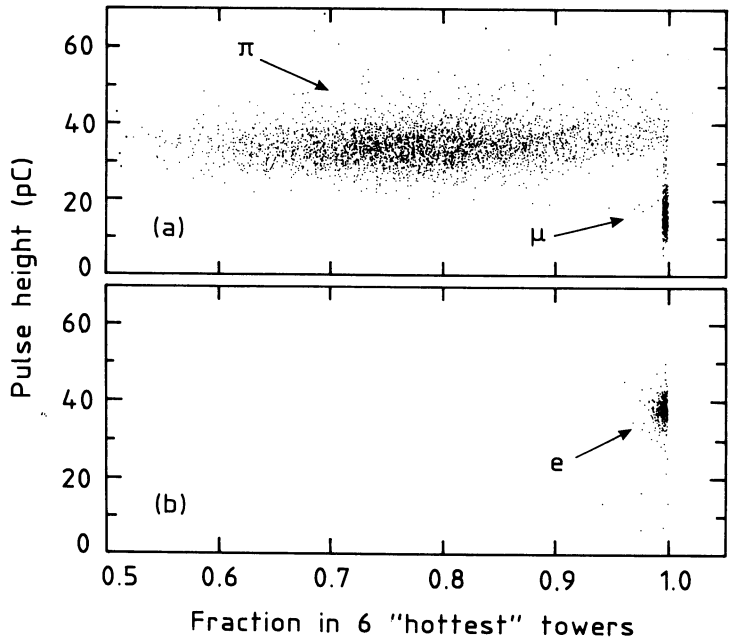

Figure 4.9: *The pulse height measured in SPACAL as a function of the fraction of energy contained in the 6 "hottest" towers, for events from the 9.7 GeV (a) pion beam and (b) electron beam.*

separation between the f_6 values for pions and muons. As muons only deposit their energy by ionization, they only produce signals in a few towers, while the pion showers are spread over many towers and are rarely contained in these 6 towers. Therefore, a requirement of $f_6 < 98\%$ removes most of the muons, with a small amount of pions. In fig. 4.9*b*, the same is shown for the electron beam, which contains almost no muons. However, this same criterion can be used to separate electrons from pions. For the electron beam, $f_6 > 98\%$ was required in the data selection.

4.3 Electron detection

One of the features of the SPACAL important for WA89 is the ability to separate e.m. and hadronic showers. The calorimeter was originally intended as an integrated e.m. and hadronic calorimeter, without the need for a separate e.m. calorimeter, which degrades the performance of the hadronic part. Therefore, the studies made with electron beams are relevant to the calorimeter's application in WA89. Some of the electron results were obtained from studies with the small prototype detectors. Since these prototypes were large enough to contain e.m. showers and their structure is the

same as that of the final calorimeter, these results can be applied to the final calorimeter as well.

In the SPACAL design, almost an entire e.m. shower is contained in one tower when the particle enters the center. Fig. 4.10 shows the lateral profile produced by electrons at 80 GeV in the 155-tower calorimeter [61]. Each point represents the signal in a tower as a function of the distance between the tower center and the center of gravity of the shower. Approximately 95% of the shower is contained in one tower, and the lateral shape is practically independent of the particle's energy. An e.m. shower is then fully contained within a central tower surrounded by 2 rings (19 towers), with an effective radius of 17.1 cm, allowing many of the tests with electrons to be done with the 20-tower prototype. The signal for an e.m. shower in the 155-tower calorimeter was defined as the sum of the signals of 37 towers, comprising the central tower plus the three surrounding rings (within an effective radius of 23.9 cm). The shower is more than adequately contained, such that adding more towers does not change the

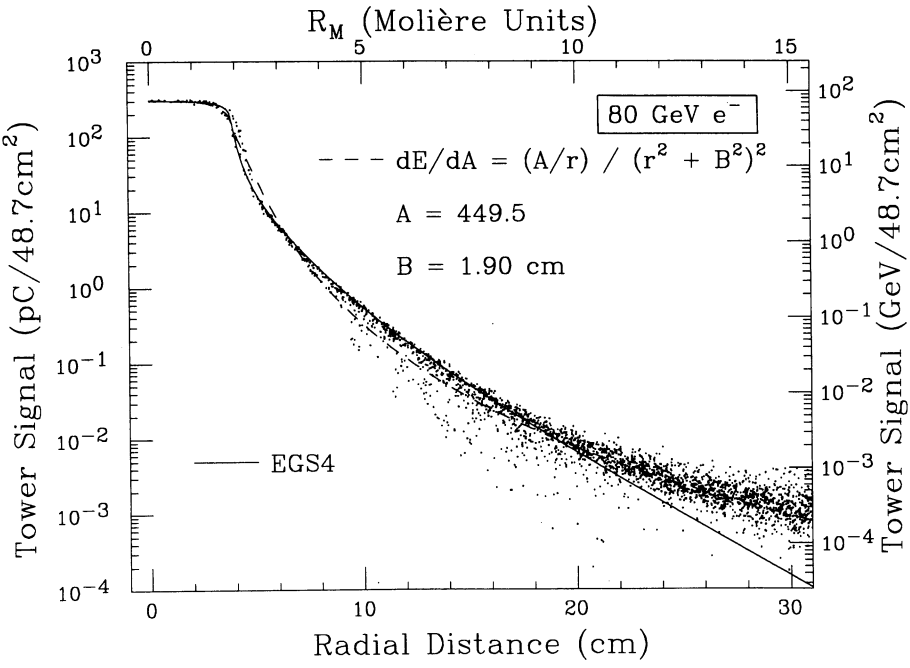

Figure 4.10: *The lateral shower profile for 80 GeV electrons entering the calorimeter at $\theta_z = 2°$ at various positions. The signal in a tower is plotted as a function of the distance between the tower center and the axis of the shower. The solid curve is a calculation based on EGS4, and the dashed curve is the best fit of the function written above [61].*

resulting signal [58].

4.3.1 Angular effects

The calorimeter is oriented such that the particle travels almost parallel to the fibers. This allows the fiber readout to be at the back of the calorimeter, making the calorimeter hermetic. It also causes some peculiar (but understood) behavior with such a geometry. One such case is the angular dependence of the signal.

A scan was made by varying the angle θ_z between the fiber axis and the particle direction, with a small $26.6X_0$ deep e.m. module [49]. The signal distributions for 40 GeV electrons are shown in fig. 4.11 for angles between 0° and 5.9°. Anomalously low signals are present at very small angles, below ~0.1°, and a high-energy tail on the distribution is present up to ~1°. The signals in the low-energy tail result from the particles that enter the calorimeter at a fiber position and travel without touching any lead and showering. This channeling results in a MIP-like signal. Other particles may enter a fiber at a small angle and travel some distance before leaving the fiber and initiating a shower. This type of shower may leak out the back in the area of the fiber bunching, where the shower particles are highly sampled and produce an anomalously high signal. This was also observed in calorimeter modules that were too short, with the leakage particles producing anomalously high signals. At larger angles, the particle enters the lead at an early stage, and no erroneous sampling occurs.

Since this effect is the result of a short detector, one would expect these angular effects to be absent in the longer 155-module detector, in which a particle is unlikely to channel for the entire length. Indeed, the low-energy tails completely disappeared. However, a high-energy tail on the signal distribution for electrons in a $266X_0$ long module, with the same length as the final calorimeter, was observed for angles up to ~1°, suggesting an additional cause for this effect. The early part of a high-energy electron shower has small lateral dimensions, indicating that most of the shower particles in this part travel in the direction of the incident particle close to the shower axis. Consequently, if the particle enters the calorimeter near a fiber axis at a small angle, most of the energy carried by the early part of the shower is deposited in the fiber. In effect, the sampling fraction is increased for such showers. This also implies that the sampling fraction depends on the impact point of the particle, since the effect just mentioned will be absent for electrons entering in the lead between two fibers. At larger angles of incidence, the differences between these two extreme cases are rapidly smeared out (as discussed in the next section). In order to avoid these effects and be sure of Gaussian signal distributions, the calorimeter was oriented at θ_z of 2° or 3° for most of the beam tests.

4.3.2 Uniformity

As discussed in the last two chapters, a uniform calorimeter is very important for an accurate energy measurement. First of all, the signal should be independent of

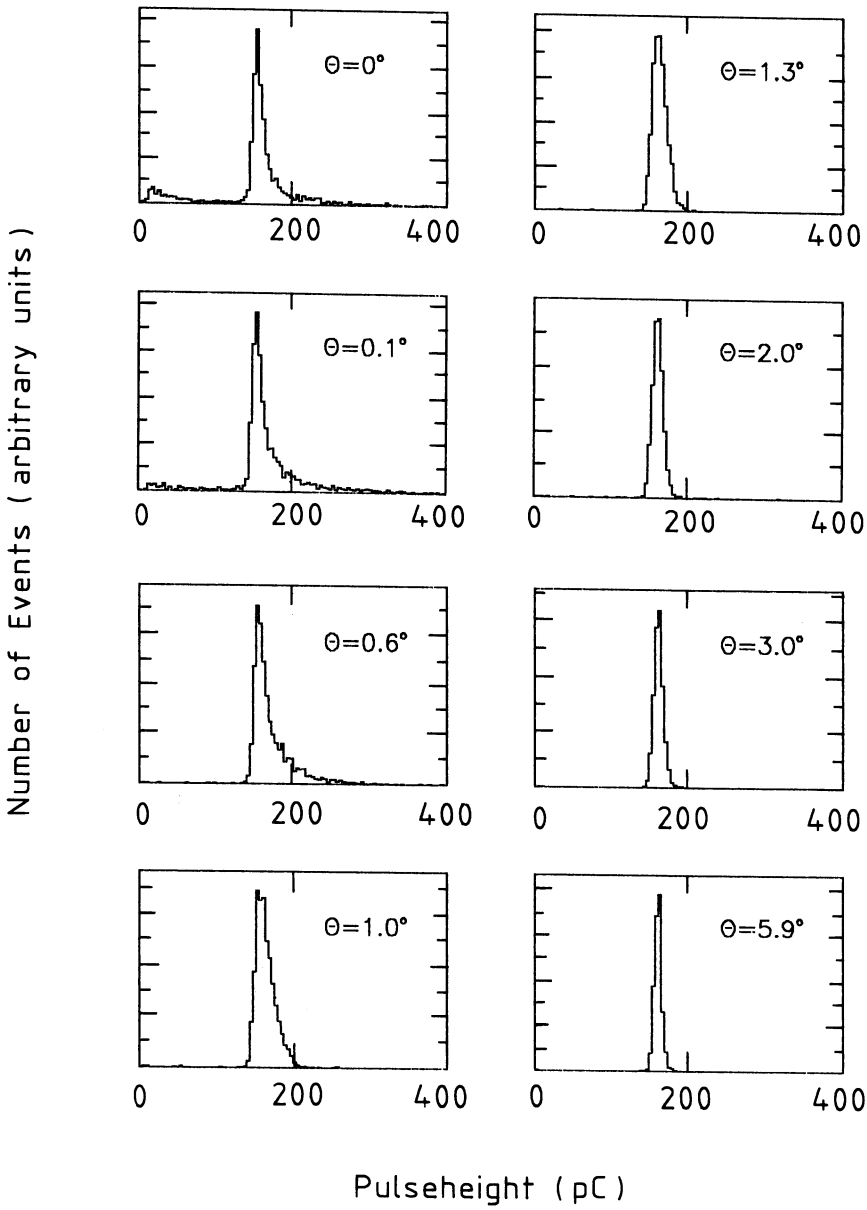

Figure 4.11: *Signal distribution for 40 GeV electrons entering a fiber calorimeter at various angles θ_z with the fiber axis, in a 26.6X_0 deep module [49].*

position of the shower in the calorimeter to avoid corrections based on position. Second, non-uniform response contributes to the energy resolution, and should therefore be minimized.

An 80 GeV e^- beam was scanned across the surface of the calorimeter, covering an area of 144 cm^2 around the center. The resulting average signals in 3×3 mm^2 sub-areas are shown in fig. 4.12 [58]. The average signal was found to vary with a

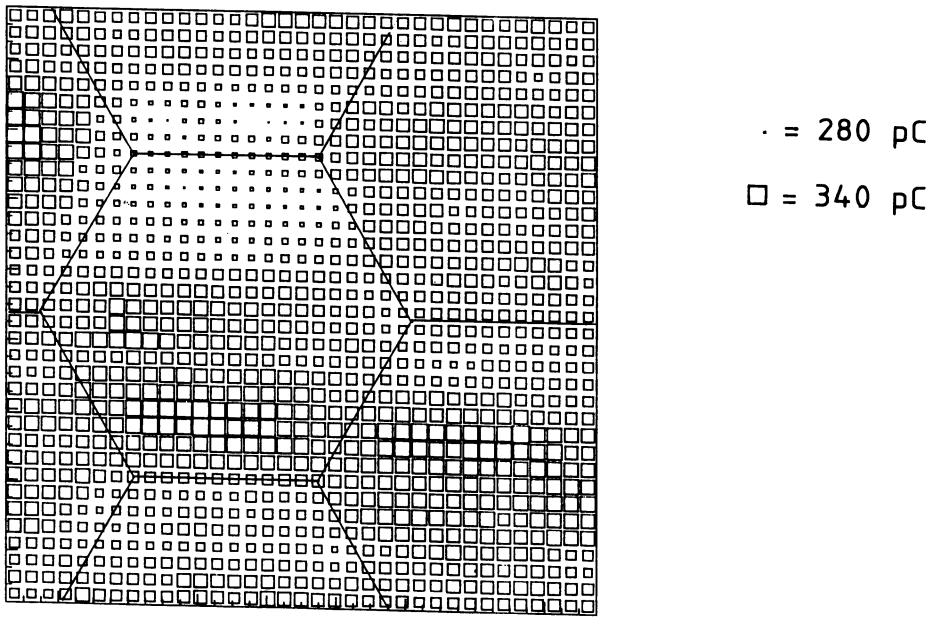

Figure 4.12: *The average signal for 80 GeV electrons entering the central region of the calorimeter at many impact points. The size of the squares indicate the numerical value, with the scale as indicated [58].*

standard deviation of ~3%. Fig. 4.12 does not show any obvious edge effects between calorimeter cells. The calorimeter is uniform between towers, since it was built as one unit, not as separate modules. The signal over the central tower, the one used for most of the tests, varies more than in most other towers. Observation by eye of the fibers at the readout end showed that this is due to differences between the fibers used in this tower. The signal produced when an electron enters the middle of this tower however is average compared to signals from other positions in the central region of the calorimeter, and thus can be assumed to be representative of the calorimeter as a whole.

On a finer scale, a non-uniformity in sampling of e.m. showers was discovered [58] and is shown in fig. 4.13. The periodic variations of the average signal with the impact point of the electron are consistent with the fiber spacing. This effect has the same

origin as the angular effects described in the previous section. In the early part of an electron shower, the lateral shower dimensions are small, with the shower particles emitted primarily in the direction of the incoming electron. The sampling fraction for the early part of the shower, and hence the total calorimeter signal, therefore depends on the impact point of the electron, The result is that electrons impacting on a fiber generate a larger signal than those impacting on the lead. Both this and fiber-to-fiber non-uniformity contribute to the energy resolution, as discussed in sect. 4.3.4.

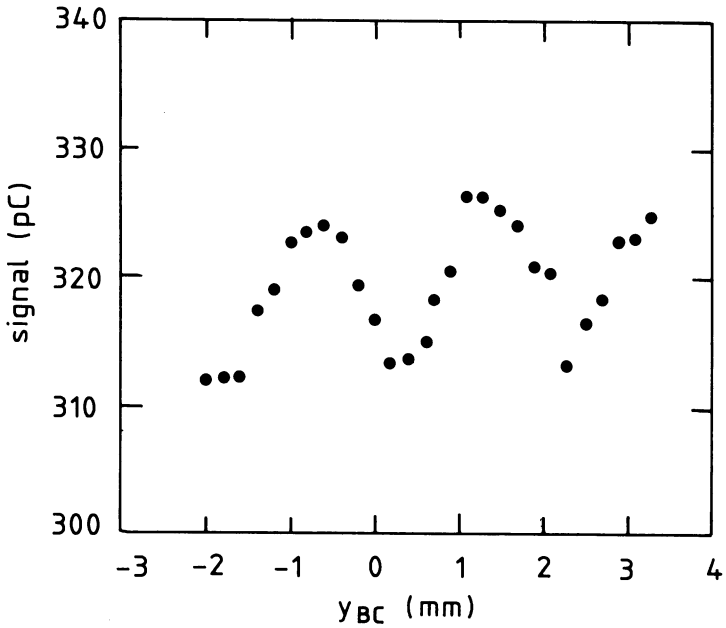

Figure 4.13: *The calorimeter signal as a function of the impact point in the vertical direction, for 80 GeV electrons at $\theta_z = 3°$ [58].*

4.3.3 Position measurement

The position of the center of gravity (or barycenter) of a shower in SPACAL can be determined from the sharing of the shower energy by neighboring towers. The horizontal (x) and vertical (y) coordinates by the standard center-of-gravity calculation are

$$x_{\mathrm{cg}} = \frac{\sum_{i=1}^{n} E_i x_i}{\sum_{i=1}^{n} E_i} \qquad y_{\mathrm{cg}} = \frac{\sum_{i=1}^{n} E_i y_i}{\sum_{i=1}^{n} E_i} \tag{4.1}$$

where E_i is the energy contained in tower i (out of n towers) and x_i and y_i are the coordinates of the center of this tower. For electron showers, the sum comprising the signals of the tower with the maximum energy deposit and the hexagonal ring around it, *i.e.*, $n = 7$, is sufficient for this calculation.

However, there is a bias depending on the position within the hexagon. The positions of 80 GeV electrons entering the calorimeter tilted at $\theta_z = 2°$ at various points on a tower are shown in fig. 4.14. It shows the impact point of each electron on a SPACAL tower as measured by a beam chamber and the position of the center of gravity of the shower as found using eq. 4.1. The positions measured by the calorimeter are incorrectly reconstructed. When an electron enters the center of a tower, ~5% of its energy is shared between the surrounding six towers. If the electron is displaced from the center by ~1 cm, the energy sharing between towers does not change much. The result is that the reconstructed positions are shifted toward the center or toward the axes linking this center with the centers of the neighboring towers.

In order to correct this position shift, it can be systematically described in another coordinate system (x', y') based on the position inside one of the six triangles that make up the hexagon, as shown in fig. 4.15 [57]. These coordinates describe the distance along an axis linking two cell centers (x') and the distance along a line perpendicular to this axis (y'). The new coordinates as measured by the calorimeter (CAL) are plotted against those measured by the beam chambers (BC) in fig. 4.16, showing a clear functional dependence. A fit describing the relation between $(x'_{\mathrm{CAL}}, y'_{\mathrm{CAL}})$ and the true position $(x'_{\mathrm{BC}}, y'_{\mathrm{BC}})$ was made, to be incorporated into a correction term. A

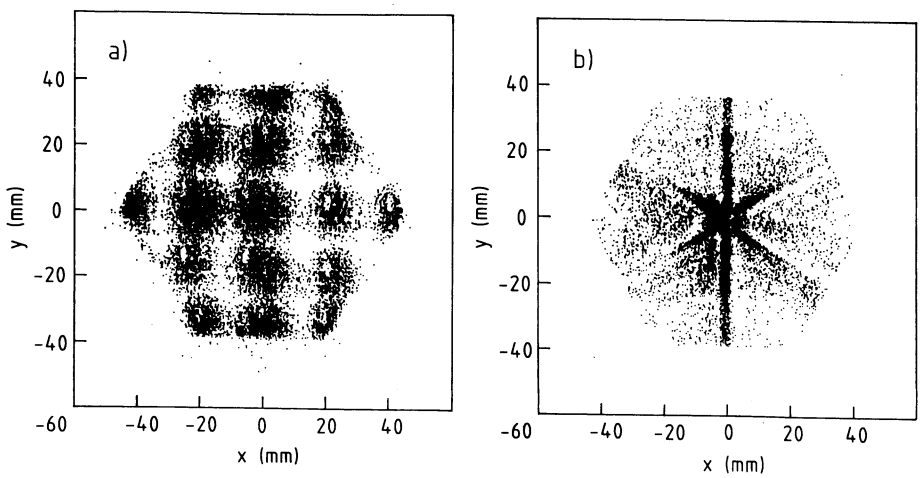

Figure 4.14: *The positions of the impact points of 80 GeV electrons on a SPACAL tower, determined (a) by the beam chambers and (b) by the center of gravity of the energy deposit in SPACAL [57].*

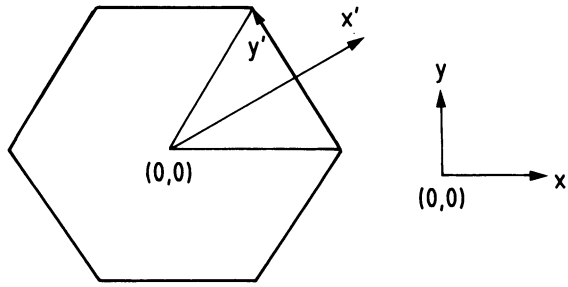

Figure 4.15: *The coordinate system used in the correction, based on the position in an hexagonal tower, to the center-of-gravity calculation of a particle showering in SPACAL [57].*

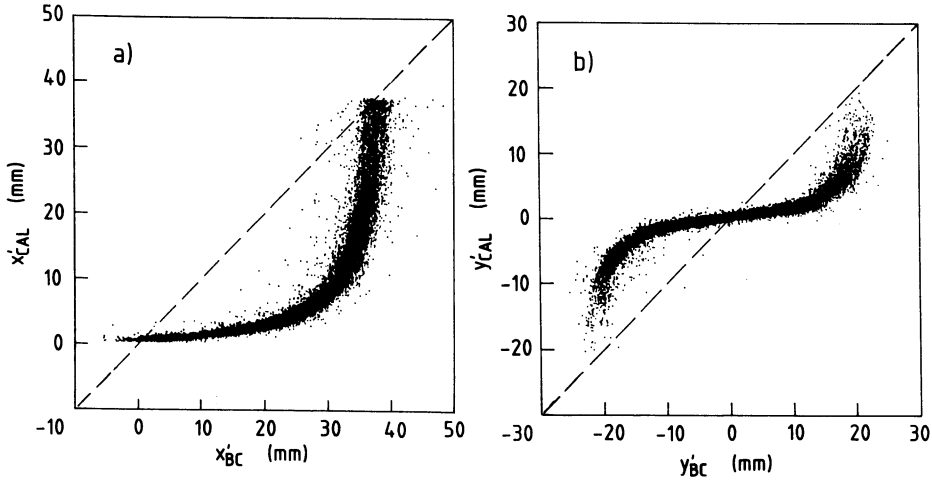

Figure 4.16: *Comparison of the position (x'_{CAL}, y'_{CAL}) determined by the center-of-gravity method in the calorimeter to the position (x'_{BC}, y'_{BC}) measured by the beam chamber, for 80 GeV electrons [57].*

good fit was found with the following expressions:

$$\begin{aligned} x'_{\mathrm{CAL}} &= 25.0 \arctan(0.363\, x'_{\mathrm{BC}}), \\ y'_{\mathrm{CAL}} &= 14.7 \arctan(0.476\, y'_{\mathrm{BC}}). \end{aligned} \tag{4.2}$$

Applying this as a correction to the simple center-of-gravity calculation results in a good correspondence between the impact point measured by the BC and the one measured by the calorimeter (fig. 4.17).

With the final determination of the position by the calorimeter, the position resolution σ_y for the vertical coordinate was found to scale with $E^{-1/2}$ [57], as shown in

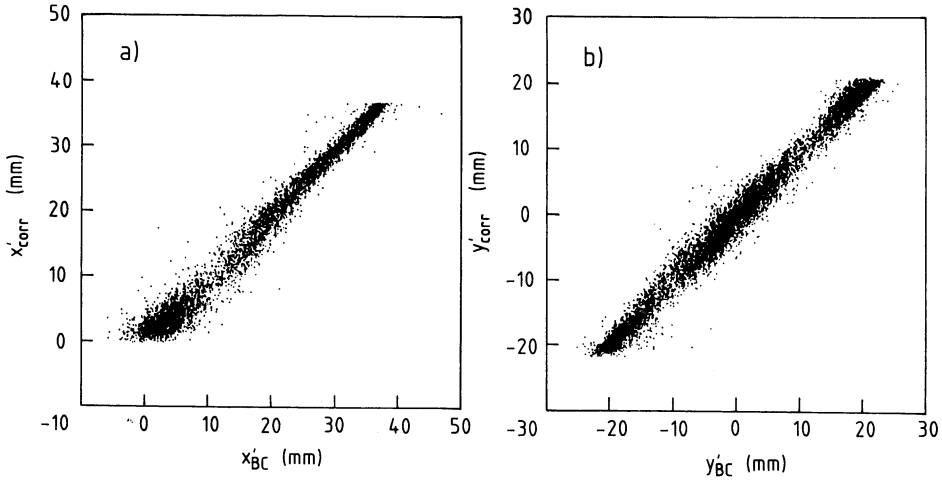

Figure 4.17: *Comparison of the corrected position (x'_{CAL}, y'_{CAL}) to the position (x'_{BC}, y'_{BC}) measured by the beam chamber, for 80 GeV electrons [57].*

fig. 4.18. The calorimeter was oriented at $\theta_z = 3°$, with the beam entering the center of the calorimeter tower. The data can be parametrized as

$$\sigma_y(E)\ [\text{mm}] = 17.1/\sqrt{E\ [\text{GeV}]}. \tag{4.3}$$

Such a relation is expected since the position determination is based on a measurement of the energy deposit in each cell, the resolution of which scales as $E^{-1/2}$. However, the uncertainty of the position is dependent on the relative position in a tower. It is greatest in the center of the tower where the energy sharing is least. The position resolution averaged over an entire tower was found to be $\sim 20\%$ better than that at the center, and the above result is therefore the worst case. Similar results were found for the horizontal coordinate. For 80 GeV electrons entering all over the surface of the calorimeter the position resolution is 1.8 mm in the x-direction and 1.6 mm in the y-direction.

4.3.4 Energy resolution

The energy resolution was found as a result of a Gaussian fit over the signal distribution, without restriction on the area around the peak value [58]. It is plotted for electrons in the calorimeter tilted at 3° as a function of energy in fig. 4.19. The data is best described by a fit of the form given in eq. 2.24, with the result

$$\frac{\sigma}{E} = \frac{(12.9 \pm 0.3)\%}{\sqrt{E}} + (1.23 \pm 0.05)\%, \tag{4.4}$$

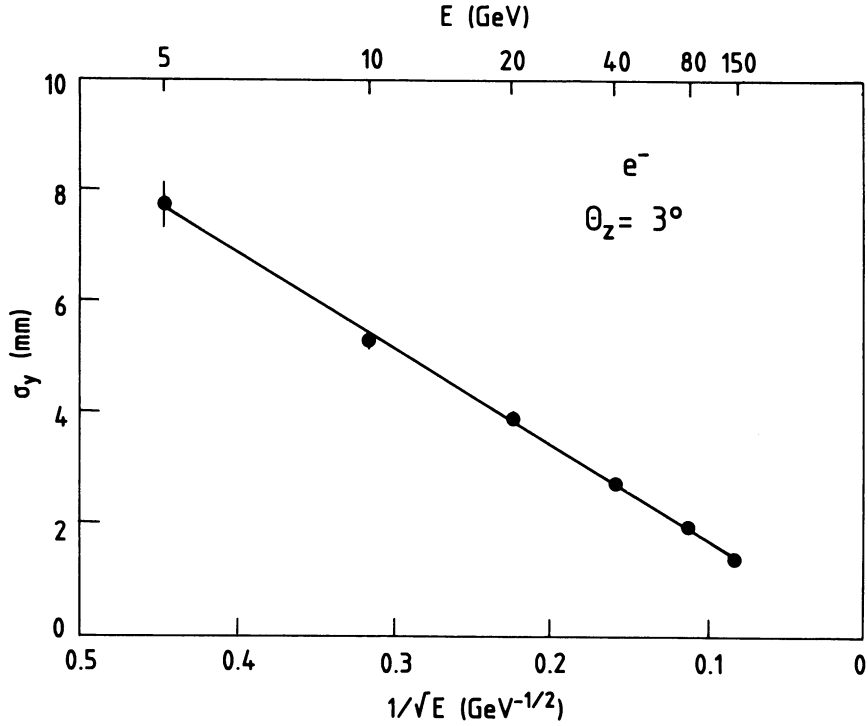

Figure 4.18: *The position resolution in the vertical direction as a function of energy, for electrons entering a tower center at $\theta_z = 3°$ [57].*

where E is given in GeV, with $\chi^2 = 0.9$ per degree of freedom (DOF). A fit to the quadratic expression (eq. 2.23) gives

$$\frac{\sigma}{E} = \frac{(15.7 \pm 0.2)\%}{\sqrt{E}} \oplus (1.99 \pm 0.05)\%, \tag{4.5}$$

with $\chi^2 = 4.8$/DOF. The origins of the scaling and constant terms were then investigated.

The $E^{-1/2}$ term is determined mainly by sampling fluctuations (sect. 2.3). The constant term is a result of systematic effects. These effects are, in general, magnified by the relatively small lateral shower dimensions and the small number of fibers (~40) involved in the shower. One source of fluctuations is the non-uniformity of the signal response due to fiber-to-fiber fluctuations (sect. 4.3.2), with consequences as discussed in sect. 3.2. In addition, the dependence of the sampling fraction on the impact point (fig. 4.13) increases the constant term (due to non-uniformity). This is seen in fig. 4.19, where the energy resolution for events impacting only on the lead (represented by the closed squares) is smaller than the resolution found for all events.

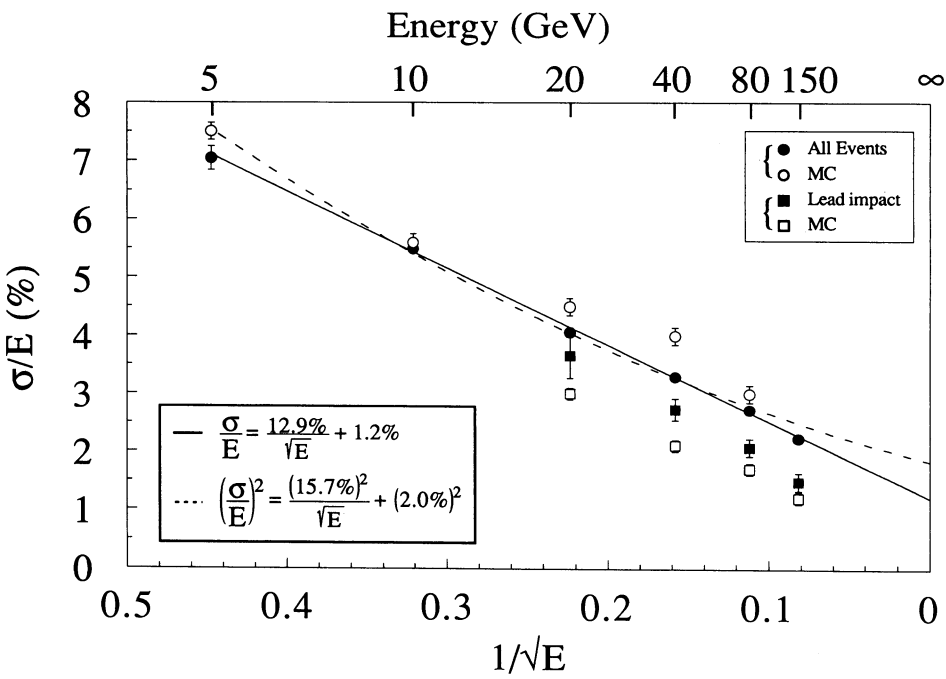

Figure 4.19: *The energy resolution for electrons as a function of energy, for $\theta_z = 3°$. The closed circles are the results of all the events, while the closed squares were determined with only particles entering in the lead. The open circles and squares show Monte Carlo results for these two cases. [58].*

Measurements with 80 GeV electrons entering the 20-tower detector at various angles (fig. 4.20) showed that the angular dependence of the energy resolution can be completely attributed to the term describing deviations from $1/\sqrt{E}$ scaling. This term almost vanishes completely at $\theta_z = 90°$ and grows rapidly at very small angles.

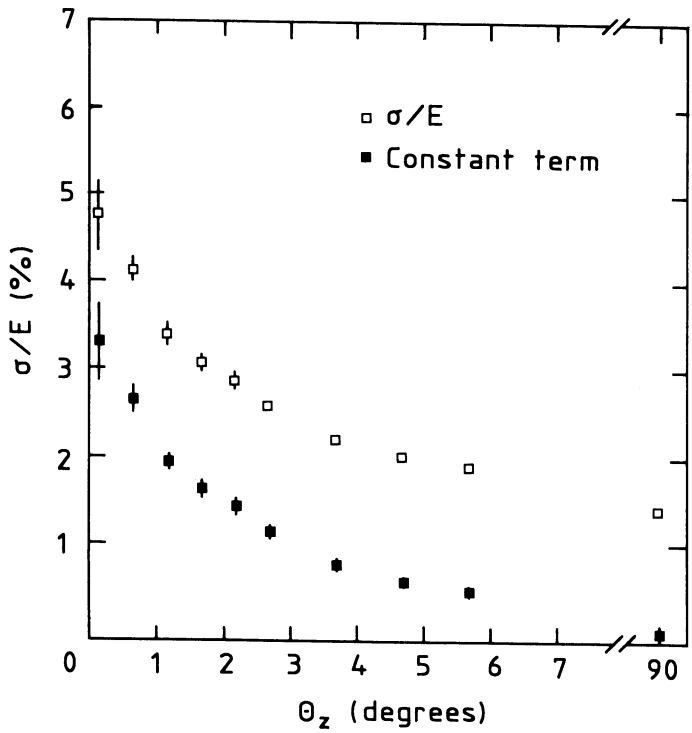

Figure 4.20: *The energy resolution (open squares) for 80 GeV electrons as a function of the angle between the fiber axis and particle direction. The closed squares show the constant term C_2 as a function of energy, resulting from a linear fit assuming $\sigma/E = 12.9\%/\sqrt{E} + C_2$. The measurement was made in the 20-tower calorimeter prototype [58].*

4.4 Pion detection

Hadronic showers in SPACAL are, in general, very broad, as shown by the energy deposit profile [61] for 80 GeV pions in fig. 4.21. The 155-tower calorimeter contains ~98% of an hadronic shower when the hadron enters the center [61]. Fig. 4.22 shows the containment of pion and electron showers as a function of the radius from the shower axis [57]. This measurement is important for determining the allowable cluster size for the hadron energy measurement. Leakage not only affects the correctness of measurement, but the precision as well, since the shower-to-shower fluctuations increase if the volume over which the shower signal is integrated is decreased. The lateral leakage as a function of energy is shown in fig. 4.23. It decreases with energy, since high energy showers are, in general, narrower [61]. There was a small amount of longitudinal leakage as well. This leakage energy was measured using the 20-tower calorimeter [59], and is shown as a fraction of the incident energy in fig. 4.24. It increases with energy, to nearly 0.5% at 150 GeV. In addition, the amount of leakage

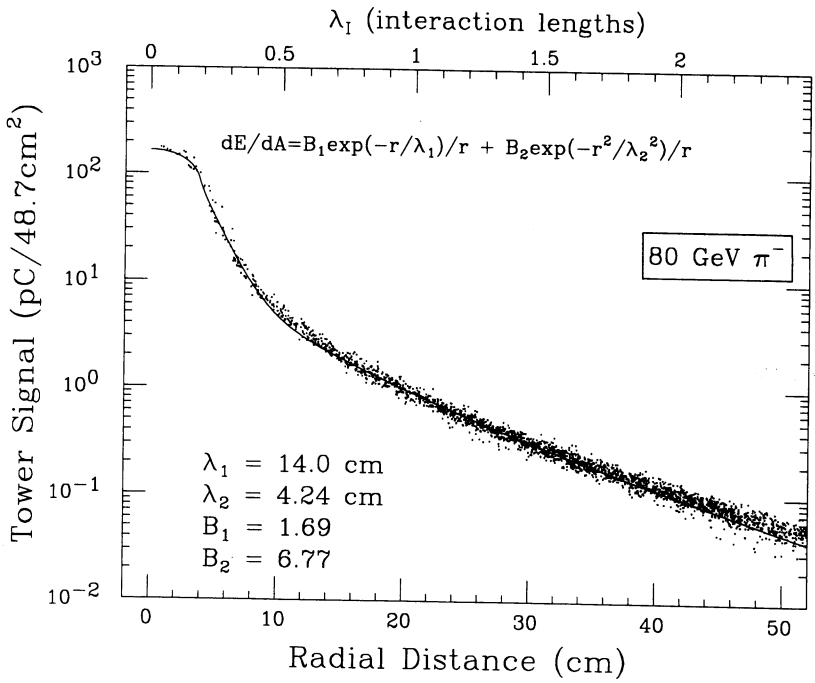

Figure 4.21: *Lateral shower profile for 80 GeV pions entering the calorimeter at $\theta_z = 2°$ at various positions. The tower signal is plotted as a function of the distance between the tower center and the shower axis. The curve is a fit to the data as indicated on the plot [61].*

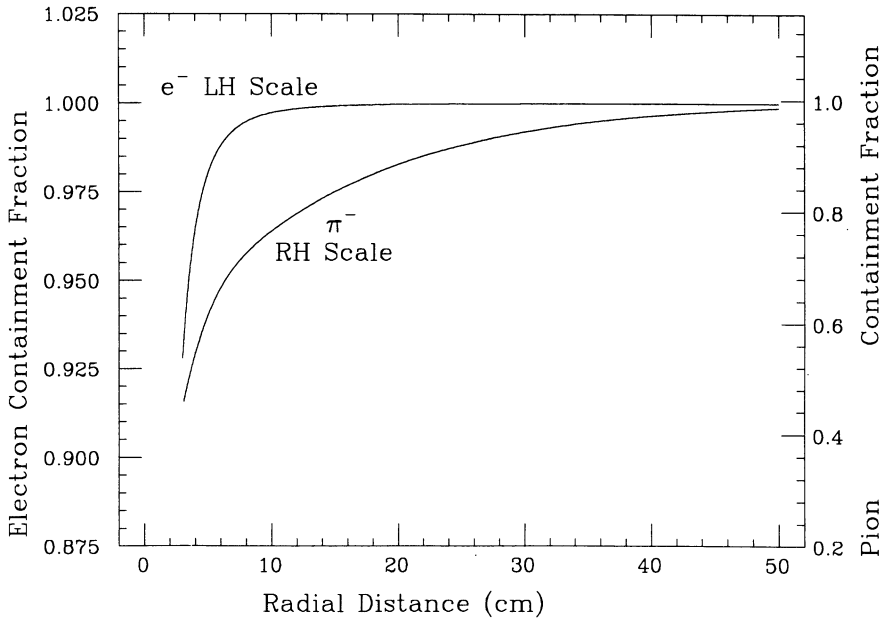

Figure 4.22: *Shower containment in SPACAL as a function of radius, for 80 GeV electrons and pions at $\theta_z = 2°$, as calculated by integrating over the fits to the lateral profiles. The left-hand scale is for the electrons; the right-hand scale is for the pions [61].*

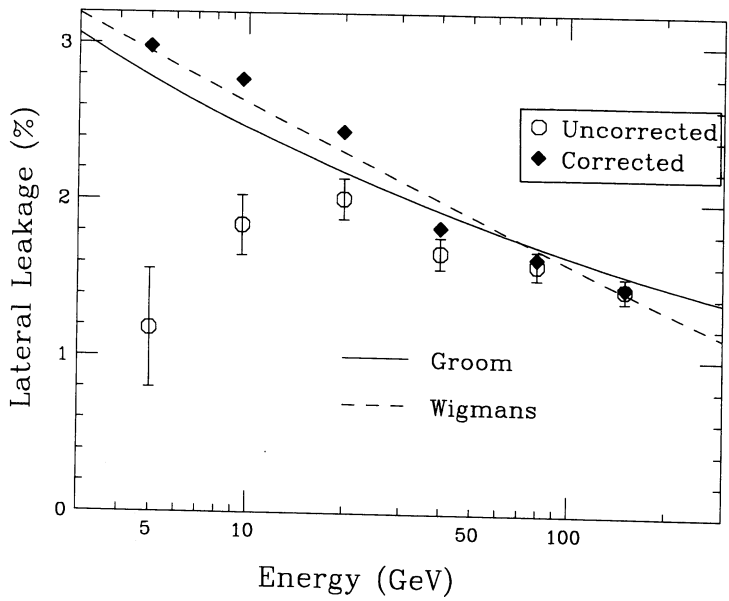

Figure 4.23: *The estimated lateral leakage of pion showers in SPACAL as a function of beam energy, for $\theta_z = 0°$. The open circles are the uncorrected data; the closed circles show the data corrected for low-energy cutoff by the ADCs. The curves are based on an estimation of the non-e.m. part of the showers [61].*

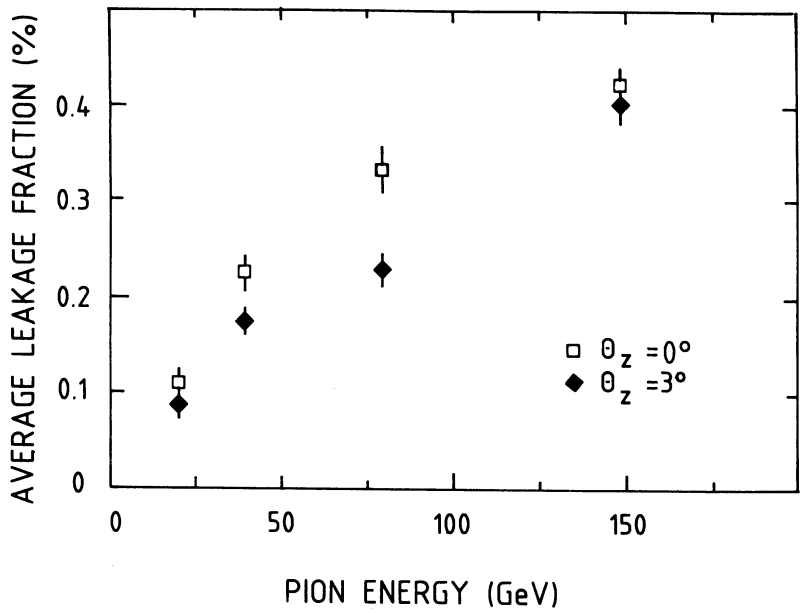

Figure 4.24: *The fraction of energy leakage out the back of the SPACAL, as a function of the beam energy. Data was taken at $\theta_z = 0°$ (squares) and at 3° (diamonds) [59].*

is slightly higher at $\theta_z = 0°$, due to the increased probability of pions channeling in a fiber before showering. Since polystyrene has a longer nuclear interaction length than the lead, a hadron can travel some distance in a fiber without showering. A shower that starts deeper in the calorimeter therefore has more rear leakage. This is the only effect at small angles seen for pions in SPACAL.

The large dimensions of the hadronic shower cause many fibers to contribute to the signal, and the fiber-to-fiber response variations are much less important than for e.m. showers. Therefore, the increase in energy resolution due to lateral non-uniformity, so important with e.m. showers, is absent for hadronic showers. Experimental measurements confirm this [58]. A scan with 80 GeV pions over an area of 24×24 cm^2 showed an RMS variation of the signal of only 1%.

4.4.1 Position measurement

The procedure to determine the position (x_{CAL}, y_{CAL}) of a hadronic shower barycenter is similar to that for e.m. showers (sect. 4.3.3). The center-of-gravity calculations were made using eq. 4.1, using the energy deposited in the 2 rings of towers surrounding the central tower ($n = 19$), which gives the best spatial resolution [57]. Data from 80 GeV pions entering the calorimeter at $\theta_z = 2°$ are shown in fig. 4.25, in the coordinate system (x', y') (fig. 4.15). Despite the fact that there is more energy sharing between

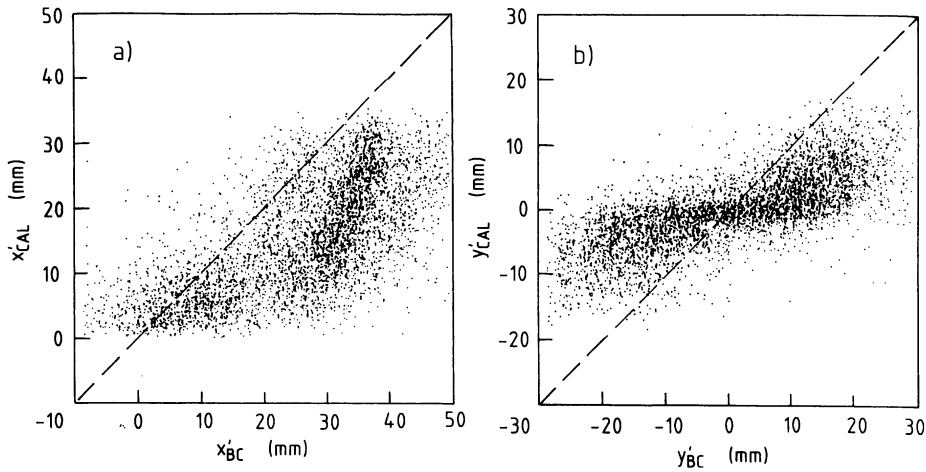

Figure 4.25: *Comparison of the shower position (x'_{CAL}, y'_{CAL}) determined by the center-of-gravity method in the calorimeter to the position (x'_{BC}, y'_{BC}) of the incoming particle measured by the beam chamber, for 80 GeV pions [57].*

towers for the broader pion showers (~50% of the energy in the center tower), there is a shift in position similar to that for electron showers, although it is more smeared. This is due to the e.m. core of the pion shower.

Expressions describing the average position shift were found [57]:

$$\begin{aligned} x'_{\mathrm{CAL}} &= 29.7 \arctan(0.084\, x'_{\mathrm{BC}}), \\ y'_{\mathrm{CAL}} &= 17.0 \arctan(0.147\, y'_{\mathrm{BC}}). \end{aligned} \tag{4.6}$$

These were used to correct the positions, resulting in a good agreement between the calorimeter and beam chamber measurements.

The major difference of the hadronic barycenter measurement as compared to the e.m. shower measurement occurs from the larger fluctuations in the energy deposit profile, increasing the uncertainty on the position measurement. Since the lateral energy deposit is used in this calculation, fluctuations in the lateral profile affect the position resolution. Longitudinal fluctuations may also contribute to the uncertainty. When the calorimeter is tilted at an angle θ_z, the depth of the shower barycenter shows up as a lateral displacement from the impact point, and therefore longitudinal shower fluctuations translate into lateral ones. In the beam tests, the calorimeter was tilted with respect to the vertical plane $(y-z)$, resulting in a systematic displacement of the final calorimeter barycenter position x_{CAL} from the impact point x_{BC} as measured by the beam chamber as a function of the depth d of the shower:

$$x_{\mathrm{CAL}} - x_{\mathrm{BC}} = d \tan\theta_z. \tag{4.7}$$

The average displacement at different angles is shown in fig. 4.26, with the expected results [57]. If the impact point is known, the depth of a shower can be found, thus providing information generally only found using longitudinally segmented calorimeters. It is used in the beam tests to correct the signals for for the effects of light attenuation with shower depth (sect. 4.4.2).

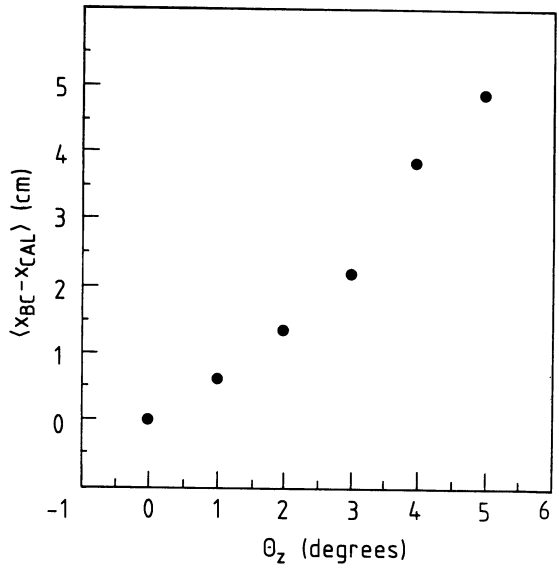

Figure 4.26: *The average displacement of the shower barycenter x_{CAL} from the impact point x_{BC} as a function of the angle θ_z between the fibers and the particle direction. Data for 40 GeV π^- entering the central region of a tower [57].*

The position resolution of pions in SPACAL is a function of energy, in the same way as the e.m. position resolution. The vertical position resolution, shown in fig. 4.27, can be parametrized as

$$\sigma_y(E)\ [\mathrm{mm}] = 2.4 + 31.4/\sqrt{E\ [GeV]}, \tag{4.8}$$

for pions entering at $\theta_z = 3°$ into the center of a tower [57]. As for e.m. showers, the tower center represents the worst possible case. Averaged over all positions in a tower, the resolution improves to $\sigma_y = 5.1$ mm at 80 GeV, over $\sigma_y = 5.8$ mm at the center of a tower. The horizontal position residual includes the fluctuations of the shower depth, resulting in a distribution which is described by the convolution of a Gaussian distribution with $\sigma_x = \sigma_y$ and an exponential distribution of the shower starting point. Such a fit was made and was consistent with the pion interaction length [57].

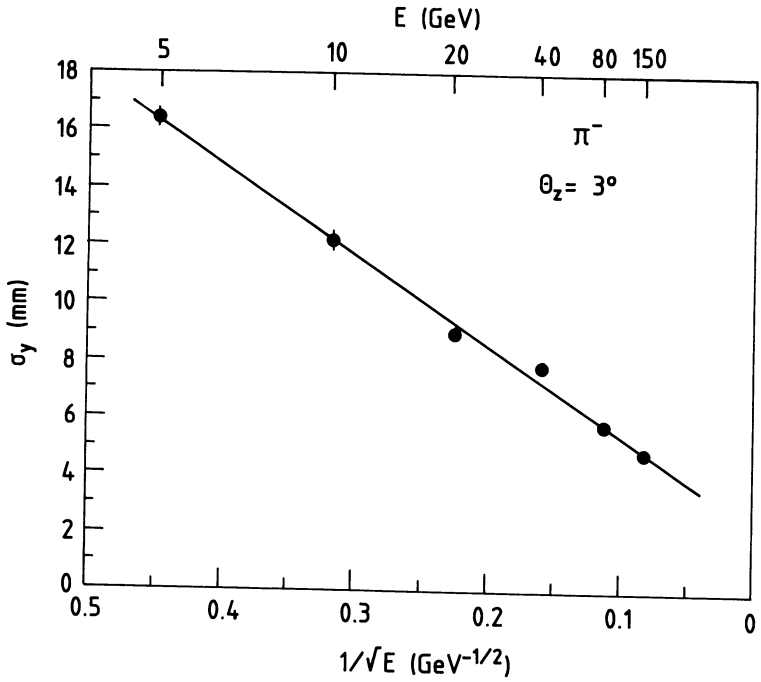

Figure 4.27: *The position resolution of the vertical coordinate as a function of energy, for pions entering the central region of a SPACAL tower at $\theta_z = 3°$ [57].*

4.4.2 Attenuation effects

The calorimeter signals are affected by the attenuation properties of the fibers. These properties are more pertinent to the measurement of hadronic showers, which penetrate deeper in the calorimeter and have a larger longitudinal spread than e.m. showers (sect. 2.3.2. Consequently, the signal varies greatly at a single energy: the deeper the light is produced, the less it is attenuated before reaching the PM. Signal distributions for 10, 40, and 150 GeV pions (entering the calorimeter at $\theta_z = 3°$), shown in the left-hand column of fig 4.28, illustrate the consequences of very deep showers in the form of a tail at the high-energy side of the distribution. This tail is more prominent at higher energy.

With knowledge of the depth of each shower barycenter and the attenuation characteristics of the calorimeter, it was possible to correct for this effect event by event [58]. The depth of the shower was found using eq. 4.7, when the calorimeter is tilted at angle θ_z and the impact point was known by non-calorimetric means (*e.g.*, the beam chamber). The greater signal at greater depth is clearly apparent in fig. 4.29, which shows the calorimeter signal for each shower as a function of the displacement between the shower barycenter and the impact point of the particle.

The attenuation curve for the 20-tower calorimeter was measured by aiming 40 GeV electrons into the detector perpendicular to the fiber axis ($\theta_z = 90°$) along its length [58]. The average calorimeter signal is plotted against the distance z between the impact point and the PMs in fig. 4.30. The points were fit by the expression

$$I(z)\ [\mathrm{pC}] = I_0 \left[e^{-z/\lambda_{\mathrm{att}}} + R e^{-(2L-z)/\lambda_{\mathrm{att}}} \right] + I_1 e^{-z/\lambda_{\mathrm{clad}}}, \tag{4.9}$$

where z is measured in meters. This accounts for the core attenuation ($\lambda_{\mathrm{att}} = 3.3$ m from sect. 3.3.2) with the aluminized front end of reflective index $R = 0.85$ (sect. 3.3.2) at $L = 2.2$ m from the PMs (eq. 3.7) and for the cladding attenuation (eq. 3.6) as parametrized by the attenuation length λ_{clad}. The fit determined the three remaining parameters to be

$$\begin{aligned} I_0 &= 168 \pm 0.1 \text{ pC}, \\ I_1 &= 79 \pm 0.6 \text{ pC}, \\ \lambda_{\mathrm{clad}} &= 0.60 \pm 0.01 \text{ m}, \end{aligned} \tag{4.10}$$

and is plotted with the data in fig. 4.30. Errors include only statistical uncertainty. The resulting λ_{clad} is consistent with the value measured with single fibers (sect. 3.3.1).

It turned out that there is a strong correlation between the different parameters of eq. 4.9. A slightly better fit of the experimental data was obtained with the following set of values:

$$\begin{aligned} \lambda_{\mathrm{att}} &= 11.0 \text{ m(fixed)}, \\ I_0 &= 102 \pm 0.2 \text{ pC}, \\ I_1 &= 124 \pm 0.5 \text{ pC}, \\ \lambda_{\mathrm{clad}} &= 0.77 \pm 0.01 \text{ m}. \end{aligned} \tag{4.11}$$

These parameter values were used to correct the measure signals for the effects of light attenuation in the fibers. The signal from each pion was then adjusted by weighting it

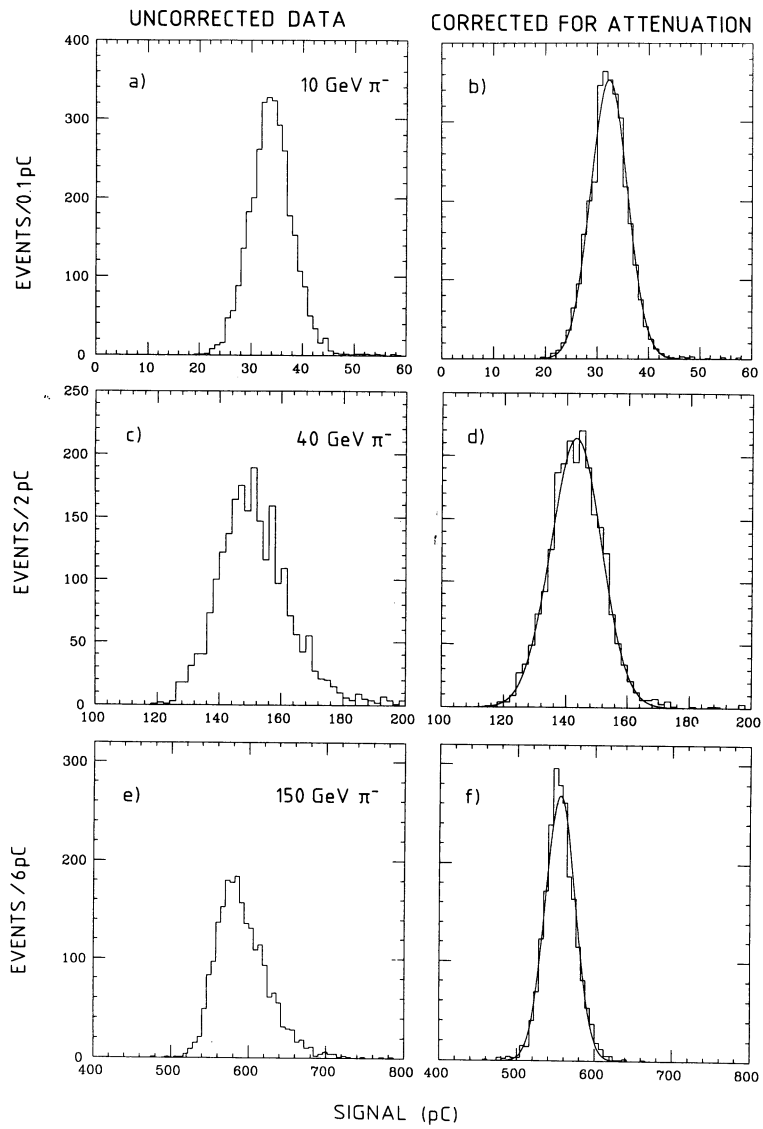

Figure 4.28: *The signal distributions for 10, 40, and 150 GeV π^- entering the SPACAL at an angle $\theta_z = 3°$. In the left-hand column (a, c, e) appear the measured distributions. The corresponding distributions after correcting for attenuation effects are in the right-hand column (b, d, f). The curves are the result of Gaussian fits [58].*

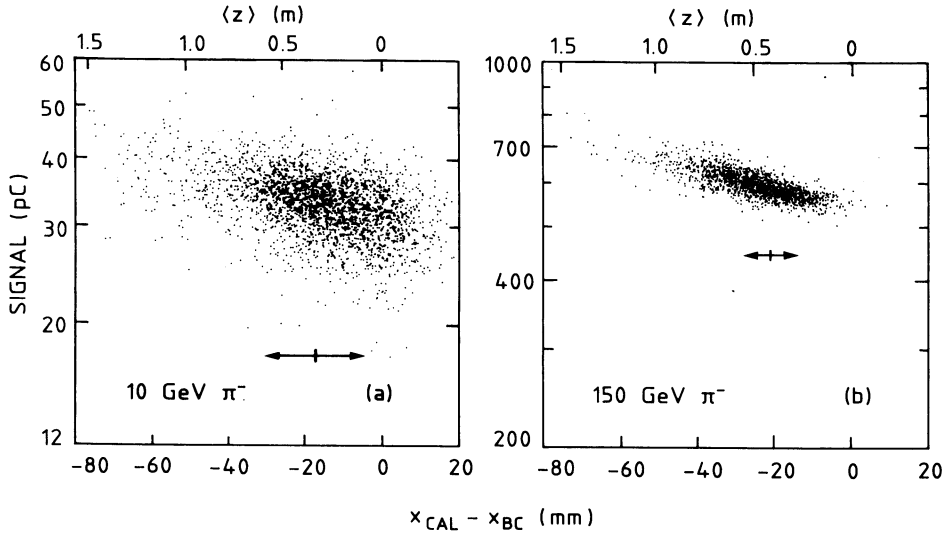

Figure 4.29: *The calorimeter signal versus the lateral displacement of the barycenter from the impact point (bottom axis), which is a measure of the depth of the shower (top axis), for (a) 10 GeV π^- and (b) 150 GeV π^-, entering the SPACAL at $\theta_z = 3°$. The arrows indicate the precision of the position measurements [58].*

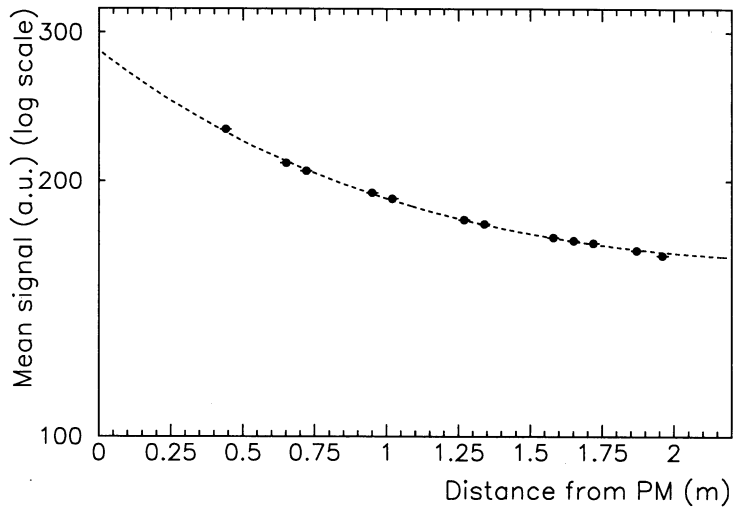

Figure 4.30: *The average signal for 40 GeV e^- entering the 20-tower calorimeter perpendicularly ($\theta_z = 90°$), as a function of the distance from the impact point to the PM. The curve is the fit to the attenuation expression given in eq. 4.9 [58].*

by a factor $I(2.2)/I(d)$. The scatter plots from fig. 4.29, which appear tilted as a result of light attenuation, flatten out as a result of this operation. The corrected signals are plotted on the right-hand side of fig 4.28 for the same data as on the left column. The signal distributions are well-described by a Gaussian distribution, as the fits on the plots show, and narrower (better resolution) than without the attenuation correction.

This correction is not possible using exclusively calorimetric information from SPACAL or if $\theta_z = 0°$. In an experiment, the impact point and angle of the charged particle on the calorimeter is usually measured by tracking detectors. This is not possible for neutral particles. In particular, this correction can not be used when detecting neutrons with SPACAL oriented at $\theta_z = 0°$ in WA89 (chap. 5). However, the longitudinal fluctuations causing the differences between the signal distributions in fig. 4.28 are smaller for neutrons than for pions, since the interaction length, which sets the scale for these fluctuations, is smaller for neutrons than for pions [12].

4.4.3 Energy resolution

The energy resolution, the width of a Gaussian fit on the signal distribution, of pions from 5 to 150 GeV entering SPACAL at $\theta_z = 3°$ is plotted in fig. 4.31, before and after the correction for the attenuation effects described in the previous section. The data is well-described by fits to both the linear and quadratic expressions for the energy resolution, as shown on the plots. The results of the least-squares fits before the attenuation correction are [58]:

$$\frac{\sigma}{E} = \frac{(27.7 \pm 0.6)\%}{\sqrt{E}} + (2.5 \pm 0.1)\%, \tag{4.12}$$

with $\chi^2 = 4.8/\text{DOF}$, and

$$\frac{\sigma}{E} = \frac{(33.9 \pm 0.4)\%}{\sqrt{E}} \oplus (4.1 \pm 0.1)\%, \tag{4.13}$$

with $\chi^2 = 3.4/\text{DOF}$.

After the attenuation correction, there is considerable improvement to the constant term. The fits to the data give:

$$\frac{\sigma}{E} = \frac{(30.6 \pm 0.5)\%}{\sqrt{E}} + (1.0 \pm 0.1)\%, \tag{4.14}$$

with $\chi^2 = 2.4/\text{DOF}$, and

$$\frac{\sigma}{E} = \frac{(33.3 \pm 0.4)\%}{\sqrt{E}} \oplus (2.2 \pm 0.1)\%, \tag{4.15}$$

with $\chi^2 = 2.0/\text{DOF}$.

The constant term of the energy resolution does not completely disappear after the attenuation effects are removed, initiating an investigation into this term. The small

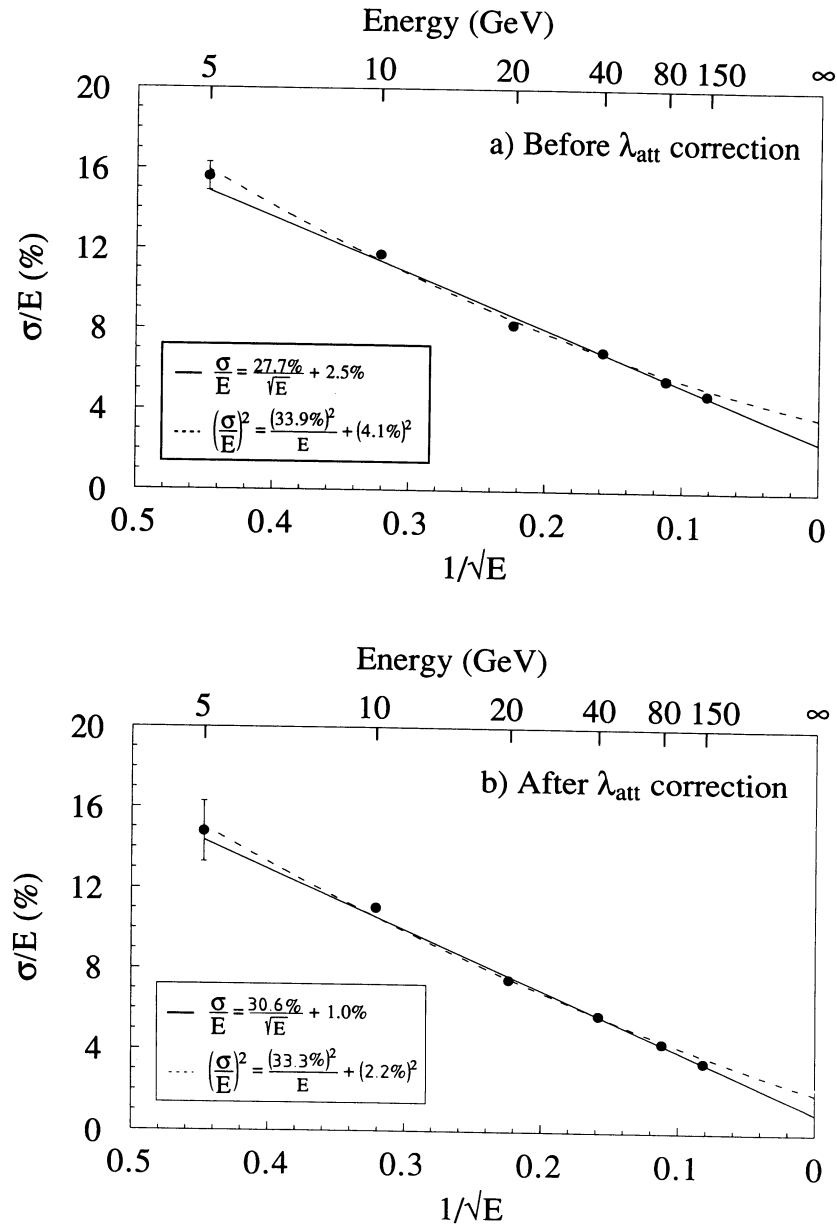

Figure 4.31: *The energy resolution for pions entering the calorimeter at $\theta_z = 3°$ as a function of the pion energy, (a) before and (b) after correcting for the effects of light attenuation. The curves are the results of least-squares fits to the data [58].*

angular dependence of the shower containment (fig. 4.24) did not significantly contribute to the constant term of the energy resolution. This term is caused primarily by the fact that the calorimeter is not completely compensating (sect. 2.4), as determined in the next section.

For all of the results presented, the pion signal consists of the sum of all 155 towers of SPACAL, which cover the same area as a circle with a radius of 49 cm. Under experimental conditions, however, it may be desirable to integrate over a smaller area to avoid overlapping showers or event pile-up or to provide fast information for a trigger decision. This would affect the precision of the energy measurement by introducing additional fluctuations in the shower containment. The energy resolution was therefore measured as a function of the cluster size [58], with results plotted in fig. 4.32*a*. Each point is the result of a different number of hexagonal rings being included, with the effective radius being that of a circle covering the same area. As expected, the energy resolution becomes worse as the cluster size gets smaller, but down to ~30 cm the resolution increases by less than 10%. The degradation of the resolution at smaller radii is more severe for higher energy. Fig. 4.32*b* presents the same data in terms of the lateral leakage at a certain radius. The fraction of lateral leakage for the same cluster size decreases with increasing energy, but the relative degradation

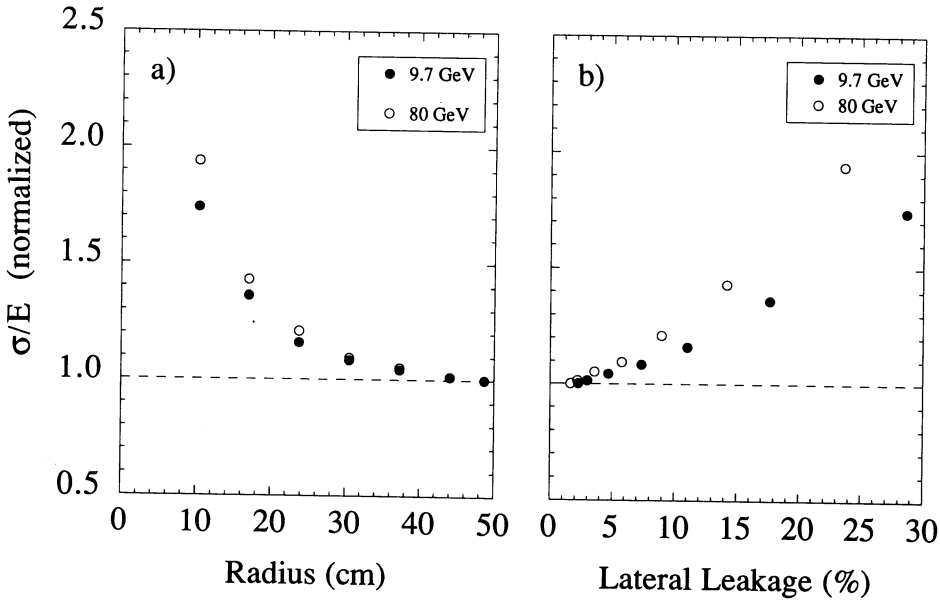

Figure 4.32: *The energy resolution, for 9.7 and 80 GeV pions at $\theta_z = 3°$, (a) as a function of the effective radius of the area over which the signal is integrated and (b) as a function of the fraction of lateral leakage. The resolution is normalized to the nominal one for the whole calorimeter [58].*

of the energy resolution is larger at higher energy. The effect of lateral leakage on the energy resolution can be described by the addition (in quadrature) to the scaling term of approximately $1/\sqrt[4]{E}$ term. The best empirical result was [58]

$$\frac{\sigma(E)}{E} = \frac{C_1}{\sqrt{E}} \oplus 0.90LE^{0.22} + C_2, \tag{4.16}$$

where C_1 and C_2 are the values found with full containment (eq. 4.12), L is the average fractional lateral leakage, and the energy E is given in units of GeV.

4.4.4 The e/π signal ratio and the determination of e/h

Since SPACAL was designed to be compensating, and hence to have an optimal hadronic resolution, the e/π signal ratio was measured in order to determine the degree of compensation, as given by e/h. The e/π ratio of the e.m. response to the total hadronic response is dependent on energy, whereas the e/h, with h as the response to the non-e.m. part of a hadronic shower, is an energy-independent, intrinsic property of the detector, as discussed in chap. 2. The e/π signal ratio measured for SPACAL [58] is shown in fig. 4.33. A systematic error of 1% was added (in quadrature) to the statistical errors to account for instabilities in the PM response, for uncertainties in the beam energy and for a non-Gaussian calorimeter response (the difference between the mean signal from a Gaussian fit and from the simple average).

The e/π signal ratio can be changed by integrating the signal over a smaller area, which may be desirable under experimental conditions, as discussed in the last section. In this way, the pion response decreases with smaller radii of the cluster, whereas the

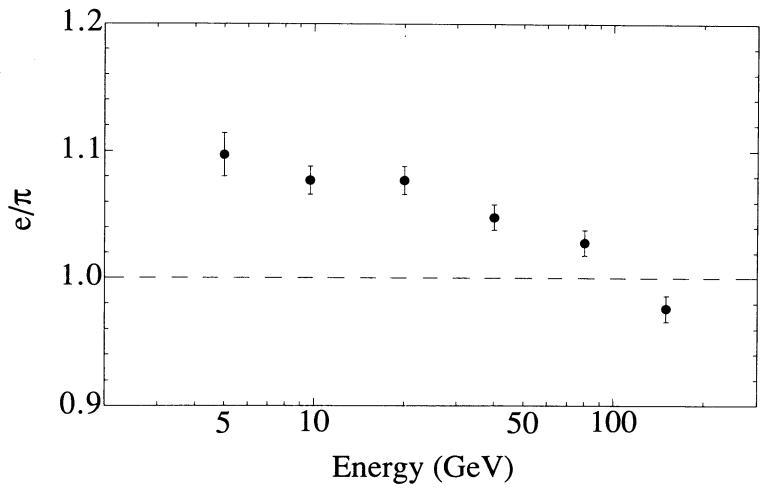

Figure 4.33: *The e/π signal ratio as a function of the particle energy, for $\theta_z = 3°$ [58].*

electron response remains the same down to the equivalent of about one hexagonal ring, within which the shower is fully contained. One expects then an increase in e/π with a decrease in radius, as confirmed by the measurement in fig. 4.34. In fact, the e/π ratio increases by only about 10% down to $\sim$ 30 cm [58].

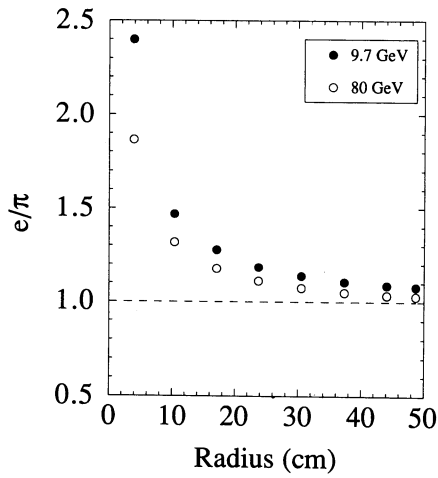

Figure 4.34: *The e/π signal ratio as a function of the effective radius of the area over which the signal is integrated. The ratio is normalized to the nominal one for the whole calorimeter. Results are for 9.7 and 80 GeV particles entering the calorimeter at $\theta_z = 3°$ [58].*

In order to determine e/h, which is the ratio of the calorimeter response from the e.m. and the non-e.m. parts of a hadronic shower, the instrumental effects on the calorimeter response had to be removed. This was done as follows.

i. As shown in the previous sections, pions that penetrate deeper in the calorimeter generate a higher signal from the less attenuated scintillation light. All signals were normalized as if their barycenter were located in the front of the calorimeter. This increases the value of e/π by 4-6%.

ii. When an electron started to shower in the PSD, it deposited a small fraction of its energy there. This was measured to be typically 0.2-0.3 GeV, which is a significant fraction of the total energy at the lower energies. This value was added to the electron response. Pions, assumed to behave like MIPs, lost only an average of 15 MeV in the PSD. Therefore, the overall correction increased e/π, in an energy-dependent way.

iii. The suppression of the small signals by the readout system means that small energy deposits were not included in the total signal. This especially affected

the hadron signal, with a spread in energy over many towers. In this way, the e/π was overestimated. A correction was determined by extrapolating from the effects of higher values of the cutoff [58]. After applying this correction, the e/π decreased accordingly.

iv. Energy leaking out of the calorimeter also led to an overestimation of e/π, since only hadronic showers are not fully contained. The measurement of the longitudinal leakage was shown in fig. 4.24. The lateral leakage was plotted in fig. 4.23, as determined from the shower profiles. The correction for both of these decreased e/π by 1-3%, depending on the energy.

v. After all of the above corrections were made, the electron response was found to be linear with energy, within the uncertainty of the beam energy ($\Delta E/E < 1\%$), except for the signal at 150 GeV. Saturation of the PM for the center tower, which contained ~95% of the total energy was suspected as the reason for the non-linear signal at 150 GeV. A correction was made to this response to force linearity, increasing the e/π ratio by 3.6%.

After all of these corrections for instrumental effects, the e/π ratio is plotted again with respect to energy in fig. 4.35. These points, excluding the one at 150 GeV for the reason just given, were fit to the expression relating e/π and e/h (eq. 2.13), where $\langle f_{\text{e.m.}} \rangle$ either follows a logarithmic energy dependence (Wigmans, eq. 2.14) or a power-law dependence (Groom, eq. 2.15). The resulting curves are shown on the plot. Combining the results of the two fits gives the value [58]

$$e/h = 1.15 \pm 0.02. \tag{4.17}$$

The same expressions also describe the non-linearity with energy of the pion response alone, when the electron response does not change with energy. The pion response is plotted as a function of energy in fig. 4.36 for the uncorrected and corrected data. After applying the described corrections for instrumental effects, the pion signal linearity is greatly improved. The small remaining signal non-linearity is in agreement with expectations on the basis of $e/h = 1.15$.

These results, which rely upon knowledge of the variation of $\langle f_{\text{e.m.}} \rangle$ with energy, were confirmed independently by measuring the $f_{\text{e.m.}}(E)$ [61]. The e.m. component of an hadronic shower consists of mostly π^0s produced in the early part of the shower. Therefore, one can measure the fraction f_{π^0} of the energy in this component by assuming that the especially large energy deposit at the "core" of the shower is due to π^0s (fig. 4.21). The lateral pion shower profile is well described by two terms, one describing the energy deposit over the whole shower, and one that is only prominent toward the center, the "core term." Using the parameters found by the fit, f_{π^0} was calculated for different energies and plotted in fig. 4.37. This data is is in reasonable agreement with the expressions used for $\langle f_{\text{e.m.}} \rangle$, represented by the curves on the same plot.

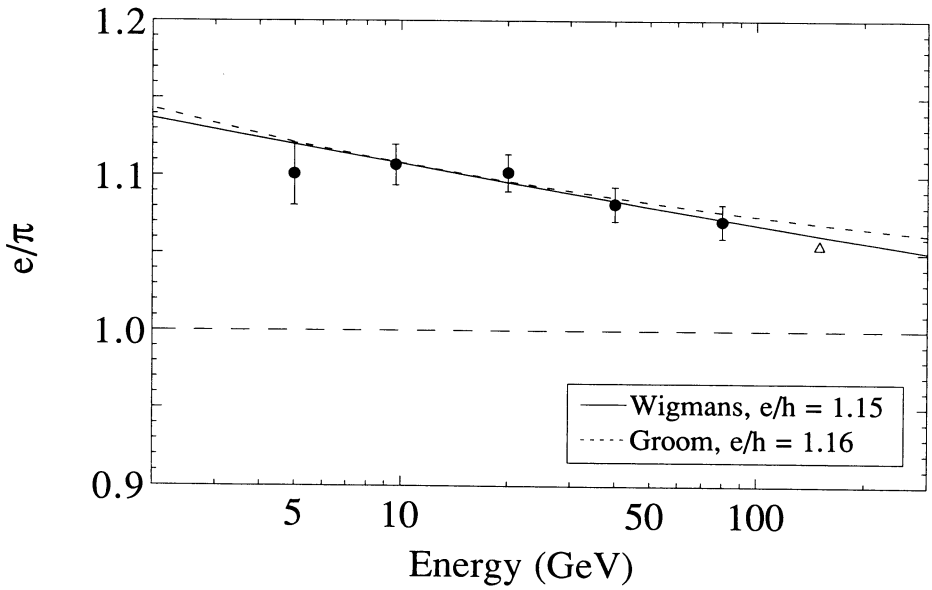

Figure 4.35: *The e/π signal ratio corrected for instrumental effects as a function of the particle energy, for $\theta_z = 3°$. The curves correspond to fits over all the points except the one at 150 GeV, resulting in $e/h = 1.15$ and 1.16 [58].*

The SPACAL detector, with $e/h = 1.15$, is therefore slightly undercompensating, resulting in an undesirable constant term in the hadron energy resolution and a non-linear hadron signal. The 1% constant term (to be added linearly to the scaling term) was predicted by Wigmans for a calorimeter with $e/\pi = 1.1$ at 10 GeV [11], and confirmed by SPACAL. This value differs from the the $e/h = 1.05 \pm 0.4$ found by the ZEUS Calorimeter group, who built a compensating calorimeter with the same volume ratio of lead and plastic scintillator [32], as reported in sect. 2.4.3. The increase in e/h in SPACAL is a result of higher sampling by the e.m. shower component. It was found that this happens when the distance between subsequent sampling layers are closer than $1X_0$ [11]. Evidence to support this comes from the comparison of the e/mip values for the different calorimeters. By comparing the electron response to the muon response in SPACAL, after correcting the latter for deviations from MIP behavior, the ratio e/mip of the electron response to the MIP response was found to be 0.72 ± 0.03 [62]. The measurement for the lead/scintillating-plate calorimeter (with a distance between active layers of 10 mm) gave $e/mip = 0.67 \pm 0.03$ [32]. This confirms that e.m. showers are more efficiently sampled (by ~7%) in SPACAL than in the ZEUS lead calorimeter, contributing to a higher e/h. Also, in SPACAL, 11% of the plastic volume is is taken up by the fiber cladding, in which energy deposited by a neutron often goes undetected, and therefore the sampling efficiency for neutrons is somewhat reduced. This also causes an increase in e/h. Therefore, in order to build

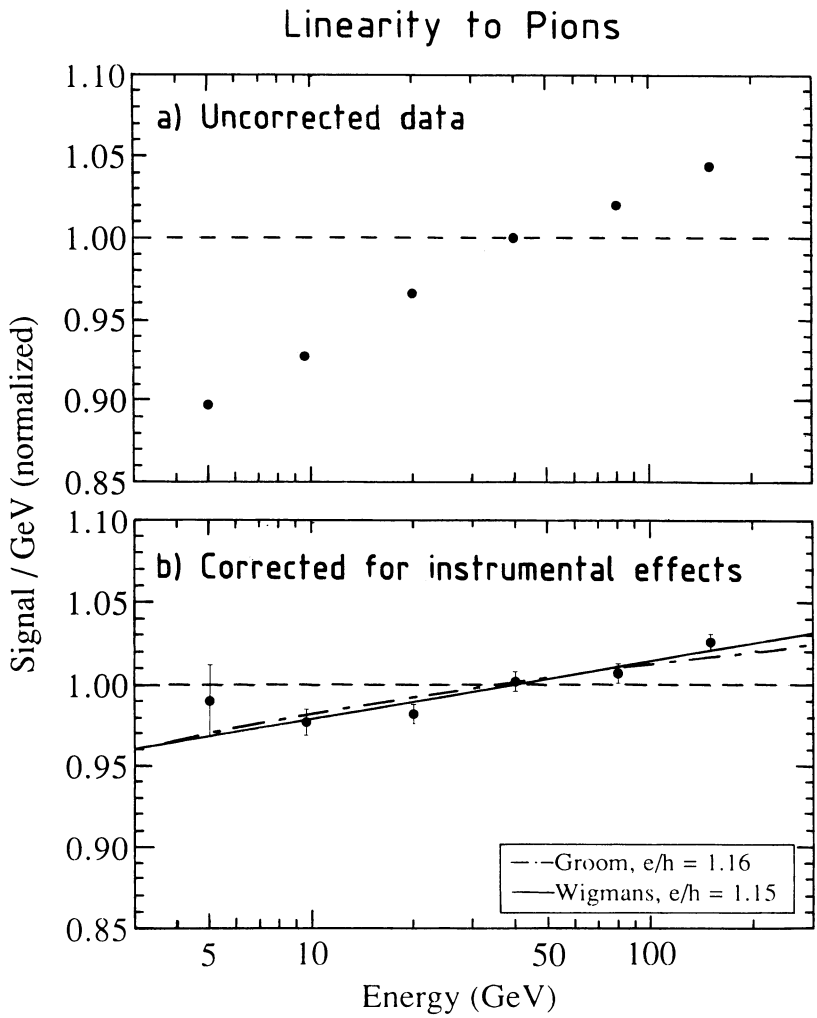

Figure 4.36: *The pion calorimeter signal normalized by dividing by the beam energy as a function of the energy for (a) before and (b) after corrections for instrumental effects. The curves correspond to fits for $e/h = 1.15$ and 1.16 [58].*

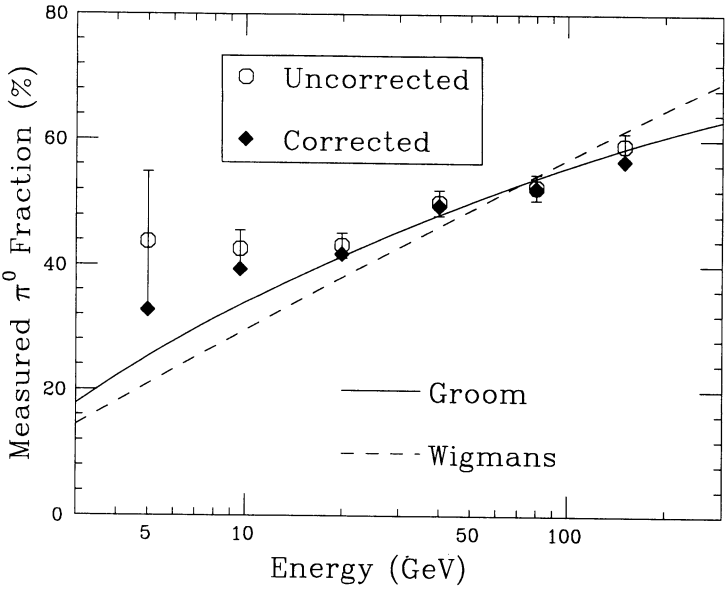

Figure 4.37: *The estimated π^0 fraction in pion showers as a function of energy. The open circles are for uncorrected data, the closed circles for data corrected for the low-energy cutoff by the ADCs. The curves correspond to the expressions for $e/h = 1.15$ and 1.16 [61].*

a compensating fiber calorimeter, either the fraction of the plastic taken up by the cladding should be reduced (with thinner cladding, for example) or the volume ratio of lead to plastic should be increased. However, the undercompensation of SPACAL is small, and the detector exhibits most of the advantages of compensation, in particular, an excellent hadronic energy resolution.

4.5 Electron–pion discrimination

The SPACAL design does not include longitudinal segmentation, and therefore has to exploit other techniques for electron–pion separation other than those based on differences in the longitudinal shower development that are used in many calorimeters. One exception is described in sect. 4.4.1, where, at a non-zero angle θ_z, the displacement of the shower barycenter from the impact point gives the depth of the shower [57]. At $\theta_z = 0°$, this is not possible and cannot be used for WA89. However, one can use the lateral shower characteristics to discriminate between electrons and pions, with the good granularity provided by SPACAL. In addition, the analog signals have a different time structure depending on whether they are caused by an electron or a pion shower. Methods of e–π separation by exploiting these characteristics are described

below. Longitudinal shower separation was achieved by the addition of a pre-shower detector made of a thin converter. This was described in sect. 4.2, and was used to clean the data samples (sect. 4.2.3). The results from other methods below used data taken with the 20-tower calorimeter, unless otherwise stated.

4.5.1 e–π separation by lateral shower characteristics

The differences in the lateral dimensions of e.m. and hadronic showers were discussed in sections 4.3 and 4.4. Just the fact that the hadronic shower is broader can be used to separate electron showers from pion showers. From fig. 4.22, one sees that for the same effective cluster radius less than 30 cm, the fractional shower containment of electrons and of pions are significantly different. A measure of this fraction for a given event provides a straightforward separation between the particles. This fraction can be characterized by a quantity called the containment $\mathcal{C}$ defined as [56]

$$\mathcal{C} = \frac{\sum_{i\in\{3\}} E_i}{\sum_{i\in\{12\}} E_i}. \tag{4.18}$$

The cluster $\{3\}$ consists of the three neighboring towers containing the highest energy deposit of any cluster. The cluster $\{12\}$ includes these three towers plus the towers immediately surrounding them. In this way, no knowledge of the particle's impact point is needed. The containment of 80 GeV electrons and pion entering the center of a calorimeter tower is plotted in fig. 4.38. The electron distribution extends only above 0.96 with almost full shower containment, while the pion distribution is very broad. A cut $\mathcal{C} \geq 0.970$ retains an electron efficiency of 98%, while passing 0.65% of the pion sample. With an impact point near the joining point of the three towers, better separation is achieved in general using the same cut.

Another method uses a quantity $R_{\rm p}$, which gives the effective width of the shower in the 155-tower calorimeter [57]. This quantity is defined as:

$$R_{\rm p} = \frac{\sum_{i=1}^{n} r_i E_i^{0.4}}{\sum_{i=1}^{n} E_i^{0.4}}, \tag{4.19}$$

where E_i is the energy contained in tower i (out of n towers) and r_i is the distance between the center of tower i and the (uncorrected) center of gravity of the shower (eq. 4.1). The distributions of $R_{\rm p}$ for electron and pion showers are well-separated, as shown in fig. 4.39. On the order of a fraction 10^{-3} of the pions pass the electron cut. These are probably the pions which have similar shower dimensions to electrons. Combining this with an additional cut based on the depth of the shower, as determined using eq. 4.7 where $\theta_z = 2°$, achieves separation down to 1.5×10^{-4} at 80 GeV, for 98% electron efficiency. This is only possible, however, when $\theta_z \neq 0°$.

4.5.2 e–π separation by signal time structure

Shower development over time in the calorimeter is encoded in the analog signal pulse. Data taken with a fast digital oscilloscope reveal significant differences in the time

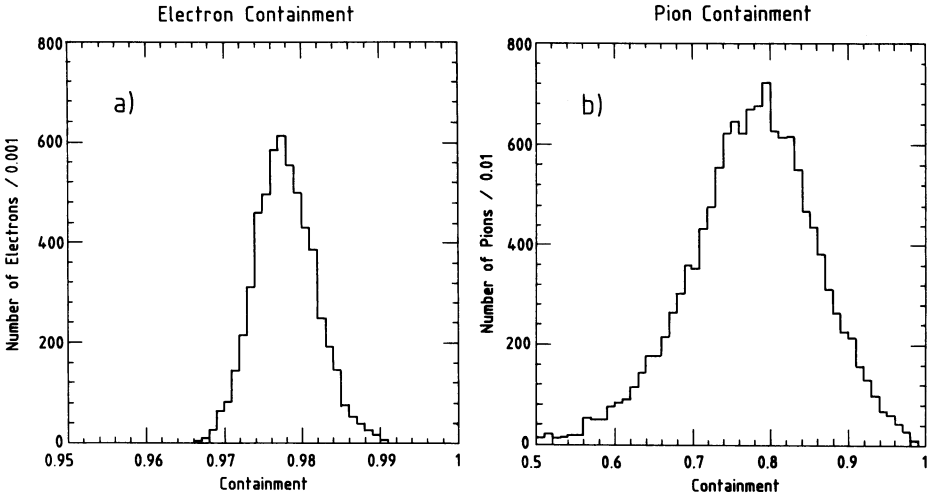

Figure 4.38: *The distributions of the containment fraction C for 80 GeV (a) electrons and (b) pions entering a calorimeter tower near its center. Note the different horizontal scales [56].*

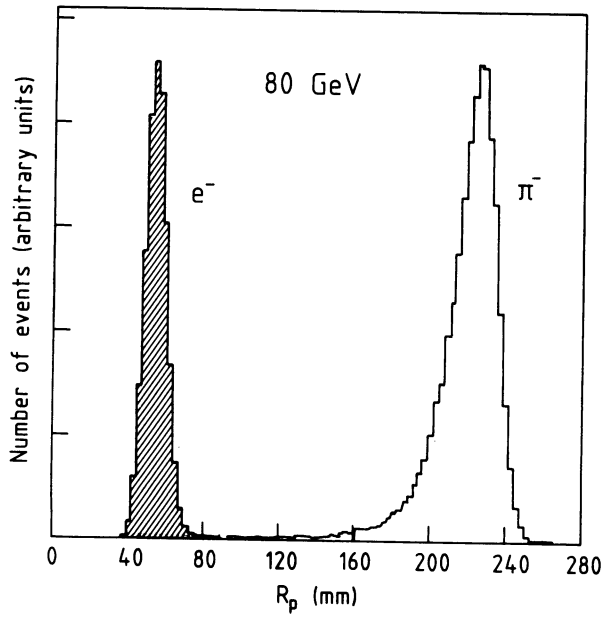

Figure 4.39: *Distribution of the effective width R_p of electron and pion showers at 80 GeV, with $\theta_z = 3°$ [57].*

structure of pulses from electron showers and from pion showers [55, 56]. Examples are shown in fig. 4.40. Whereas the electron signals are very similar at a single energy, the pions signals vary greatly. Some pion showers are made up of mostly π^0s which interact through e.m. processes, resulting in fast signals similar to the electron signals. Other pions may begin to shower deep in the calorimeter, so that the signal produced from the reflection off the aluminized ends of the fibers is well-separated from the direct signal. This causes a longer signal, with a second bump. The pion signals also exhibit a longer tail due to the neutron component in the hadronic showers. In addition to a difference in pulse length, the starting point of the pion pulses may vary by a few ns. Generally, the pion signals start earlier than the electron pulses.

One method to exploit these differences and provide good energy-independent discrimination between electrons and pions is to measure the time width of the pulse at

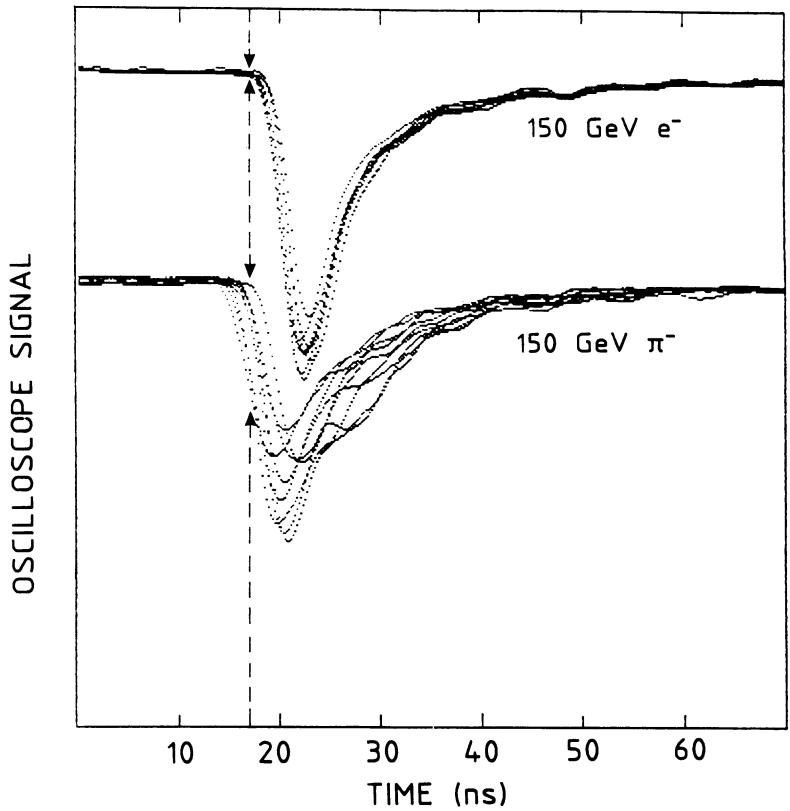

Figure 4.40: *Calorimeter analog signals, digitized and recorded by an oscilloscope. The signals from ten 150 GeV e^- showers overlap at the top, and those from ten 150 GeV π^- shower are overlaid on the bottom [55].*

a constant fraction of the amplitude, making it energy-independent. Good results [56] were obtained from the width at a fifth of the signal amplitude, where the signal was defined as the sum of the analog signals from the seven towers around the shower center. The full width at a fifth maximum (FWFM) was measured by a special circuit called a LATE-CFD (Leading and Trailing Edge Constant Fraction Discriminator). It provided the signal width in less than 100 ns after the arrival of the analog input signal at the input of the summing circuit. The FWFM is plotted for 80 GeV electrons and pions in fig. 4.41, showing almost complete separation between the distributions. The results of various electron selection cuts are plotted in fig. 4.42, where separation down to 1.25×10^{-3} is achieved with an electron efficiency of better than 99%. This technique was chosen for use with the SPACAL in the experiment WA89.

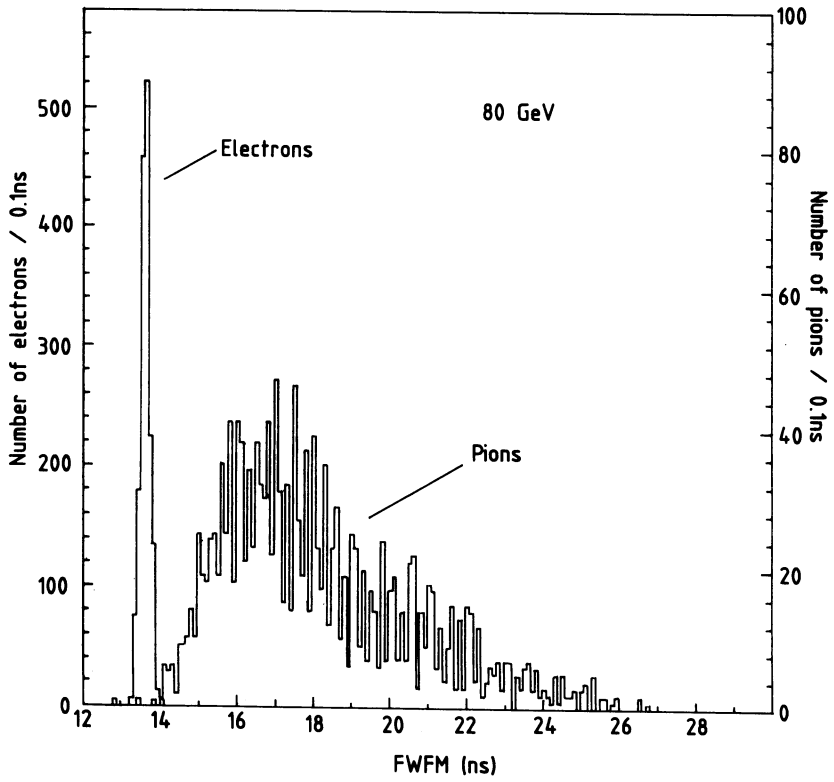

Figure 4.41: *Distribution of the full width at a fifth maximum (FWFM) of the calorimeter analog signals from 80 GeV electrons and pions [56].*

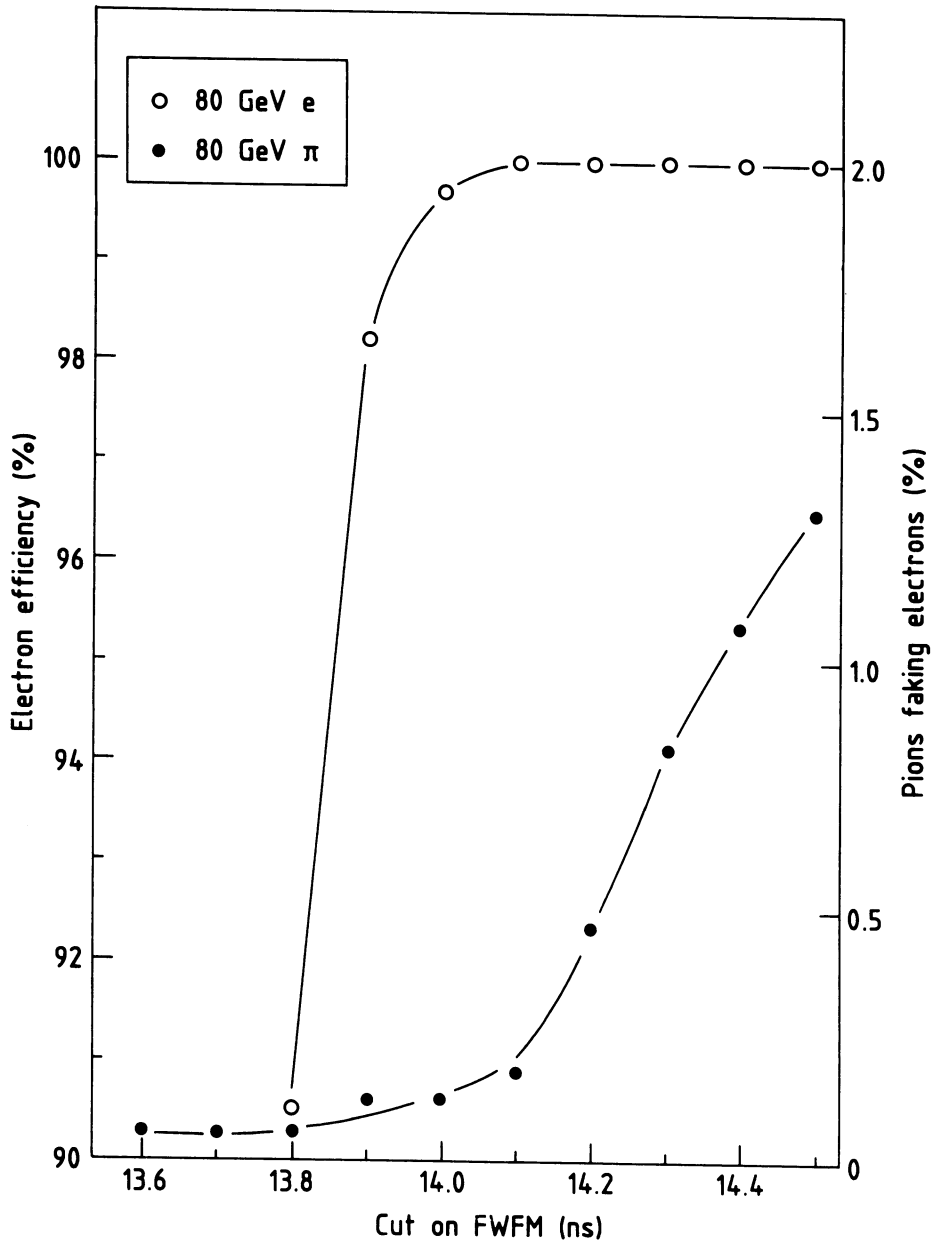

Figure 4.42: *The fraction of electrons (left-hand scale) and pions (right-hand scale) passing the cut on the FWFM as indicated on the horizontal axis, for the same data as in fig. 4.41 [56].*

Chapter 5

The Feast: A spaghetti calorimeter in WA89

A calorimeter can measure the energy of a particle, regardless of whether it is charged or uncharged. A typical high-energy physics experiment includes a magnet and a set of tracking detectors, using the curve of a charged particle's path to calculate its momentum and charge. For a neutral particle, another method must be used, namely the measurement of its energy deposit in a calorimeter. In the hyperon beam experiment WA89, an e.m. calorimeter had already served to measure the energy and position of neutral particles that shower electromagnetically, particularly π^0s. The 155-tower spaghetti calorimeter, discussed in chapter 4, was proposed for the identification and measurement of neutrons. Using the SPACAL detector in WA89 is also interesting for hadronic calorimetry. This is the first hadronic fiber calorimeter to be used in an experiment, a harsh environment compared to a test beam.

In this chapter, the performance of the spaghetti calorimeter in WA89 is described. First, the hyperon beam experiment and the motivations for the inclusion of SPACAL are presented. The modifications of the calorimeter for use in the hyperon beam are then described, followed by a detailed description of the calibration of the calorimeter with an electron test beam and with protons in the experiment. Finally, an application of the calorimeter in the experiment with the reconstruction of the decay $\Sigma^- \rightarrow n\pi^-$ is presented.

5.1 The Hyperon Beam Experiment WA89

The hyperon beam experiment WA89 at CERN has completed two physics runs, in 1991 and in 1993. The descriptions and results presented here are for the 1991 run only, in addition to calibration beam tests in the same period.

5.1.1 Experimental aims

The Hyperon Beam Experiment WA89 proposed to investigate three topics with a high-energy Σ^- beam impinging on a nuclear target [63]:

Charmed baryons

The hyperon beam experiment aims to investigate all the baryons containing one charm quark with $J = 1/2$. (Some of these are more well-known than others [64].) This corresponds to the $C = 1$ layer of the $SU(4)$ $J = 1/2$ baryon multiplet, as shown in fig. 5.1. Detection of all these baryons in one experiment allows comparison of their properties

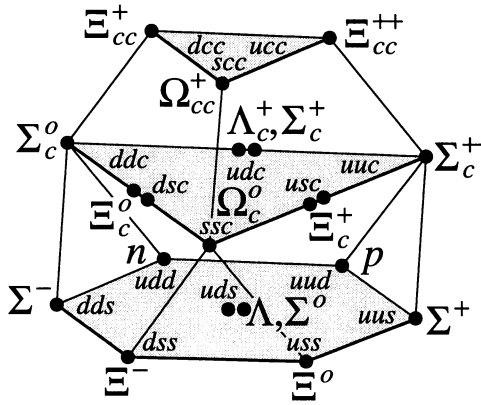

Figure 5.1: *The $SU(4)$ multiplet for baryons with $J = 1/2$.*

while minimizing systematic uncertainties. Those containing a strange quark are more easily produced than the others due to the presence of the strange quark in the incident Σ^-beam particles. Values for the masses have been calculated by several theoretical models [65], which attempt to explain the mass splittings for baryons containing heavy quarks. The measurement of the masses of charmed baryons is therefore a sensitive test for the validity of these models. In addition, their relative lifetimes have been predicted, based on the mechanisms involved in their decay modes [65]. Observation of the decay modes and the measurement of their branching ratios provide an insight into the dynamics of weak hadronic decays. Complementary to these measurements, the production properties of charmed strange baryons can also be studied, in particular the dependence of the production cross sections on the momentum components of the produced particles and on the mass number A of the target material [66].

Multi-quark states

The U(3100), with proposed quark composition $(qq) \cdot (\bar{q}\bar{q})$, has been predicted, with experimental evidence to support, but not verify, its existence [67]. WA89 should be

sensitive to the U with the good p/K separation of its decay products provided by the RICH detector (sect. 5.1.3). The experiment should have enough events to be able to verify the U. The search for the predicted dibaryon state H (quark content uuddss) is conducted by searching for its possible decay products, which include hyperons. Presently, the $\Lambda\Lambda$ and Ξ^-p channels are being investigated by WA89.

Rare hyperon resonances and decays

WA89 is studying the properties of rare hyperon resonances, in particular the Ξ and Ω.

5.1.2 The hyperon beam

In order to achieve the aims outlined above, charmed baryons must be produced in sufficient quantities for a reliable measurement of their properties. It has been found that baryon beams produce baryons with a higher x_F spectrum than meson beams [68], where x_F is defined as the fraction of the momentum p_L in the direction of the beam, $x_F = p_L/p_{L,max}$. In addition, lower particle multiplicities with a baryon beam result in a lower combinatorial background. In order to enhance the forward production of baryons containing a strange quark as well as a charm quark, a beam of strange baryons (hyperons) is used.

The hyperon beam at CERN was designed to fit in the available space of the H1 beam line in the West Hall [69]. In addition, the distance between the hyperon production and the experiment had to be kept short, due to the relatively short decay lengths of these particles. The average path length of the beam particles increases with energy, motivating the production of a high-energy beam.

The hyperon beam is a secondary beam, which is produced from a primary proton beam and defined by a magnetic channel, as shown in fig. 5.2. A beam of 450 GeV protons from the CERN SPS is aimed onto the beryllium production target. The three 2.4 T magnets have brass and tungsten collimators with small transverse dimensions which define the passage of the beam. In the first magnet, the primary protons remaining after the target are bent away from the reaction products and dumped into the magnet. The secondary reaction products are selected according to momentum by the channel in the second magnet. The exit of the third magnet, which is located 13 m from the production target, bends the beam back onto the axis of the incident proton beam.

The resulting beam contains all negative particles that were produced within the acceptance of the magnetic channel. These are mainly π^- and Σ^- in a production ratio of 2.5:1, with very small amounts of K^-, Ξ^-, $\bar{p}$, and Ω^- particles. Photon background is reduced by the presence of "pockets" in the downstream part of the channel which diminish the number of interactions in the walls and trap part of the showers in the tungsten. Muon background, from the decays of secondary pions and kaons created in the production target, is minimized by having a short distance (2.5 m) between the production target and the beam dump. Muons resulting from proton showers in

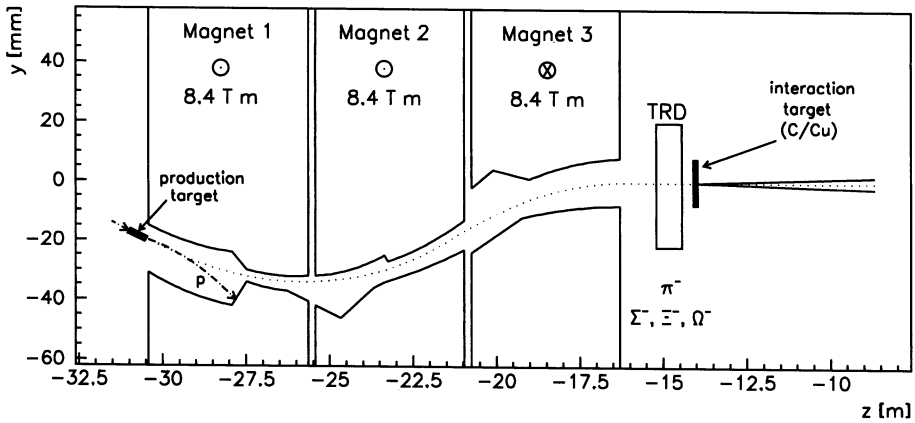

Figure 5.2: *The production of the hyperon beam. See text for details. Note the different scales in the horizontal and vertical directions.*

the dump region are minimized by the high density and short interaction length of tungsten.

In the 1991 running period, the average momentum of the beam was 330 GeV/c, with a spread $\Delta p/p$ of ~12%. About 7×10^5 beam particles were produced per spill of 4×10^{10} primary protons lasting 2.58 s, in a cycle repeated every 14.4 s.

5.1.3 The experimental setup

The setup of WA89 for the 1991 run is shown in fig. 5.3, with an enlarged view of the target and vertex regions given in fig. 5.4. The beam is defined for the trigger by scintillation counters B1 and B2 and by veto counters. The transition radiation detector (TRD) [70] discriminates between π^- and Σ^-, rejecting more than 93% of the pions for the trigger, while keeping ~75% of the Σ^-s [71]. It is composed of alternating layers of multi-wire proportional readout chambers (MWPCs) and of polypropylene radiator. It operates on the principle that the transition radiation energy emitted depends on the Lorentz factor $\gamma = \sqrt{\mathbf{p}^2c^2 + m^2c^4}/mc^2$, allowing discrimination between particles with different masses (m) at the same momentum ($|\mathbf{p}|$).

Silicon microstrip detectors (with 50 μm pitch) placed before and after the TRD measure the beam particle trajectory before impacting on the interaction target. The target is composed of $0.0375\lambda_I$ of copper and carbon placed side-by-side. It is thin and dense enough to produce a maximum number of multi-hadron states without secondary interactions in the target and to allow a large fraction of charmed particles to decay outside the target [63]. The vertex detector consists of 12 planes of silicon microstrip detectors (with 25 and 50 μm pitch) for the reconstruction of the produced particle tracks and the charm decay vertices.

Many of the interesting charm decays detected by WA89 result in Λ particles which

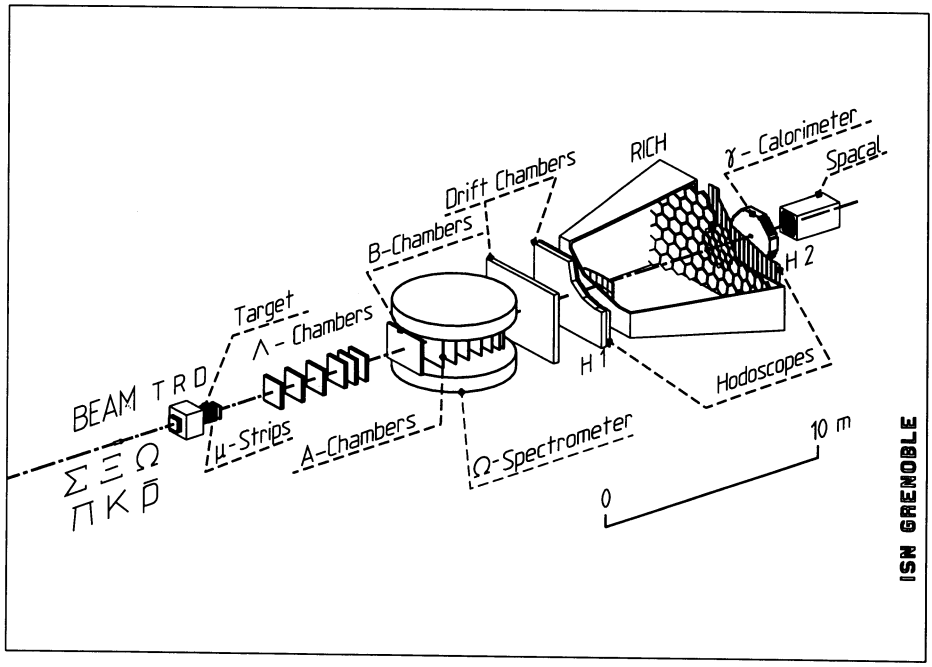

Figure 5.3: *The WA89 experimental setup in the 1991 run with SPACAL.*

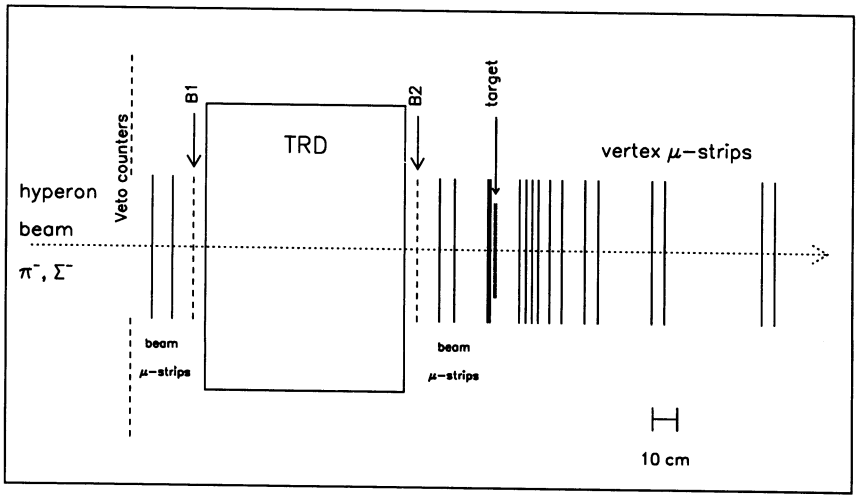

Figure 5.4: *Detailed layout of the target and vertex regions in WA89 in 1991.*

then decay themselves. These particles are detected in the so-called "Λ chambers," 38 planes of drift chambers placed along the 10 m following the vertex region. The momenta and trajectories of charged decay products are then measured by the Omega spectrometer. A set of 16 MWPCs at the entrance measures the initial trajectory into Omega. The magnet provides a bending power of 8.2 Tm. The momentum p [GeV/c] of a singly charged particle is then determined by

$$p = \frac{0.3BR}{\cos\lambda} \tag{5.1}$$

where B [T] is the strength of the magnetic field through which the particle trajectory has curvature R [m] and pitch angle λ. This track is measured by 22 additional MWPCs in the field region. After the magnet, several drift and proportional chambers measure the outgoing track. The momentum is measured by the spectrometer with a resolution of

$$\frac{\Delta p}{p} = 10^{-4}p, \tag{5.2}$$

with p measured in GeV/c.

Particles with momenta greater than ~15 GeV/c fall within the acceptance of the Ring Imaging Čerenkov (RICH) counter [72] intended for charged particle identification (of p, π, and K). A charged particle emits Čerenkov photons at an angle θ from the incident path depending on its velocity βc as it passes through the 5 m long radiator volume filled with nitrogen (with refractive index n), according to

$$\cos\theta = \frac{1}{n\beta}. \tag{5.3}$$

The radiation is reflected and focused by an array of spherical mirrors through a UV-transparent quartz window onto the photon detector, where the Čerenkov cone appears as a circle. The photons are detected by a set of 5 UV-sensitive drift chambers. The chambers, in which the photoelectrons are generated, are filled with ethane saturated with TMAE[1] at 30°C. On average, 14 photoelectrons are detected for each ring, with a spatial resolution of better than 2 mm. A mass hypothesis (and its corresponding ring) for each particle is made using the track information from the Omega chambers and the mirror geometry. A likelihood function is calculated for each hypothesis, taking into account the distance between the predicted ring radius and each hit over a constant background. A cut on the ratio of the likelihoods provides particle discrimination. Separation between protons and pions was achieved with a 90% efficiency at 150 GeV/c [73].

Placed before and after the RICH, the scintillator hodoscopes H1 and H2 form part of the trigger. The e.m. calorimeter detects γs from radiative charmed baryon decays or from π^0 decays. It consists of 642 blocks of lead glass, each measuring 75 × 75 mm^2 across and $24X_0$ deep. This homogeneous calorimeter measures the energy with

[1] tetrakis(dimethylamino)ethylene

a resolution of $\sigma/E = 5.6\%/\sqrt{E} + 0.5\%$, while the resulting resolution for the $\pi^0 \rightarrow \gamma\gamma$ invariant mass peak in the experiment is 4.2 MeV/c^2. The average spatial resolution is 6 mm [74].

During the 1991 run, the SPACAL calorimeter was placed in the last position for $2\frac{1}{2}$ weeks (both with and without the lead glass in front). With it, decay channels resulting in a neutron are accessible. A neutron produces an hadronic shower in the calorimeter from which its energy and position can be measured. The shower is distinguished from an e.m. shower by the shower dimensions (sect. 4.5), and is identified as a neutral particle by the absence of a spectrometer track correlated to the shower barycenter position measured in the calorimeter. The SPACAL performance is the main subject of this chapter. Preliminary results were reported in [75].

5.1.4 The role of the neutron calorimeter

As stated before, the basic role for the SPACAL detector is to act as a neutron calorimeter [76]. Its purpose is to measure the energy and the position of neutrons in the final state, especially those resulting from $\Sigma^{\pm} \rightarrow n\pi^{\pm}$ decays. For the Σ^-, this is the main decay channel, with a branching fraction of 99.8% [5]. It is undetectable without a neutron calorimeter. For the Σ^+, this mode accounts for almost half of all decays, with a branching ratio of 48.3%. The main decay mode, $\Sigma^+ \rightarrow p\pi^0$, is observable in WA89 with the e.m. calorimeter, but has a very high background. Therefore, a neutron calorimeter contributes to an increased sensitivity to the Σ^+.

An hadronic calorimeter provides the additional capability to study charmed baryon decay channels resulting in a charged Σ, for example, the observed decay $\Xi_c^+ \rightarrow \Sigma^+K^-\pi^+$ [77] and possible decays $\Xi_c^0 \rightarrow \Sigma^{\pm}K^-\pi^+\pi^{\mp}$. This allows a more complete study of all possible charmed baryon decay modes as measured within a single experiment.

Neutron detection is also important for a reconstruction of the H dibaryon [78]. If the H mass lies below the $\Lambda\Lambda$ threshold (2230 MeV/c^2), the only possible decay channels are weak transitions $H \rightarrow \Lambda n$ and $H \rightarrow \Sigma^- p$. The lifetime is then expected to be on the order of a hyperon lifetime, making the reconstruction of the decay vertex essential. This is possible only in the latter decay channel, which requires the use of a hadron detector.

As detailed in chapter 4, the SPACAL detector has very good hadronic energy and position resolution, suitable for neutron detection and measurement. In addition, it is fast, allowing trigger decisions. Detecting neutrons at the trigger level facilitates the study of the mentioned processes, which are, in general, characterized by low production cross sections.

5.2 The spaghetti calorimeter in the experiment

The spaghetti calorimeter as used in the beam tests described in chap. 4 needed some modifications before use in the high-rate environment of the hyperon beam (sect. 5.1.2). The bases for the PMs were modified to allow a second voltage supply, called the "booster" voltage, to be applied in order to stabilize the voltage level between the last two dynodes of the PM. Without this modification, the high anode current produced by the high particle rates during a spill would cause this voltage to drop completely, so that the base would not function at all. In addition, the output was split into two inside the base to provide signals for the neutron trigger, not implemented for this run. The cooling system for the bases was improved: compressed air was sent into the back of each base, and four fans were installed in the back of the calorimeter. This was necessary because the several watts of power produced in each base radiate a large amount of heat. The temperature was monitored by several thermistors. Finally, the response of the readout chain, from the light guide to the PM base, for each tower was monitored. Any changes in gain were then incorporated into time-dependent correction factors for the calorimeter response. The layout of this system is shown in fig. 5.5. A flashlamp produces light pulses which are diffused onto a bundle of clear plastic fibers. The other end of each fiber is inserted into the back of the readout casing alongside the base and PM to the light guide, in which the light pulses are transported. The signal is then digitized by an ADC and recorded at regular intervals when there are no

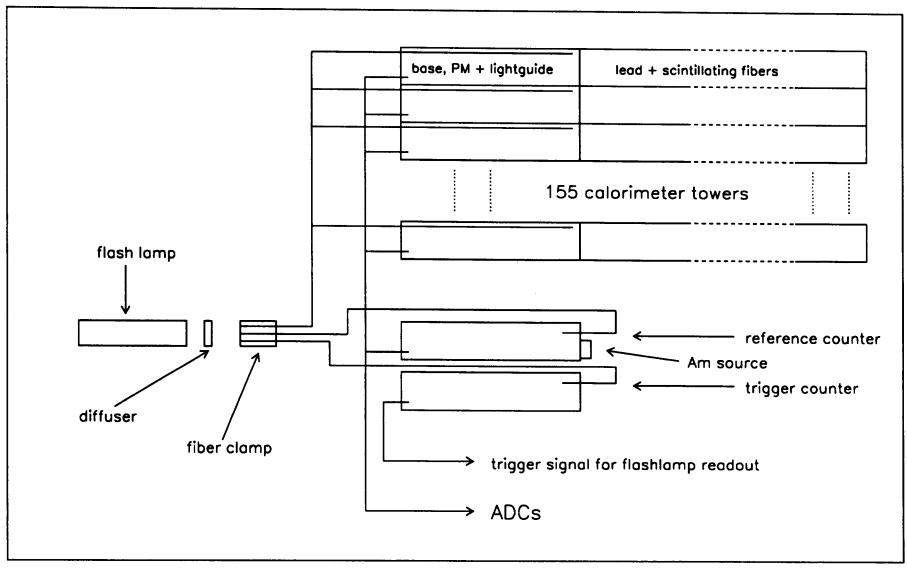

Figure 5.5: *The monitoring system for the SPACAL readout chain. See text for details [79].*

particles in the calorimeter. The trigger for the readout of the light pulses is provided by putting another fiber to a PM outside the calorimeter. The flashlamp was tested to be very stable, with little variation between pulses. This variation is monitored by comparing the flashlamp signal to a mono-energetic ^{240}Am α source. The source is attached to a scintillator tile which is coupled to a PM outside the calorimeter. A fiber from the flashlamp also sends light pulses to this PM, resulting in two pulse height spectra: the constant α spectrum as reference and the variable flashlamp spectrum. Temperature information from a thermistor next to the reference PM is used to correct its response.

Information from the monitoring system was used to identify malfunctions in the readout chain (*e.g.*, the PM, the base, or a cable) or in the high voltage supply, and efforts were made to replace the faulty element. In the end, only two channels with fluctuating signals and two with no signal could not be repaired.

In both the test beam and experiment, the signals from the calorimeter were treated in the following way. One output of the calorimeter base went to Fastbus 1885F analog-to-digital converters (ADCs), which have two ranges. The low range gain is 0.05 pC/count $\pm$ 3% and the high range gain is 0.4 pC/count $\pm$ 5%, with a 12-bit dynamic range for each. Data could be taken with one of three modes: low range, high range, or "autorange," which switches between the high and low ranges for the best precision. The ADC pedestals were recorded by the monitoring system as described above during a separate trigger driven by a pulser. After ~150,000 events, the average pedestals for each channel were collected in a separate record. On-line or off-line, the pedestals from either source could be subtracted from the signals. The flashlamp monitoring system and high voltage control and check task were running during most of the beam time. The data was recorded by DECstation RISC-processor computers.

5.3 Single-tower calibration of the calorimeter

There are many ways to calibrate a calorimeter to obtain the correct energy measurement from the calorimeter signals. In the case of SPACAL, electron showers are used because they are contained in the entire calorimeter and their response with respect to the response to hadron showers (e/π ratio) has been precisely measured, allowing the extrapolation in the case of hadronic showers. However, it turned out that an additional energy calibration with hadrons was required. This proton calibration is discussed later in sect. 5.4.2. Muons (either from a beam or from cosmic rays) are frequently used to calibrate calorimeters. The muons are easily contained transversely in one tower, allowing inter-modular calibration. The relation between the muon response and the electron response must then be known, as well as the response to hadrons, to determine the absolute energy conversion. This was successfully done for the 20-tower spaghetti calorimeter prototype (sect. 4.1) when it acted as a leakage detector for the full calorimeter in the H2 test beam [59]. In the case of a detector (often consisting of many cells) that needs to be calibrated often, and which cannot be disassembled

and placed in a test beam, a radioactive source may be used for time-dependent calibration between cells. In a uranium calorimeter, the constant background radiation can be used. In the case of SPACAL, the use of a radioactive source was investigated. This is discussed in sect. 5.3.5.

5.3.1 Test beam setup

The calorimeter towers were calibrated with electrons during two test beam periods, before (in April) and after (in September) the WA89 run in June 1991, in the X3 beam line at the CERN SPS. The X3 beam is a tertiary beam derived from the H3 secondary beam and provides electrons and hadrons of momentum between 2 and 50 GeV/c [80]. The layout of the X3 beam line after the first quadrupole and bending magnet is shown in fig. 5.6. A spectrometer consists of two delay-wire chambers [81]

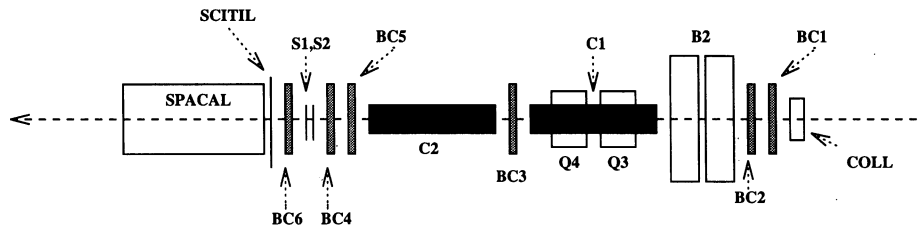

Figure 5.6: *A schematic of the X3 test beam line after the first bending magnet and quadrupole magnet, during the SPACAL tests. See text for details. (Not drawn to scale.)*

(labeled BC1 and BC2) upstream and two of the same (BC3, BC4) downstream of the last bending magnet (B2). This magnet bends in the horizontal direction and so the chambers are only sensitive to this coordinate. In addition, there are two delay-wire chambers (BC5, BC6) giving both the horizontal and vertical positions of the beam particle. The beam size is defined in the horizontal and vertical directions by collimators (COLL) and focusing quadrupole magnets (Q3, Q4). The beam is further defined for the trigger by two scintillator counters (S1, S2) of 2×2 cm^2. The particle type is selected using different targets and by adding an electron absorber of 5-mm lead for charged pions. In addition, two Čerenkov counters give particle identification between pions, electrons, and muons. One or both counters were included in the trigger at any given time.

The calorimeter was prepared as described in sect. 5.2 and was placed at an angle of 3° between the fiber axis and beam direction. It rested on a support that could move by remote control horizontally (x) and vertically (y) in the plane perpendicular to the beam direction. The position of the support was recorded by the data acquisition system. In order to find the absolute position of the beam on the calorimeter, the beam was centered on a tower with a precision of ~1 mm. This was done by scanning

across horizontally and vertically and finding the edges of the tower (*i.e.*, when there is a large decrease in the signal from the tower). Halfway between was taken to be the center.

5.3.2 Summary of data

The main purpose of the test beam periods was to calibrate the calorimeter. No modifications or repairs were made to the calorimeter system between the test beam periods, so that any changes in signal were due to the experimental conditions alone.

In the April beam test, the voltages of the PM bases were adjusted such that the average signals from 50 GeV electrons steered into the center of each tower (within a few millimeters) were 450 high range counts (±2%), for an average gain of 3.6 pC/GeV. At this value, the whole ADC range is utilized at the hyperon beam energy (330 GeV). Then electron beams of 10 and 30 GeV were directed to the tower centers for both ranges of the ADC, and ~1000 events were recorded for each tower at a single energy and ADC range. This is the data from which the calibration factors were determined. The data sample includes events occurring at positions between tower centers in addition to those at the tower centers.

In the September beam test, the same was done with electron beams of 10, 30, and 45 GeV. The position display of the support was not always reliable during this time, causing the actual position to be sometimes several centimeters from the desired position. For each tower at a single energy, ~9000 events were recorded with the low ADC range and ~6000 with the high range.

5.3.3 Calculation of calibration constants

The purpose of a calibration is to determine the factor which converts the calorimeter signal into an accurate energy measurement. A calorimeter is usually divided into smaller units, with each unit having its own "calibration constant." With the calibration constants applied, the same energy value is found no matter where the particle entered in the calorimeter. Changes in the response with respect to time, temperature, and other external conditions, requiring additional factors, are dealt with separately from the calibration constants, and will be discussed later.

With SPACAL, the goal of the calibration runs was to get sets of calibration constants in units of GeV per ADC count for each tower at different energies (to check the linearity) and for the two ranges of the ADC. The factor between the ranges is nominally 8 low range counts for each high range count for the same signal (sect. 5.3.1), but in practice may vary from one ADC module to the next by as much as ~6%. Another approach is to calibrate the ADCs separately, by sending in different amounts of charge and comparing with the resultant ADC signals. Then separate conversion factors for the ADCs can be used to convert from one range to another, with only one set of calibration constants needed. In fact, it will be shown that the methods used do not provide a very good determination of the ratio of the two ADC range gains.

A separate ADC range calibration was done after the test beam periods and is not included in the results here.

Two methods of determining the calibration constants were employed.

The "fraction" method

Since practically an entire electron shower is contained in one tower of the calorimeter (sect. 4.3), there is a straightforward method of determining the calibration constants. One aims the electron beam into the center of a tower, then finds the mean value of the (ideally Gaussian) distribution of the signal from that tower. Then one assumes that this signal is a known average fraction of the beam energy, in this case 95%. For the spaghetti calorimeter, the calculation of the calibration constant C_i is as follows for tower i with an uncalibrated mean signal μ_i:

$$C_i \left[\frac{\text{counts}}{\text{GeV}}\right] = \frac{\mu_i[\text{counts}]}{0.95E\ [\text{GeV}]}, \tag{5.4}$$

where E is the energy of the incident beam.

This "fraction" method is reliable because one can see any problems with individual towers right away by scanning the results of the fits and checking the histograms. The towers are treated separately, so that if there is a problem with a neighboring tower, it does not affect the results. However, there are many sources of uncertainty. One needs to be sure that the beam enters the center of each tower, in order to have equal containment in each. Using the average fraction contributes to the uncertainty, since the fraction of energy contained in a tower fluctuates from event to event. Lastly, the beam energy should be well known. This method was used to determine the calibration constants for the 20-tower prototype. The results were found to agree within 1% with the constants found using the following method for the same prototype [82].

The "matrix" method

Another method to determine calibration constants is based on the energy sharing between towers of the calorimeter. It is easy to derive this procedure for two towers, then generalize it to an arbitrary number of towers. Assume these two towers contain the full shower and have signals S_1 and S_2 (in units of counts or pC, for example). We want to find their calibration constants α_1 and α_2 (in units of GeV/count, for example), such that the energy (in GeV) contained in towers 1 and 2 are $S_1\alpha_1$ and $S_2\alpha_2$, respectively. The total energy contained (assuming no leakage) is equivalent to the known particle energy E, *i.e.*

$$E = \alpha_1 S_1 + \alpha_2 S_2, \tag{5.5}$$

but the energy sharing between the towers varies from event to event. When the containment in each tower is the same, the uncalibrated signal distribution is centered around a different mean signal, so that the total distribution is quite broad, as shown in

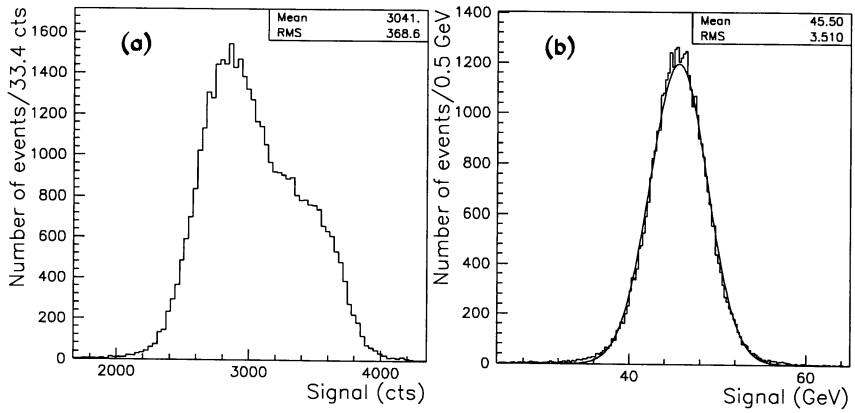

Figure 5.7: *The distribution of 45 GeV electrons entering many different SPACAL towers, (a) without calibration constants, and (b) with calibration constants applied. The curve is the result of a Gaussian fit. Data from the second test beam period.*

fig. 5.7*a*. The width of the total signal distribution is minimized when both channels give the same mean signal for the same amount of energy, *i.e.*, when the correct calibration constants are applied (fig. 5.7*b*). The σ_{RMS} of this sum of distributions over N events is

$$\sigma^2_{\mathrm{RMS}} = \frac{1}{N}\sum_{k=1}^{N}(\alpha_1 S_1^k + \alpha_2 S_2^k - E)^2. \tag{5.6}$$

To find α_1, eq. 5.6 is minimized with respect to this variable,

$$\frac{\partial \sigma^2_{\mathrm{RMS}}}{\partial \alpha_1} = \frac{2}{N}\sum_{k=1}^{N}(\alpha_1 S_1^k + \alpha_2 S_2^k - E)S_1^k = 0, \tag{5.7}$$

which expands to

$$\alpha_1 \sum_{k=1}^{N} S_1^k S_1^k + \alpha_2 \sum_{k=1}^{N} S_1^k S_2^k - E\sum_{k=1}^{N} S_1^k = 0. \tag{5.8}$$

This can be simplified by defining constants:

$$\begin{aligned} a_{11} &= \sum_{k=1}^{N} S_1^k S_1^k, \\ a_{12} &= \sum_{k=1}^{N} S_1^k S_2^k, \\ b_1 &= \sum_{k=1}^{N} S_1^k. \end{aligned} \tag{5.9}$$

Eq. 5.8 is then rewritten as

$$a_{11}\alpha_1 + a_{12}\alpha_2 = Eb_1. \tag{5.10}$$

The same is done for α_2 by minimizing the total σ_{RMS} with respect to α_2, resulting in a similar expression:

$$a_{21}\alpha_1 + a_{22}\alpha_2 = Eb_2. \tag{5.11}$$

where the constants are defined as

$$\begin{aligned} a_{22} &= \sum_{k=1}^{N} S_2^k S_2^k, \\ a_{21} &= \sum_{k=1}^{N} S_2^k S_1^k, \\ b_2 &= \sum_{k=1}^{N} S_2^k. \end{aligned} \tag{5.12}$$

Eqs. 5.10 and 5.11 form a linear system of equations, appearing in matrix notation as

$$\begin{pmatrix} a_{11} & a_{12} \\ a_{21} & a_{22} \end{pmatrix} \begin{pmatrix} \alpha_1 \\ \alpha_2 \end{pmatrix} = E \begin{pmatrix} b_1 \\ b_2 \end{pmatrix}, \tag{5.13}$$

which can be solved to find α_1 and α_2. Now it is easy to generalize to a larger number of towers, *e.g.*, 155 towers in the case of SPACAL. For tower i, eq. 5.10 generalizes to

$$a_{ij} \sum_{j=1}^{155} \alpha_j = Eb_i, \tag{5.14}$$

where

$$\begin{aligned} a_{ij} &= \sum_{k=1}^{N} S_i^k S_j^k, \\ b_i &= \sum_{k=1}^{N} S_i^k. \end{aligned} \tag{5.15}$$

For all the towers, this is written in vector notation as

$$\mathcal{A}\vec{\alpha} = E\,\vec{b} \tag{5.16}$$

where $\mathcal{A}$ is the matrix of elements a_{ij} with $i, j = 1, \ldots, 155$ and $\vec{\alpha}$ and $\vec{b}$ are vectors containing 155 elements α_i and b_i, respectively. This equation can be solved using standard computer library routines. In the calculation for SPACAL, the constants C_i found are the inverse of those described above, *i.e.*, $C_i[\mathrm{counts/GeV}] = 1/\alpha_i$, for convenience.

This "matrix" method is very elegant. The data for all towers can be processed altogether and then the system of equations solved, with the only requirement that there is some significant showering in each tower. The calculation does not depend

on the position of the entering particle. However, there is some uncertainty when the particles enter close to the edge of the calorimeter, since there is some leakage. This should be a small effect. Another disadvantage comes when using an imperfect device, for example, if there are malfunctioning towers. The signals from these towers can distort the results of the calculation, since all the signals are combined according to eq. 5.16. In addition, some unknown malfunctioning towers may not be found, since there is no explicit check of individual towers during the calculation. Also, the beam energy should be well known for an accurate absolute energy calibration. This is the method used for the first beam tests of the calorimeter (chap. 4).

Both methods described above were used with electron shower data to extract the calibration constants for the SPACAL detector in WA89.

5.3.4 Results of calibration

The following cuts were made to clean up the data samples from both calibration runs:

- The particle was required to pass through beam chambers 1 to 4 (see fig. 5.6). Tighter cuts on the chambers made little difference to the resulting signal distributions, except for reducing the already small number of events. In April, the beam size was no larger than $\sim$2 cm in the horizontal direction and $\sim$1.5 cm vertically. In September, the beam spot was roughly 2×2 cm^2.

- A cut was made on the total signal (in counts) to remove probable muons, which deposit much less energy in the calorimeter. This cut, at $\sim$20% of the total signal, was used only for the April data, when the Čerenkov counters were not in the trigger. It was not necessary for the September data.

- Pions were removed using two algorithms:

  i. The fraction of the total signal contained in the tower being calibrated gives good e/π separation, but the beam must enter the center of each tower. For this reason, this cut was only used in the fraction method calculations. Fig. 5.8 shows this quantity for a contaminated 30 GeV e^- beam. One clearly sees the electron peak, with a smaller, broader distribution at a lower fraction, due to π^- contamination. The cut required a fraction greater than 60% in order to be an electron. The values greater than 1 are due to the inaccurate pedestal values which result in many negative signals in the outer towers where there should be no signal. It was seen that the energy in the center tower as a fraction of the total energy contained within one, two, and three rings is always less that 1, but with the addition of a fourth ring, negative values appeared.

  ii. For the matrix method, no cut on the position is required, so the previous pion cut cannot be used. Therefore, a method studied in the previous beam tests (sect. 4.5.1) was used, namely the cut on containment in the cluster

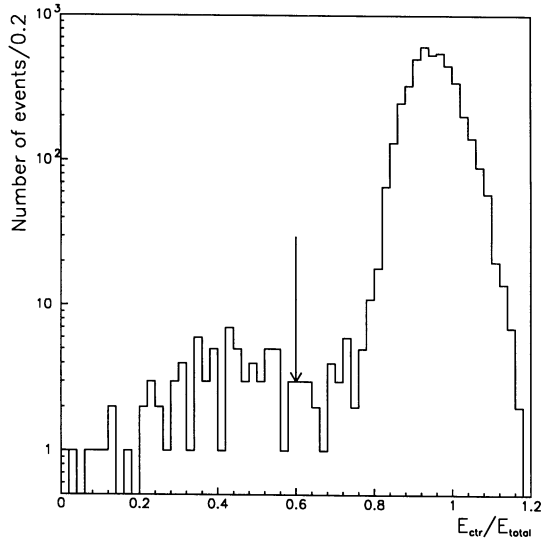

Figure 5.8: *The fraction of the signal contained in the tower into which the particle enters for a 30 GeV electron beam contaminated by pions. The April data is used, and the signal was treated in low range ADC counts without calibration constants.*

of three towers containing the most energy. Fig. 5.9 shows this quantity $\mathcal{C}$ (eq. 4.18) for a 45 GeV e^- beam with high π^- contamination. The suggested cut of 0.97 guarantees that the particle is an electron with high certainty, but also cuts many of the events in this case. This cut had been optimized in the previous beam tests for 80 GeV events, and the electron peak here is a little broader than from the previous data since calibration constants have not been applied. Therefore, a cut at $\mathcal{C} = 0.90$ removes most of the π's from the sample, with an acceptable reduction of the number of electron events.

Double hits were very rare and did not require a cut.

In addition to the cuts on the beam, specific cuts were necessary for the calculations. For the fraction method, the vertical and horizontal support positions were required to be within 1 mm from the center of the tower. Any "bad" channels, *i.e.*, those without a signal or with a highly fluctuating signal due to a malfunctioning readout element (see sect. 5.2), were left out of the calculation by setting their signals to zero. The matrix calculation, however, is sensitive to large variations in neighboring towers, since it relies on the energy sharing between towers. Therefore, the signals of these known unreliable channels were only set to zero if they were more than one ring of towers away from the impact tower, the one with the highest signal. If the "bad" tower was neighboring the impact tower, its signal was set to the average of the other (working)

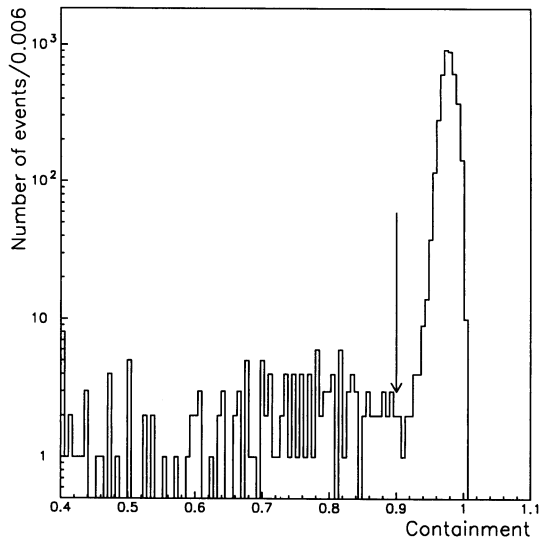

Figure 5.9: *The containment C as defined in the text for a 45 GeV electron beam contaminated by pions. September data is used, and the signal was treated in low range ADC counts without calibration factors applied.*

towers in the first ring around the impact tower. If the particle entered a "bad" tower, then the event was left out altogether.

Both calculation methods were used for the April data. After cuts, ~500 events were available for each tower at one energy and ADC range, for both methods. The data sets differed mainly in that the data for the matrix method includes data recorded between tower centers. Since the support position control was not reliable in the September tests, there was not data for the centers of all the towers, so the calibration constants were calculated using the matrix method. In fact, this was also expected to work better than it did for the April data, since there was more data taken all over the tower surfaces, not just the centers. After cuts, ~5000 events on average had an impact point on each tower at a single energy and ADC range.

An intrinsic property of the calorimeter, namely, non-uniformities of ~3% due to fiber-to-fiber fluctuations, limits the precision of the calibration constants. The fraction method, for instance, only uses data taken at one point on the tower. If another point was the impact position for the calibration and the tower was not very uniform, this calibration constant may be different by as much as 3%. If the matrix method is used and there is data taken at many different points on each tower, the resulting calibration constants are averaged over the non-uniformities of the tower response.

Comparison of methods

With the fraction method, the signal distributions for the single towers were very well described by a Gaussian function, as in the example shown in fig. 5.10 for the April data. For the constants derived using the matrix method, reasonable results were found for the 30 GeV data with the low ADC range, but was less reliable for the 10 GeV data and 30 GeV high range data. In fig. 5.11*a* and *b*, the constants found using the 30 GeV data with the low ADC range agree on average, but there is a ~2% spread on this correlation. For the high range (fig. 5.11*c,d*), the correlation is much worse, with a wide spread in the constants derived from the matrix calculation. The correlation is even worse for the 10 GeV data, as shown in fig. 5.11*e* and *f* for the low ADC range. The spread in the "fraction" values is comparable to that for the 30 GeV data, but the range of "matrix" values is much broader. Non-uniformities across the surface of a tower also contribute to the spread, since the matrix data includes points away from the tower centers. One can conclude that the matrix method works better when there is significant energy sharing between towers. In the case here, usually only about 5% of the total energy is shared between the surrounding towers. In the latter two cases, the ADC was not sensitive enough to the signals in the towers around the impact tower, either because it was in the high range mode or the signals were just very low because the beam energy is low.

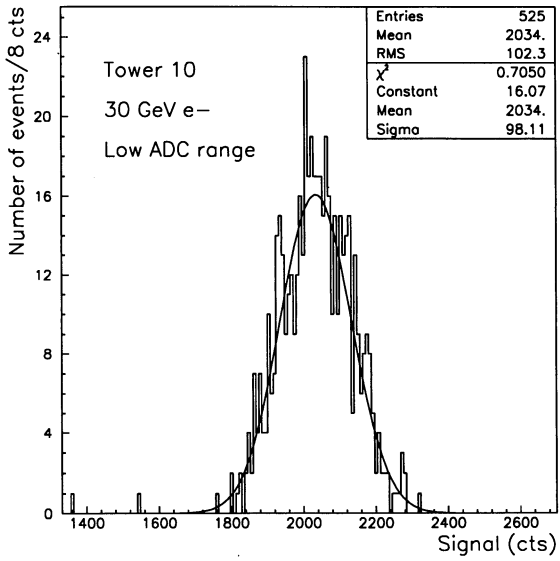

Figure 5.10: *The distribution, with a Gaussian fit, for 30 GeV electrons entering the center of tower 10, as used in the "fraction" method for calculating calibration constants.*

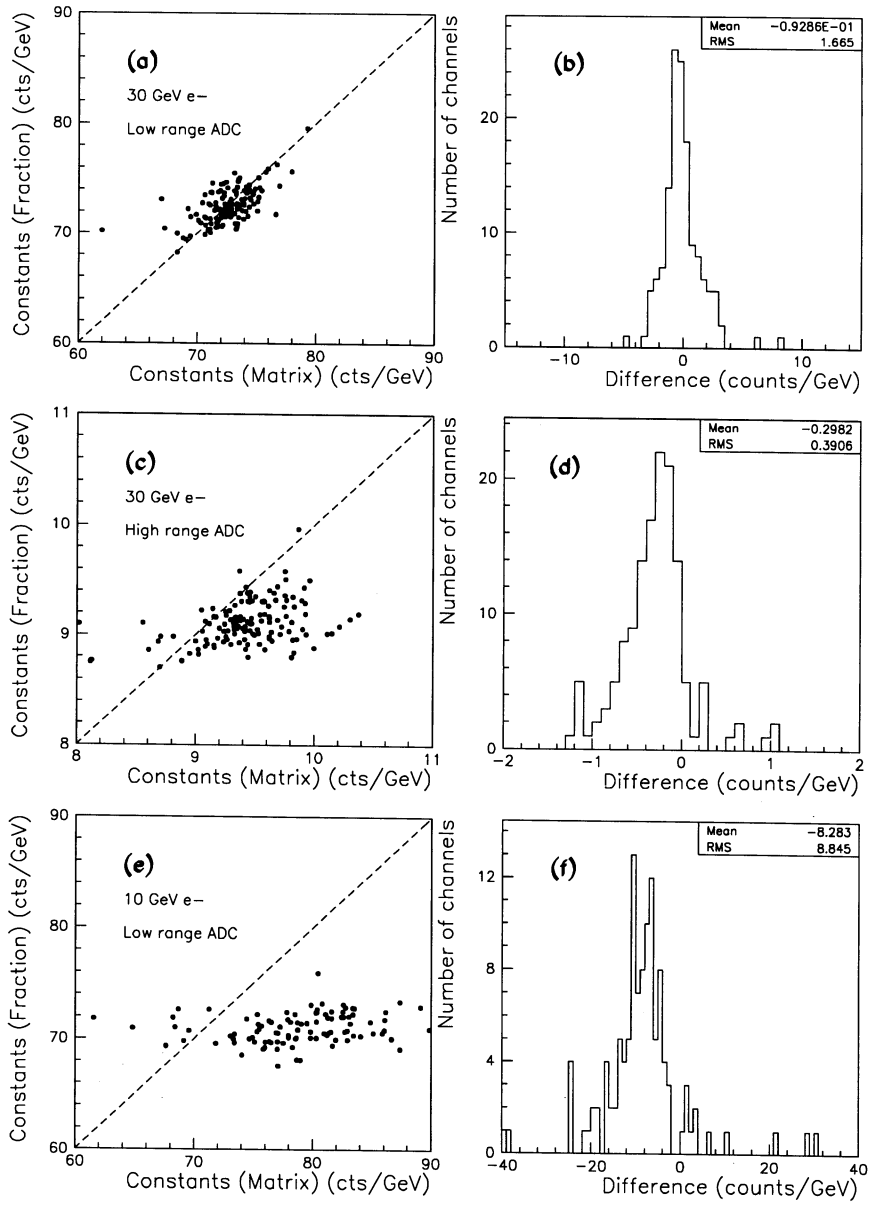

Figure 5.11: *Comparison between calibration constants calculated using the fraction method and those calculated by the matrix method. In the first column (a,c,e), they are compared in a scatter plot, where the dashed line marks equal values; in the second column (b,d,f), the differences for the same data are plotted. The data sets used are noted on the figure.*

Comparison at different energies

Since the gains of the PMs had decreased over the WA89 run (to be discussed in sect. 5.4.1), a comparison between April calibration constants and September constants does not yield any information about the calculation methods used. Therefore, it is only possible to compare the data taken at different energies in September, which is done in fig. 5.12. The calculations using the 30 GeV data agree on average with those using the 45 GeV data, as shown in fig. 5.12*a* and *b*. Since the data sets are different, some of the spread is due to the non-uniform tower surfaces. In fig. 5.12*c* and *d*, these constants are compared to those derived from the 10 GeV data. The latter constants are systematically higher by ~4 counts/GeV. This is most likely due to uncertainty in the knowledge of the beam energy. The energy of the beam was probably underestimated, and so the calibration constants were overestimated. In addition, as seen in fig. 5.11, the matrix method is less reliable at lower energies.

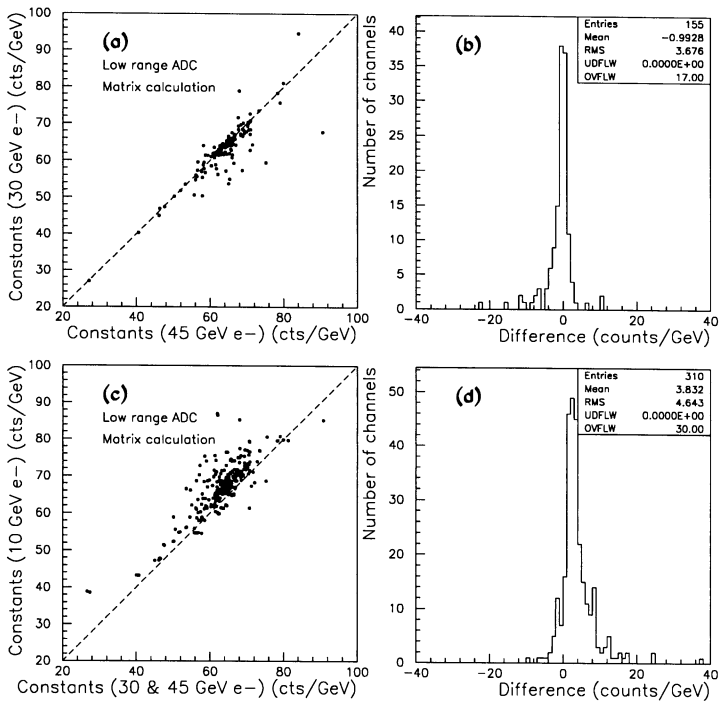

Figure 5.12: *Comparison between constants derived from 30 GeV e^- data and those from 45 GeV data, in the form of (a) a scatter plot and (b) the difference between them. Constants from both data sets are compared to those derived from the 10 GeV e^- data in (c) and (d).*

Comparison at different ADC ranges

The ratio of the calibration constants from September 30 GeV data for the low and high range (fig. 5.13) falls around 7.9, close to the expected factor 8 between the ranges. This gives additional confidence in the matrix method for this data. The spread of ~2.5% is better than the 6% taken from the ADC specification (see sect. 5.3.1), and includes the effects of having data from different positions on the calorimeter surface. However, a separate ADC calibration would give more exact measurement of this ratio.

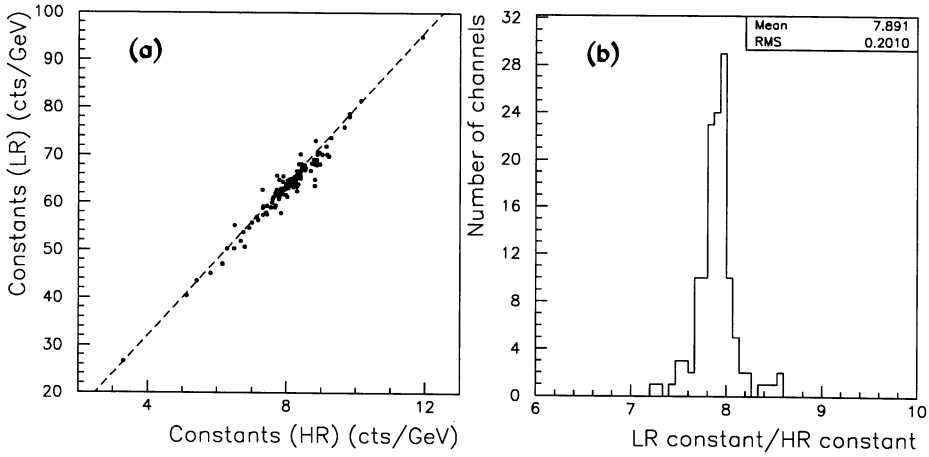

Figure 5.13: *Comparison between calibration constants calculated using the matrix method from low ADC range (LR) data and those from high ADC range (HR) data, from the September test beam run of 30 GeV electrons: (a) in the form of a scatter plot, where the curve represents the nominal relation between the ranges, and (b) the ratio of the LR constant to the HR constant.*

Discussion of results

There were some major drawbacks of using the fraction method with this setup of the SPACAL in addition to those discussed in sect. 5.3.3. First of all, the number of events for each tower was low (~500), contributing a significant statistical error in the calculation of each calibration constant. As discussed in sect. 5.3.3, the 95% containment is only an average. Additional variations of the containment fraction resulted from the uncertainty on the calorimeter centering.

The matrix method seems to be the better method for this case. Using this method, there is no need to cut on the position, increasing the number of events and reducing the statistical error. However, the "bad" towers had to be corrected in order to calculate the correct calibration constants for the rest of the towers. In addition, this method was not reliable for the cases where there was little energy sharing: in the case of the

lower energies and when the high range of the ADC was used, since there was less precision on the small amounts of energy contained in some towers. However, the high range constants can be derived from the low range range constants if one knows the correct factor between the ranges.

Final calibration constants

The conclusions from these calculations were used to finalize one set of calibration constants each for the April and September data, which could then be used in the analysis of the data from the WA89 run as well, in conjunction with the correction factors provided by the monitoring system. For the April data, most of the final calibration constants from the low ADC range data were taken from the averages of the constants found with the fraction method and those with the matrix method at 30 GeV, if both were available. Otherwise, one or the other was used. In a very few cases with no data at 30 GeV, the 10 GeV factor calculated with the fraction method was used, with a correction to account for the discrepancy of this data compared to the data at other energies (fig. 5.12). No calibration constants were available for 2 towers that had highly fluctuating signals and for one tower that had no signal at all. For the high range calibration constants, the constant by the fraction method was used for most of the towers. For the rest, the low range constant divided by the average factor 8 (= low range counts:high range counts) was used.

For the September data, the final calibration constants from the low ADC range data were derived from the averages of the constants from the 30 GeV data and those from the 45 GeV data. In a few cases, only one or the other, or the corrected 10 GeV factor, was used. No calibration constants were available for two towers that had highly fluctuating signals and for two towers that had no signal at all. For the high range calibration constants, the constants from the 30 GeV data were used for most of the towers. For the rest, the low range constants divided by a factor 8 were used.

For the analysis, the September calibration constants were used, as they are more reliable than the April constants.

5.3.5 Calibration with a radioactive source

Another way of calibrating the calorimeter was tested before the WA89 run. A ~10 mCi flat ^{60}Co source, in the shape and size of a SPACAL hexagonal tower, was placed on the front face of 60 of the calorimeter towers. The PM response was compared with the calibration constants derived from the April low ADC electron data, shown in fig. 5.14. The values agree within ~4%. The difference between the two sets of results can be attributed in part to the difference in the volume calibrated. The source covered the whole surface of the tower, so the resulting signal was effectively averaged over all non-uniformities, whereas the electron beam was narrow (~1 cm diameter) hitting only one small area. With a variation of ~3% in response over the surface, a difference is expected. In addition, the electron showers penetrate deeper into the calorimeter than the γs from the source. The spread in fig. 5.14 also includes the uncertainty on

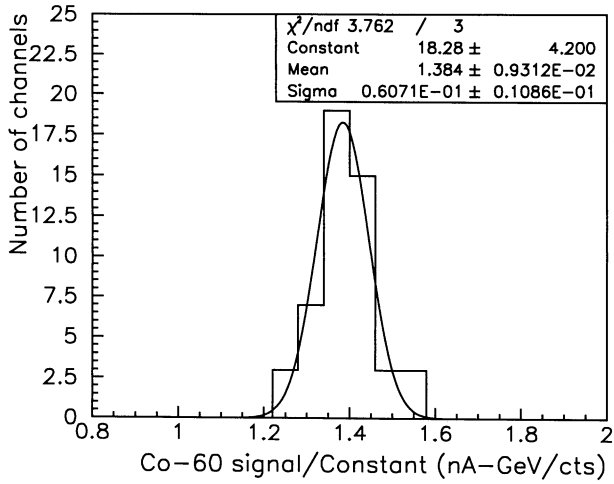

Figure 5.14: *The ratio of the signal (in nA) from the cobalt source measurement to the calibration constant (in counts/GeV) derived from electron data for 60 SPACAL towers.*

the calibration constant, as well as systematic errors in the source measurement. More study on this technique is necessary, with comparison to calibration constants derived from particles hitting the tower surface at many different impact points.

5.4 Neutron detection with SPACAL

5.4.1 SPACAL setup in WA89

The SPACAL detector was placed downstream of all the other elements of WA89 (sect. 5.1.3), just behind the lead glass e.m. calorimeter for a period of $2\frac{1}{2}$ weeks at the end of the 1991 running period. The e.m. calorimeter was moved out of the beam line for one week of this time. The two configurations of SPACAL with respect to the e.m. calorimeter are shown in fig. 5.15. In the following analysis, only the data taken without the e.m. calorimeter is used. The spaghetti calorimeter was centered (within several mm) on the path of the undeflected beam (with the Omega magnet turned off for this centering). The deflected beam particles entered $\sim$ 12 cm away, in tower 12 (fig. 4.2). The fibers were running parallel to the beam line.

The rate of particles in the hyperon beam (sect. 5.1.2) is much higher than in the test beam, and some problems resulted from this. The most obvious effect was a drop in the response of all the towers, especially those nearest the beam impact point. The response in tower 12 dropped the most, by $\sim$60% from the original response, while the response of a typical tower on the edge of the calorimeter decreased by $\sim$15%. After applying the corrections derived from monitoring the PM gains (sect. 5.2), the

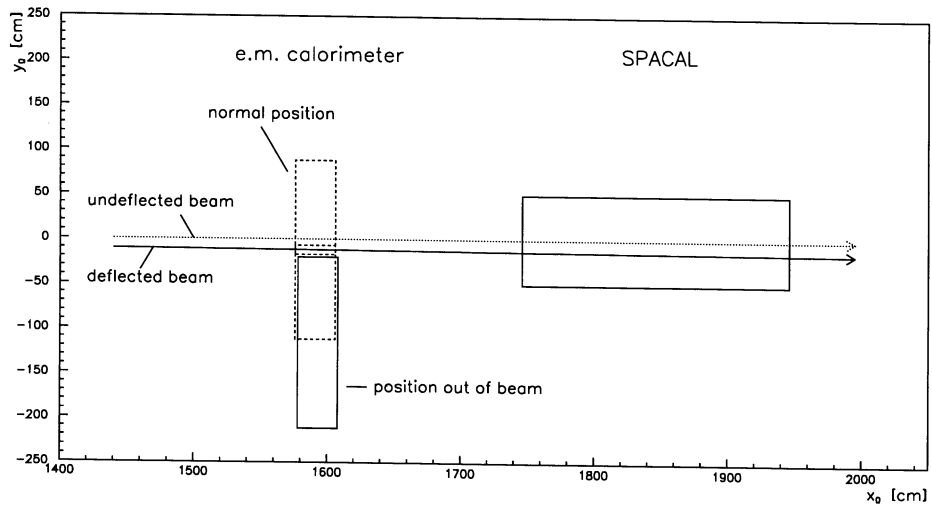

Figure 5.15: *The positions in the experiment of the lead glass e.m. calorimeter and the SPACAL hadronic calorimeter during the last $2\frac{1}{2}$ weeks of the run. SPACAL was centered on the undeflected beam path, while the e.m. calorimeter was in its normal position in the beam for $1\frac{1}{2}$ weeks and out of the beam for the rest of the time [79].*

signal in tower 12 remained constant within 2% over the course of $2\frac{1}{2}$ weeks (fig. 5.16). This indicates that there has been aging of the readout system (which is monitored), not radiation damage to the scintillating fibers in the calorimeter. The most probable cause of the signal drop is accelerated aging to the dynode surfaces of the PMs [83].

A variation in the response with the particle rate was also observed by checking the pedestal signal during a spill ("in-spill"). Normally, the pedestals are taken as the ADC signal during the time between spills ("off-spill"). The pedestal signal during a spill could also be measured, as it appears as a peak in the ADC distribution well-separated from signal peak resulting from showers. A dependence of the average value on the beam particle rate was found, as shown in fig. 5.17 for towers 12, 4, and 1 in the beam region and for tower 120, far from the beam region. (See fig. 4.2 for positions.) Initially, this was attributed to an increase in PM gain with increasing rate. In the 1993 run, however, this in-spill rate dependence disappeared for the most part after event pile-up within the calorimeter readout gate width was eliminated. This was done by shortening the gate width from 340 ns to 130 ns (still long enough to contain a hadronic shower) and the event was vetoed if the beam trigger detected another particle less than 150 ns before or after the event. With this modification, the rate dependence practically disappeared. Therefore, we concluded that the increase in signals with the rate in the 1991 run is primarily due to an increase in the number of showers from other events within the 340 ns gate, and not due to a change in PM gain. This is evident in fig. 5.17. Tower 12, at the position of the beam, is more likely

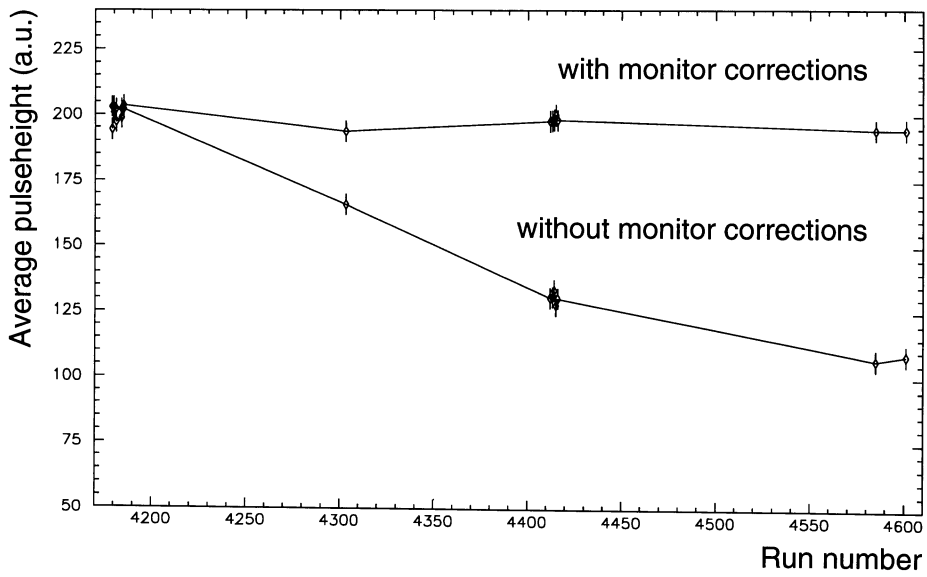

Figure 5.16: *The average signal in tower 12, which contains the impact point of the beam, as a function of time, with and without monitor corrections. The horizontal axis corresponds to time over the running period of* $2\frac{1}{2}$ *weeks [79].*

to have pile-up than the neighboring tower 4 as the beam particle rate increases. Far away from the beam region in tower 120, almost no effect is evident. This effect is correctable to some degree. The change in signal was found to be linearly correlated with the rate, albeit with a non-negligible spread. A parametrization of the average dependence was made for each channel. Correction factors were determined separately for the pedestal signal and for the calorimeter signal.

At the end of each run, the pedestals were averaged and these averages were recorded in a file. They were then corrected for the pile-up for each event, as described above. Some checks were made on the mean and σ_{RMS} of the pedestal values to determine unstable or dead PMs or connections. In addition, occasionally a general "jump" in pedestal values occurred, because of some instability in the electronics crate. These runs were identified and excluded from the analysis. As it turned out, there was evidence of inaccurate pedestal values (taken from the average). In later beam tests, another method of extracting the pedestal values was by taking the mean of a Gaussian fit on the histogram of the values, which better excludes anomalous values. These pedestal values were found to be more reliable [84].

Before analysis, the raw ADC signals were treated in the following way:

i. The pedestals, as defined above, were corrected for the dependence on the particle rate.

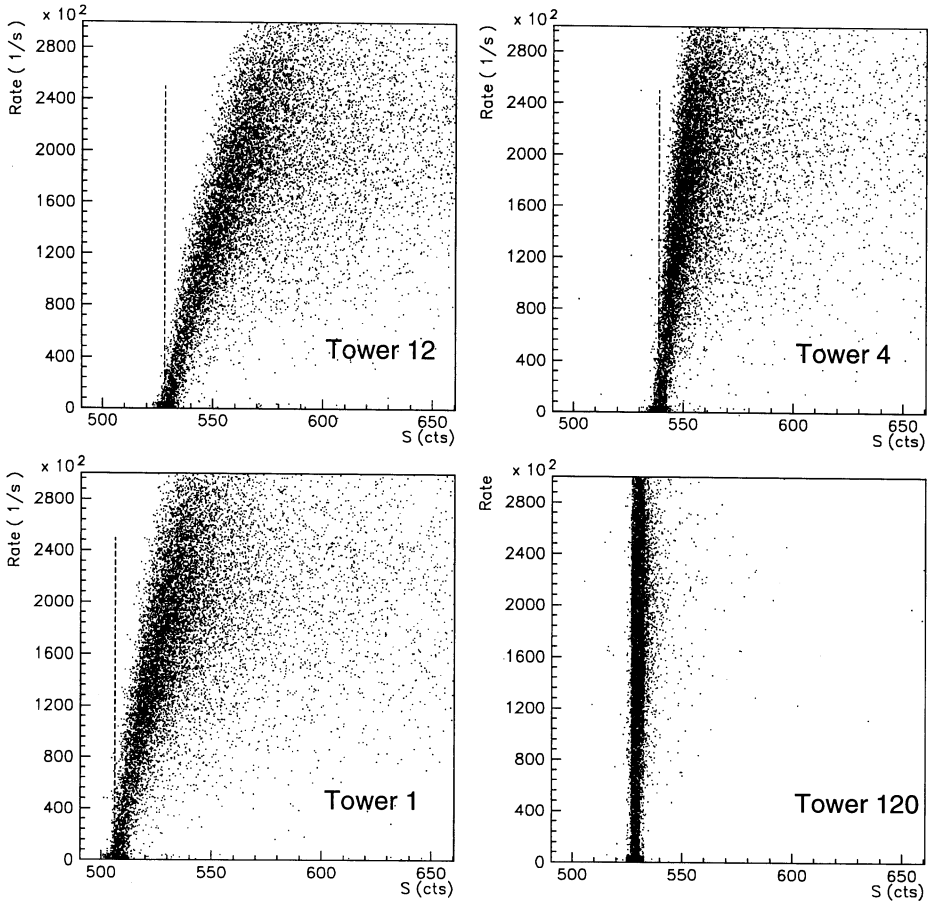

Figure 5.17: *The beam particle rate versus the pedestal signal (in ADC counts) measured during a spill for several spaghetti calorimeter towers. Towers 12, 4, and 1 are in the beam region, whereas tower 120 is far from this region, on the edge of the calorimeter [79].*

ii. The pedestals were subtracted from the calorimeter signals.

iii. The calibration constants were applied to the pedestal-subtracted ADC values. For the following analysis, the calibration constants derived from the September 1991 calibration run after the experimental run were used.

iv. The signals were then corrected for the long-term variations in the PM gain, using the monitor factor extracted for that run.

5.4.2 Hadronic energy calibration

Before proceeding to the Σ^- reconstruction with SPACAL, some checks and corrections were made to ensure correct energy and position measurements for hadrons. This was necessary because the calorimeter performance had only been measured under good test beam conditions. In this case, ~98% shower containment could be achieved by sending the particle in the center, with beams of well-known energies, thus resulting in a good energy measurement. In addition, only one particle entered the calorimeter per event, so the signals from all the calorimeter towers could be used. Finally, the calorimeter was calibrated only with electrons for this run, with no tests with hadrons over the relevant energy range.

The calorimeter also measures the position of a particle, which can then be used in conjunction with tracking information to reconstruct the angle of a particle trajectory. However, in SPACAL the barycenter of the shower is found directly, not the impact position, and these will differ if the angle between the particle trajectory and the fiber axis $\theta_z \neq 0$, according to eq. 4.7.

In order to check SPACAL energy and position measurements, protons resulting from the decay $\Lambda \rightarrow \pi^-\mathrm{p}$ were used. The momentum of the protons, measured with high resolution by the Omega spectrometer (eq. 5.2), covers a range from about 40 to 290 GeV/c. In addition, the impact point of a proton on SPACAL can be determined by extrapolating its trajectory using tracking information about its position and angle upon leaving the spectrometer. A wide range of positions of proton showers were available.

The protons were selected using information from all the WA89 sub-detectors (sect. 5.1.3 and fig. 5.18). Using the tracks reconstructed in the microstrip detectors, Λ-chambers, and Omega chambers, all vertices resulting in oppositely charged tracks were identified [85]. This required that the closest distance of approach be within a certain distance (defined differently for each region) and that the vertex position be far away from the target edge. Then the invariant mass of the two tracks was calculated for the decay hypotheses $\Lambda \rightarrow \pi^-\mathrm{p}$, $\bar{\Lambda} \rightarrow \pi^+\bar{\mathrm{p}}$, and $\mathrm{K}^0 \rightarrow \pi^+\pi^-$. If the invariant mass agreed with the standard value [5] of the Λ within 5 MeV/c^2, the vertex was assumed to be the Λ decay vertex. Other cuts, some redundant as crosschecks, were made on the tracking information to find the positive tracks corresponding to the protons. The decay should occur before the spectrometer, producing the proton track which is bridged between the Λ-chambers and the spectrometer. The proton track was required

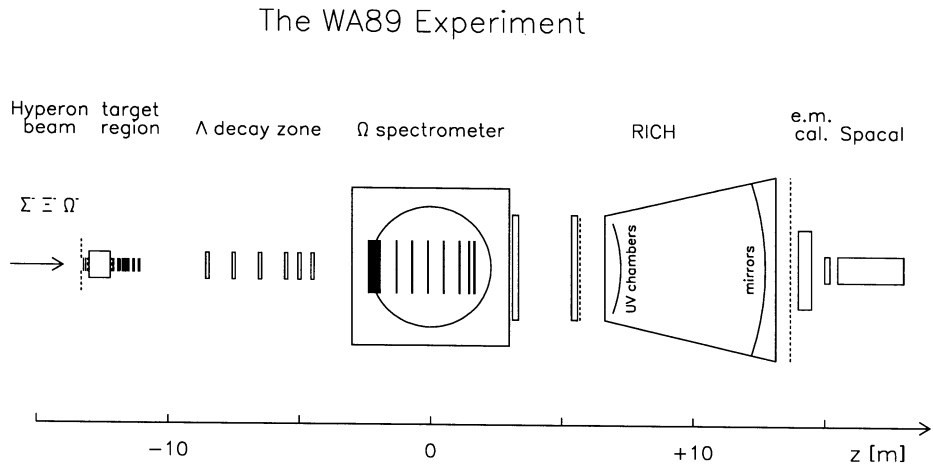

Figure 5.18: *Top view of the 1991 configuration of WA89, drawn to scale in the z-direction, the direction of the beam.*

to be well-defined and have a positive charge, as determined by the bending direction in the magnet. The ring in the RICH corresponding to the track should identify the particle as a proton [73]. This identification requires that the proton hypothesis be more probable by at least a factor 1 than any other hypothesis. This probability is given by the ratio of the likelihood values $\mathcal{L}_i$, *i.e.*,

$$\frac{\mathcal{L}_p}{\mathcal{L}_j} > 1.0, \tag{5.17}$$

for $j = \pi$, K, or background. The expected impact point of the particle on the SPACAL should be located within a radius of 40 cm from the center of SPACAL. This point was found by using the coordinates of the last point on the track (typically at $z = 5.6$ m) and the slope of the track to extrapolate out to the position of the SPACAL along the beam direction ($z = 17.52$ m).

Finally the shower in SPACAL corresponding to this track was determined in the following way. All of the local maxima, defined by a large energy deposit above 5 GeV surrounded by lower energy deposit, were found. Events were required to have at least one local maximum. For each shower, the barycenter was found using the energy deposit in the surrounding two rings, according to the method described in sect. 4.3.3. Looping over these maxima, the following cuts were made:

i. The tower containing the barycenter had to have 2 full rings surrounding it in the acceptance of the calorimeter. The sum of the signals in these 19 towers was called the particle energy (still to be calibrated). This minimizes the overlap between showers and makes the average fraction of energy contained the same at the same energy.

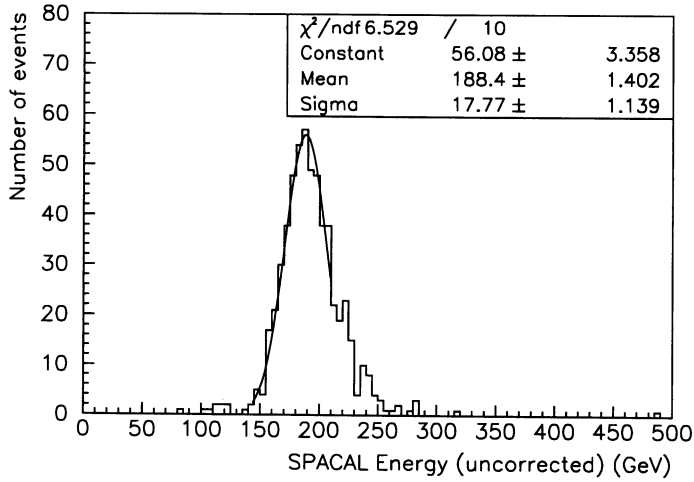

Figure 5.19: *The uncorrected energy of the protons measured within two rings of SPACAL towers within an energy interval of 184-186 GeV, with a Gaussian fit over the range $[-2\sigma, +1\sigma]$ around the peak. The mean value is taken to be the SPACAL uncorrected energy of 188.4 GeV for the energy of 185 GeV.*

ii. Showers with barycenters within 16 cm of each other (roughly the distance across two towers) were rejected. The remaining, "isolated" showers avoid inaccurate energy measurements due to overlapping energy deposit.

iii. The barycenter closest to the calculated impact point of the extrapolated track was chosen, with the distance between them not more than 3.3 cm.

The resulting proton sample amounted to almost 60,000 events.

In order to check the accuracy of the energy measurement and to find a correction if necessary, we had to find the best expression relating the energy E_{uncorr} measured by SPACAL (with only the electron calibration constants) with the energy E derived from the spectrometer momentum measurement. The events were divided into intervals of 2 GeV over the range from 44 GeV to 282 GeV (according to the spectrometer measurement). The SPACAL signal (the sum of 19 towers) for the events in each interval was plotted and a Gaussian fit made over the range $[-2\sigma, +1\sigma]$ around the peak, as in the example in fig. 5.19. This excludes a tail on the high-energy side, which is especially prominent at higher energies due to the attenuation effects (sect. 4.4.2). The mean of this fit was taken to be the calorimeter measurement corresponding to the energy at the center of the interval, *i.e.*, for the interval between 100 and 102 GeV, the energy for the interval is 101 GeV. The uncertainty is given by the error on the mean value. The calorimeter energy was then plotted as a function of the known energy in fig. 5.20.

The SPACAL energy deviates from the correct energy, especially at the low and

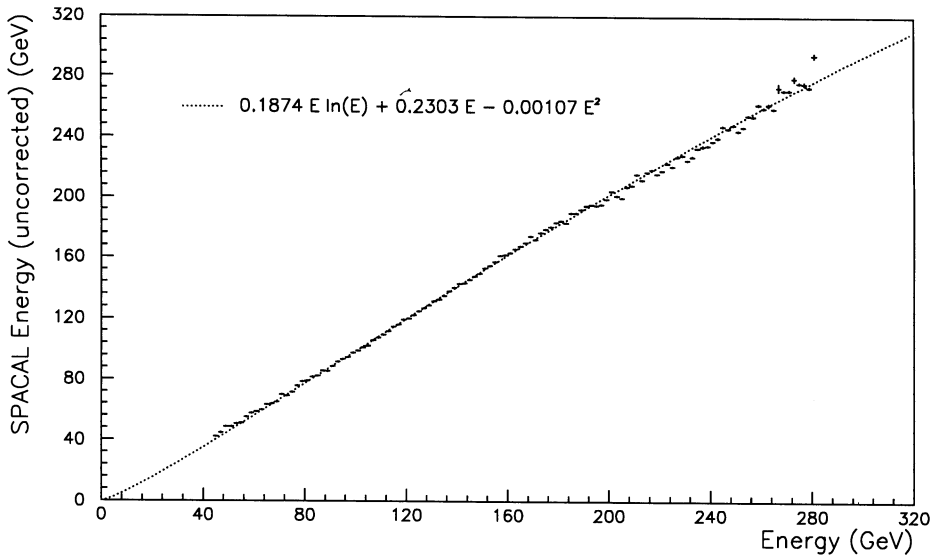

Figure 5.20: *The calorimeter energy (within 2 rings of towers) before hadron energy correction versus the energy from the spectrometer momentum measurement, for protons. The errors are based only on statistical considerations. The curve is the best fit to the data.*

high values. In order to find the expression relating the two values, a fit was made to the data in fig. 5.20 using various functions. The expression that best describes the data was found to be

$$E_{\text{uncorr}} = K_1 E \ln(E/E_0) + K_2 E + K_3 E^2, \tag{5.18}$$

where E is in units of GeV. K_1, K_2, and K_3 are constants and $E_0 = 1$ GeV is a normalization term for the units. This equation describes the data better than a straight-line and second- and third-degree polynomials. The resulting curve is also plotted on fig. 5.20, where the parameters are

$$\begin{aligned} K_1 &= 0.1874 \pm 2.76 \times 10^{-4}, \\ K_2 &= 0.2303 \pm 1.09 \times 10^{-3}, \\ K_3 &= -0.00107 \pm 3.07 \times 10^{-6}\ \text{GeV}^{-1}. \end{aligned}$$

The energy correction is only accurate up to 290 GeV, since the extrapolation of the curve past the range of data is not necessarily valid.

The expression used for the correction (eq. 5.18) can be understood by looking at possible sources of deviation from an accurate measurement of the particle energy in SPACAL:

i. Only 19 towers are used for the hadron energy measurement, resulting in an underestimation of the energy. The average fraction $\langle f_{\text{cont}} \rangle$ of energy contained in this volume is also energy-dependent. For radii far from the e.m. core of the shower, it may be described by the parametrization [61]

$$\langle f_{\text{cont}} \rangle = 1 - \frac{C(1 - \langle f_{\text{e.m.}} \rangle)}{(e/h - 1)\langle f_{\text{e.m.}} \rangle + 1}, \tag{5.19}$$

where C is a multiplicative constant and $\langle f_{\text{e.m.}} \rangle$ is the average fraction of energy in the e.m. component of the hadronic shower. Using logarithmic expression for $\langle f_{\text{e.m.}} \rangle$ (eq. 2.14) and the previously measured value $e/h = 1.15$ (sect. 4.4.4), $\langle f_{\text{cont}} \rangle$ approximately follows the form

$$\langle f_{\text{cont}} \rangle \propto \ln E. \tag{5.20}$$

Therefore, the uncorrected calorimeter measurement E_{uncorr} is this fraction of the actual energy E:

$$\begin{aligned} E_{\text{uncorr}} &= E\langle f_{\text{cont}} \rangle \\ &\propto E \ln E. \end{aligned} \tag{5.21}$$

ii. The calibration constants were derived from the test beam data, which consisted of electrons. As previously determined (sect. 4.4.4), the SPACAL is not compensating, with $e/h = 1.15$. Therefore, a correction needs to be made for $e/\pi \neq 1$, as a function of energy. The relationship between the calorimeter signal (with the electron calibration constants applied) E_{uncorr} and the actual energy E is

$$E_{\text{uncorr}} = \frac{E}{(e/\pi)}. \tag{5.22}$$

Using eqs. 2.13 and 2.14, this can be written as a function of energy only:

$$E_{\text{uncorr}} \propto E(0.015 \ln E + 1). \tag{5.23}$$

iii. Electrons of only up to 50 GeV were used for the calibration, and this range may have not been enough for an accurate determination of the energy scaling up to the hyperon beam energy of 330 GeV.

iv. The e/π signal ratio may differ from e/p ($\approx e/n$) due to the difference in the pion and proton interaction lengths, where $\lambda_\pi = 1.5\lambda_I$ [12]. A baryon shower will, on average begin to shower earlier, resulting in a more attenuated signal. The correct energy value should then differ from the calorimeter value, already corrected for e/π, by a constant factor K:

$$E_{\text{uncorr}} = KE \tag{5.24}$$

By combining the known deviations from an accurate hadronic energy measurement in the calorimeter with a quadratic term (perhaps to account for uncorrelated non-linearities), the resulting relationship may be parametrized by eq. 5.18.

The difference between the corrected SPACAL energy measurement and the Omega value as a fraction of energy is plotted in fig. 5.21*a* for events with energy < 290 GeV. The distribution peaks at 0, since the correction forces agreement, on average, between the two measurements. This fractional difference shows no dependence on energy, as shown in fig. 5.21*b*.

The corrections needed to bring the SPACAL energy measurements into agreement with the measured momenta of the protons are surprisingly small. For 99% of the events, the corrected energy E varies by no more than 6 GeV with the uncorrected value E_{uncorr}, taken from the sum over 19 towers. According to fig. 4.22, this cluster, with an effective radius of 20.5 cm, contains only an average of $\sim$90% of the total energy deposit of high-energy hadron shower. Since the (uncorrected) e/π signal ratios are very close to unity at these energies (fig. 4.33), the small residual non-compensation is not a factor in this apparent discrepancy. Most likely, the considerable pile-up effects, which increase the signals, are responsible for this phenomenon. The spread in the energy residual (fig. 5.21) also includes the effects of light attenuation in the fibers, the calorimeter energy resolution (eq. 4.12, 4.13) and the momentum resolution of the spectrometer (eq. 5.2), as well as some other external factors that can not be removed or corrected for, listed below.

- Large uncertainties in the rate corrections contribute to a broadening of the energy measurement (sect. 5.4.1).

- The energy correction as determined by the proton calibration has some uncertainty due to

  - variation in the containment, since the signal was integrated over two rings, but a particle could enter at any point on the tower;
  - many signals were enhanced by energy deposited by pile-up events within the gate width, as described above.

This last problem probably influenced the results the most. As a result, the energy resolution can not be meaningfully determined from this data.

Even when ignoring the pile-up effects on the signals, the calorimeter resolution in the hyperon beam is worse than the resolution as determined in the H2 beam tests (eq. 4.12, 4.13) for the following reasons:

- Longitudinal leakage is more likely to occur at these higher energies [59].

- With integration over only two rings, lateral leakage fluctuations contribute to the resolution (eq. 4.16), deteriorating it by $\sim$40% at high energy (see fig. 4.32*a*).

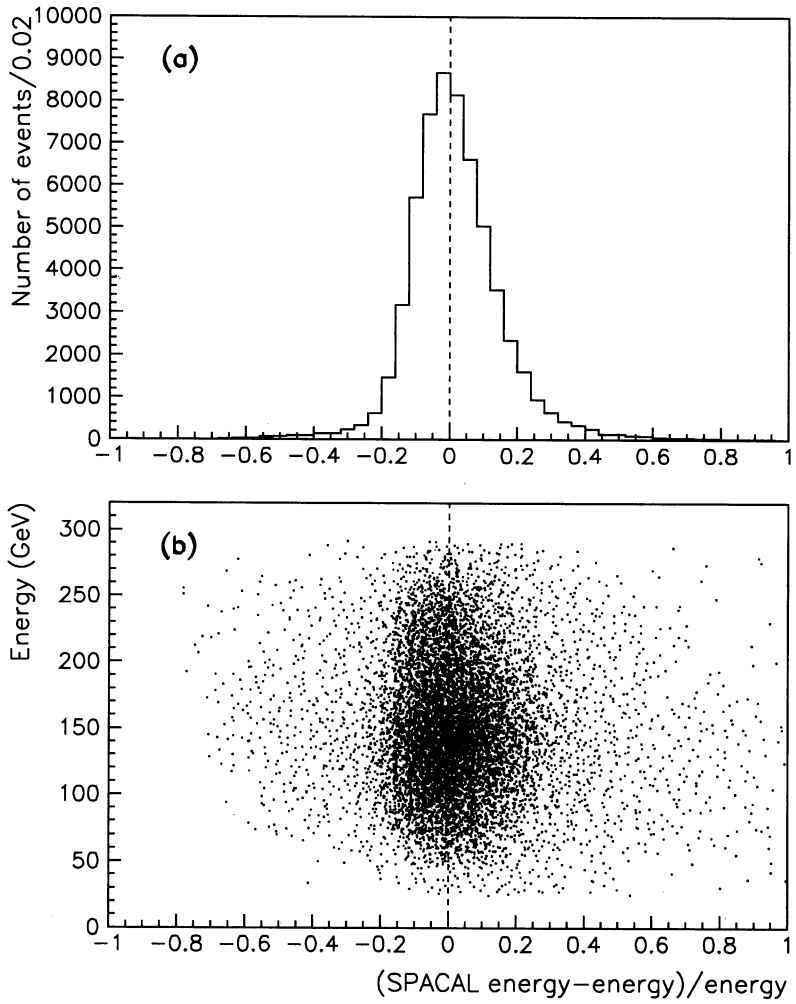

Figure 5.21: *(a) The difference between the energy of the protons as measured by the SPACAL and by the Omega spectrometer, normalized to the latter. (b) The known energy versus this energy difference, as in (a).*

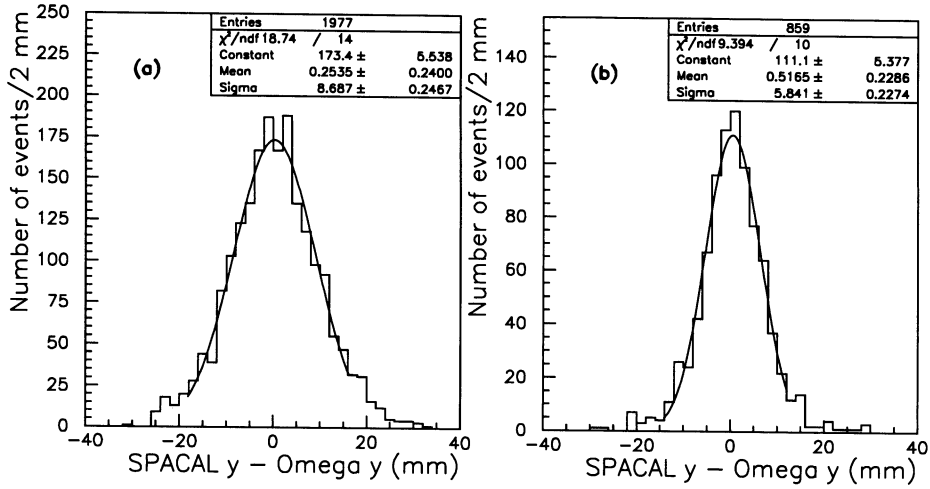

Figure 5.22: *The difference between the vertical positions of the proton barycenter in SPACAL and of the impact point extrapolated from track information for (a) the energy range [75,85] GeV and (b) [245,255] GeV. The Gaussian fits exclude the tails on the distribution.*

- There are overlapping showers, leading to more uncertainty in the energy measurement. This is probably a small effect: when the isolation cut is increased from 16 to 32 cm, the energy distributions remain practically the same.

For the reconstruction of the Σ^- particles, not only does the energy resolution of the detected neutron contribute to the mass resolution, but also the accuracy with which the position of the neutron is measured (sect. 5.4.3). Degradation of the energy resolution also has implications for this position resolution, since the position determination is based on the sharing of energy between towers. This is confirmed by the proton position measurement in SPACAL. The difference between the vertical position of the SPACAL barycenter and that of the impact point extrapolated from track information is plotted in fig. 5.22 for values between 75 and 85 GeV, and for those between 245 and 255 GeV. The vertical coordinate is not sensitive to the bending of the particle trajectory by Omega, so the angle with respect to the fiber direction is assumed to be 0°. This assumption is confirmed by the centering of the distributions close to 0. The resolution at 80 GeV is found to be 8.7 mm, as compared to the value of 5.1 mm found in the H2 test beam (sect. 4.4.1). The position resolution improves at higher energies (closer to the range of the neutron energies), down to 5.8 mm at 250 GeV.

5.4.3 Invariant mass reconstruction of Σ^-

With the hadron calorimeter, the neutron energy and position should be measured with good precision, in order to get a good resolution on the reconstruction of the Σ^-.

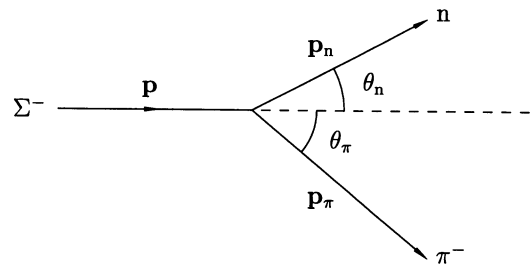

Figure 5.23: *Schematic of the decay of a Σ^- with momentum $\mathbf{p}$ into $n\pi^-$ with momenta $\mathbf{p}_n$ and $\mathbf{p}_\pi$ at angles θ_n and θ_π, respectively. The angles are not drawn to scale.*

The motivation for identifying $\Sigma^\pm \rightarrow n\pi^\pm$ was detailed in sect. 5.1.4. It should be emphasized that the identification and energy measurement of neutrons is not possible in WA89 without a hadron calorimeter.

The kinematics

The reconstruction is performed by taking the invariant mass of the pairs of candidates for the decay products, *i.e.*, the n and π^-. A straightforward way to check the calorimeter performance and usefulness in the experiment is to reconstruct a Σ^- from the beam (which does not interact in the target) by the decay $\Sigma^- \rightarrow n\pi^-$. Beam particles are easily identified by the rest of the experimental apparatus. With the measurement of the neutron energy and position by SPACAL, the pion momentum vector by the Omega spectrometer, and the Σ^- trajectory by the microstrip detectors, the mass of the Σ^- can be reconstructed and compared with the actual mass.

The expression for the invariant mass of a particle with two decay products, here for the $\Sigma^- \rightarrow n\pi^-$, can be derived as follows. Fig. 5.23 defines the variables, where on the left is the Σ^- particle, with mass M and 4-momentum $p = (E, \mathbf{p})$ where E is the energy and $\mathbf{p}$ is the momentum vector.[2] On the right are the resulting particles, with their respective momenta $\mathbf{p}_n$ and $\mathbf{p}_\pi$ and angles θ_n and θ_π with respect to the incoming trajectory. The square of the mass of the decaying particle is an invariant,

$$M^2 = p_\mu p^\mu = E^2 - \mathbf{p}^2, \tag{5.25}$$

and is treated as the unknown. The total energy of the system is conserved, so that

$$E = E_n + E_\pi. \tag{5.26}$$

The total momentum is also conserved, so that

$$\mathbf{p} = \mathbf{p}_n + \mathbf{p}_\pi. \tag{5.27}$$

[2] The convention $c = 1$ is used from here onwards.

Breaking down the momentum vector into components parallel and perpendicular to the initial particle direction yields

$$|\mathbf{p}| = |\mathbf{p}_n| \cos\theta_n + |\mathbf{p}_\pi| \cos\theta_\pi \quad (5.28)$$

$$0 = |\mathbf{p}_n| \sin\theta_n + |\mathbf{p}_\pi| \sin\theta_\pi, \quad (5.29)$$

where the angles θ_n and θ_π have opposite signs.

In WA89, the known values are the vectors of the beam track (the Σ^-) from the microstrip detectors, the momentum vector of the π^- from the Λ-chambers and the Omega spectrometer, and the energy deposit and barycenter position of the neutron in the SPACAL. The angle θ_n of the neutron with respect to the path of the Σ^- is found using the position of the neutron and the position of the decay vertex. The decay vertex is located at the position of the closest distance of approach of the Σ^- and π^- tracks. The pion angle θ_π with respect to the Σ^- trajectory is found by taking the dot product of these tracks. The Particle Data Group (PDG) values [5] for the neutron and pion masses are used.

The invariant mass for $n\pi^-$ pairs was calculated using either the energy or position information or both, in order to see the effects of the SPACAL energy and spatial resolution. This is possible since the kinematical calculation is overconstrained.

When the neutron energy E_n alone is used, with the neutron angle θ_n calculated using the information about the pion momentum. From eq. 5.29

$$\theta_n = \sin^{-1}\left(\frac{-|\mathbf{p}_\pi| \sin\theta_\pi}{|\mathbf{p}_n|}\right). \quad (5.30)$$

The momentum of the neutron then follows as $|\mathbf{p}_n| = \sqrt{E_n^2 - m_n^2}$). The total energy is thus

$$E = E_n + \sqrt{|\mathbf{p}_\pi|^2 + m_\pi^2}. \quad (5.31)$$

The momentum of the Σ^- can be expanded from eq. 5.28 as

$$|\mathbf{p}| = \sqrt{E_n^2 - m_n^2} \cos\theta_n + |\mathbf{p}_\pi| \cos\theta_\pi. \quad (5.32)$$

Putting these values into eq. 5.25 yields the invariant mass.

If only the neutron position in SPACAL is used, its momentum $|\mathbf{p}_n|$, and from that E_n, can be determined from eq. 5.29:

$$|\mathbf{p}_n| = \frac{-|\mathbf{p}_\pi| \sin\theta_\pi}{\sin\theta_n}. \quad (5.33)$$

When both the neutron energy and position measured by SPACAL are used, the total energy and momentum can be directly found from eqs. 5.26 and 5.28. The balance between the transverse components of the momenta (eq. 5.29) provides an extra constraint on the measured quantities. With a kinematic fit, these quantities

can be varied in order to best satisfy the constraint condition. This is done by setting up a least-squares function

$$S = \left(\frac{|\mathbf{p}_n| - |\mathbf{p}_{n,fit}|}{\sigma_{p_n}} \right)^2 + \left(\frac{\theta_n - \theta_{n,fit}}{\sigma_{\theta_n}} \right)^2, \tag{5.34}$$

where the new values are $|\mathbf{p}_{n,fit}|$ and $\theta_{n,fit}$. The error σ_{p_n} is determined by the energy resolution of SPACAL (as determined for the simulation, described below). The error σ_{θ_n} on θ_n results from the position resolution of spacal. This function is minimized by the method of Lagrange multipliers, which incorporates the constraint equation to find a solution [86]. Only the neutron quantities are varied in this case, since the pion momentum vector is very well-measured. The new values $|\mathbf{p}_{n,fit}|$ and $\theta_{n,fit}$ are then put into the equations for total energy and momentum to calculate the invariant mass. The resulting value of S is distributed as χ^2 and gives the quality of the fit.

The results

The selection of decaying beam Σ^- candidates was first made by a series of cuts using the track and momentum information provided by the tracking detectors. Afterwards, events containing reliable information from the showers in SPACAL were selected. Then the invariant mass of the neutron candidate and the negative track was determined.

The following criteria identify an event as a beam Σ^- decay candidate. The event is required to consist of one well-defined beam track decaying after the microstrips into one negative track, with a kink angle (θ_π) larger than 1 mrad. The momentum of this pion candidate should be less than 270 GeV/c to remove undecayed beam particles. As a loose cut before the SPACAL information is used, the invariant mass, calculated using the above information and assuming the beam energy to be constant at 330 GeV, is within 70 MeV of the PDG value for the Σ^-.

The following calorimeter cuts define an event as a decaying Σ^- for the final results:

i. The calorimeter contains one or two maxima, corresponding to the neutron shower and possibly the pion shower if it is within the acceptance.

ii. The shower with the highest energy deposit is taken to be the neutron.

iii. The barycenter of this shower has two complete rings of towers around it. As with the protons, the energy is defined by the sum of the deposits in the tower containing the barycenter and in the surrounding two rings, with the hadronic energy correction applied (sect. 5.4.2).

iv. The energy of the shower is less than 290 GeV, the limit of the energies of the available protons and thus of the proton energy correction.

v. Poor neutron energy values calculated according to eq. 5.33 are removed by requiring that it agree within 50% with the energy as measured in SPACAL.

vi. Badly measured neutron angles are rejected by requiring that $\theta_n/\theta_\pi < 0.5$.

If the event is selected by all these criteria, the invariant mass is calculated. The resulting distributions are plotted in fig. 5.24 as the difference between the invariant mass and the standard mass value of 1197.43 MeV/c^2 from the PDG [5]. The σ of a Gaussian fit, performed over the entire range, is the mass resolution. For the calculation using the SPACAL energy measurement but not the position information (fig. 5.24*a*), it is found that the invariant mass peak is shifted by 3.3 MeV/c^2 from the PDG value, with a resolution of 10.94 MeV/c^2. The distribution broadens to a width of 16.09 MeV/c^2 (fig. 5.24*b*) when the neutron angle is derived from the neutron's position in SPACAL, but the neutron energy measured by SPACAL is not used. The tails on the distributions are not due to background, which is absent without interactions, but rather due to poor determination of the neutron energy by eq. 5.33, especially at low energies. When both the SPACAL energy and barycenter measurements are used, but not constrained by eq. 5.29, the Σ^- invariant mass resolution improves somewhat (fig. 5.24*c*). When the neutron momentum vector, determined from the SPACAL energy and barycenter measurements, is modified by the constrained kinematic fit, the best invariant mass resolution is found at 10.75 MeV/c^2 for the distribution in fig. 5.24*d*. The neutron momentum and angle ($|\mathbf{p}_{n,fit}|$ and $\theta_{n,fit}$) are very close to the values found using the SPACAL energy measurement alone. Therefore, the error on the neutron angle θ_n is too large to make the constraint more useful for the invariant mass width. The SPACAL neutron measurement, however, is still useful for removing background events to this decay, for Σ^-s both from the beam and from interactions. A cut on the χ^2 of the fit does not change the results considerably.

Monte Carlo simulation

In order to understand the relative importance of the uncertainties contributing to the mass resolution, especially of the SPACAL position measurement, a simple Monte Carlo simulation was made. No detailed detector information was simulated. The following resolutions were included, to smear the values used in the invariant mass calculation:

- The beam Σ^- momentum spread was taken to be 12% around the nominal value of 330 GeV/c.
- The pion momentum resolution as measured by the spectrometer was included as eq. 5.2.
- The resolution on the pion angle θ_π was based on the uncertainties on the track position and slope from the data and parametrized as a function of the angle.
- The SPACAL energy resolution was given by eq. 4.16, with values for C_1 and C_2 taken from eq. 4.12 and a leakage fraction of 14%, as seen in fig. 4.22.
- The SPACAL nominal position resolution (eq. 4.8) was used.

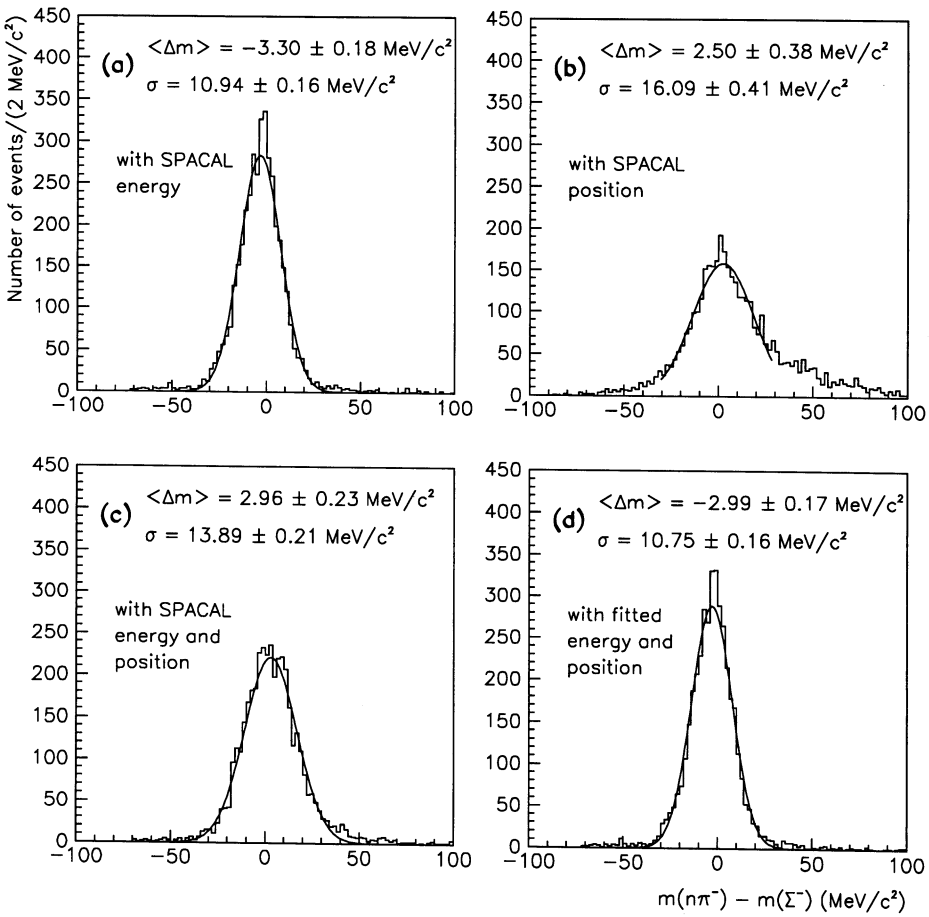

Figure 5.24: *The invariant mass of the non-interacting Σ^- calculated with the information from the decay into a neutron and π^- using SPACAL information, plotted as the difference from the PDG value [5]. The curve is the fit over the Gaussian part of the distribution. In (a), the only information from SPACAL used is the neutron energy; in (b), only the barycenter of the neutron in SPACAL is used; in (c), both the neutron energy and barycenter are used, but the constraint is not used; and in (d), the neutron momentum vector, derived from the SPACAL energy and barycenter measurements, is varied by the constrained kinematic fit and used in the invariant mass calculation.*

The same cuts were made to the simulated events as to the real data.

With these uncertainties, the invariant mass distributions in fig. 5.24 were roughly reproduced. The simulation shows that for the first mass distribution (fig. 5.24*a*), the width is dominated by the error on θ_π rather than the SPACAL energy resolution. However, for the mass distribution where θ_n is found using the vertex and neutron position in SPACAL (fig. 5.24*b*), the position resolution dominates. The resolution on θ_n is 0.12 ± 0.001 mrad, somewhat worse than the resolution of 0.08 ± 0.001 mrad on the angle found using the SPACAL energy measurement and the pion momentum vector (eq. 5.30). (The average value of θ_n is 0.7 mrad.) Therefore, the position resolution contributes much more to the invariant mass resolution than the energy resolution of SPACAL. The improvement of the mass resolution by the constrained kinematic fit was also reproduced in the simulation. When the uncertainty on the neutron position is reduced, the improvement of the mass resolution is even greater.

In the next section, I discuss how the SPACAL system can be improved in order to improve the mass resolution, and I give a summary of what was learned in the 1991 test beam and experimental running periods.

5.4.4 Discussion and outlook

The reconstruction of beam Σ^- particles using the SPACAL to measure the decay neutron energy and position has been successfully done for beam particles in WA89, with a best resolution of 10.75 MeV/c^2, achieved using a constrained kinematic fit. This is only slightly better than the mass resolution found using only the neutron energy measurement. Without the constraint, the mass resolution worsens to 13.89 MeV/c^2, as a result of the resolution on the neutron angle. The data from this experimental run was also processed to look for the Σ^- from the decay of particles produced in interactions in the target. The distribution of the $n\pi^-$ invariant mass in fig. 5.25, calculated using both the SPACAL energy and position measurements without a constrained fit, has a width of 12.6 MeV/c^2 [87]. This is perhaps a little better than for the beam Σ^- because the opening angles are larger, with less uncertainty. The peak is shifted by only 0.3 MeV/c^2 from the PDG Σ^- mass value, but with a combinatorial background that is not present for the beam particles (fig. 5.24). The signal-to-noise ratio, however, is good at 2.35.

Such a measurement in WA89 is not possible without a hadronic calorimeter, which extends the capabilities of the experiment. The SPACAL detector was not designed for this purpose, but works well for this measurement, as its performance in the 1991 run shows. The neutron energy measurement provided a reliable Σ^- identification by the invariant mass calculation. A better position determination would improve the mass resolution even more, as shown by Monte Carlo simulation.

The fibers showed no sign of radiation damage after 10-100 krad in the most vulnerable tower from $2\frac{1}{2}$ weeks in the high-rate beam (sect. 5.4.1). The relatively small acceptance of the SPACAL was sufficient for the detection of high-energy neutrons from Σ^- decay, since these neutrons are localized near the undeflected beam axis.

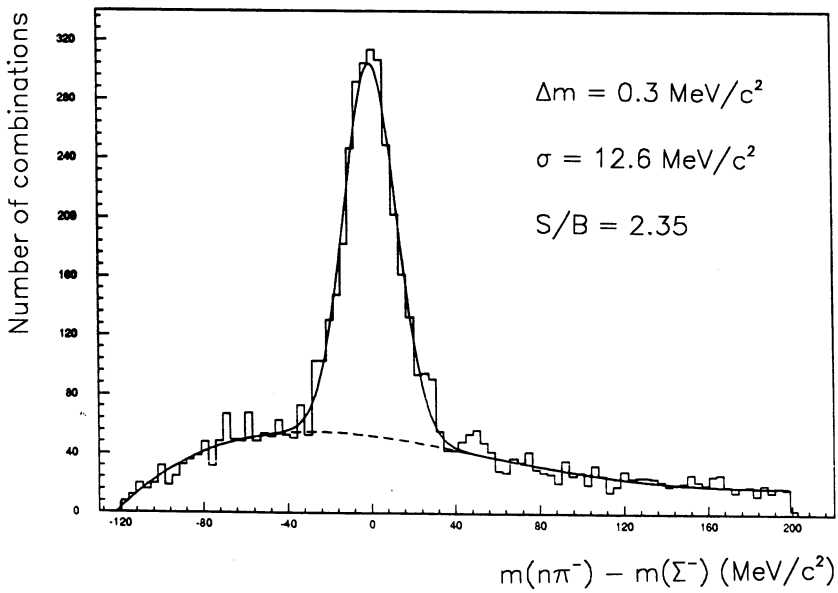

Figure 5.25: *The invariant mass of $n\pi^-$, plotted as the difference from the PDG value of the Σ^- mass, produced from interactions in the target [87].*

Running the SPACAL system under experimental conditions was found to be more difficult than in the test beams, but most of the problems were solvable. The biggest challenges were encountered with the readout and monitoring (sect. 5.4.1), not with the calorimeter itself. The high rates in the experiment required the modification of the PM bases and good cooling. The PM gain over the long-term was found to decrease, with aging of the dynodes the suspected cause. The most harmful effect was the change in signal caused by pile-up, which increased with the particle rate within a spill. Good monitoring of the readout chain helped to offset the effects of the aging of the PMs and temperature variations quite well, and to a lesser degree, the pile-up. This and an inaccurate determination of the pedestals were the limiting factors to an accurate energy measurement. Despite these problems, the Σ^- can be well-reconstructed (fig. 5.24) with good separation of the signal from background (fig. 5.25).

Improvements relating to the neutron measurement itself would also improve the Σ^- decay reconstruction. The shower position measurement could be improved by a better correction to the center-of-gravity value (fig. 4.25). It is not clear, however, that it can be improved by much, since there is a large spread in values due to the intrinsic shower size fluctuations. The barycenter measurement may also be improved by a more accurate measurement of the energy deposit, which would also improve the invariant mass resolution. A better energy resolution could be achieved by a hadron energy calibration extending above 290 GeV (sect. 5.4.2), covering an energy range

of many neutrons resulting from Σ^- decay. More study on tower clustering is also needed. A hadron calibration based on the energy deposits in individual towers could be made so that a cluster containing more than 19 towers could provide the energy measurement, provided the shower is isolated enough. With isolation cuts, such as the ones used in the analyses presented here, some energy information is still not used. The energy of two overlapping showers could be measured together then separated, based on knowledge of the shower profiles and the momentum of charged particles as measured by the spectrometer. In addition, a determination of the hadronic energy resolution in the test beam with the improved readout system would help to determine the factors contributing to the invariant mass resolution.

Some results of the trial run of SPACAL in WA89 were not presented here. It was found that the $\sim 1\lambda_I$ deep e.m. calorimeter placed in front of the SPACAL, for part of the time, did not greatly degrade the neutron measurement [84]. The invariant mass reconstruction was possible, with less noise from photons showering in the calorimeter. It was decided then to keep the e.m. calorimeter in later configurations, as it has the capability of simple and effective e–π separation, in addition to filtering electrons and photons.

In addition to providing information about a neutron's energy and position in off-line analysis, the calorimeter should quickly identify neutrons as a possible final state of an interesting decay for trigger purposes. Normally, hadron identification is based on lateral energy distribution and sharing: hadron showers have a broader lateral profile. Gathering and processing this information, however, is too slow for the trigger, motivating different approaches to identification. First, the particle needs to be identified as a hadron. The method of e–π separation by measuring the width of the analog signal pulse at 20% of the amplitude ("full-width-at-a-fifth-maximum," sect. 4.5.2) was tested for use in WA89 using specially designed electronics [75]. The circuit worked well using the 7 central towers in the test beam [75], but connecting all analog signals for hits anywhere on the surface of the calorimeter in the experiment was thought to be too unwieldy in practice. A trigger processor for e–π discrimination based on the differences between lateral shower dimensions will be used instead. The second function of a neutron trigger is to reject charged particles. A scintillating-tile hodoscope covering the front surface of the calorimeter is to be used to detect charged particles [88]. This minimum-ionizing signal provides a neutron veto when correlated to a hadronic shower in the calorimeter. The hodoscope consists of 155 hexagonal tiles, each the same size as a SPACAL tower. Five wavelength-shifting fibers glued into grooves on the tile transport the scintillation light to a small PM, each arranged on a support around the tiles. The full detector was not completed before the runs discussed here, but smaller versions covering a smaller area of the calorimeter were tested [75, 88]. This partially built hodoscope worked satisfactorily when the signals from showers starting in the e.m. calorimeter and from albedo particles from SPACAL were understood and the appropriate algorithms devised [88].

Modifications to the calorimeter system, in addition to the debugging of the system and the experience gained during the previous runs, improved the overall performance

in the recent calibration test beam and experimental run in 1993. The SPACAL was calibrated before and after the run in the X3 test beam, and was placed in the experiment after the e.m. calorimeter for most of the 2 month run. The biggest improvement was the elimination of event pile-up within the calorimeter gate, which distorts the energy measurement, as described in sect. 5.4.1. This was the reason for the rate-dependent effects observed in the 1991 data. The pedestals were also determined in another way. The pedestal values were recorded on-line in the form of histograms for each run, so that off-line processing required only taking the peak of a Gaussian fit as the final pedestal value. In this way, anomalous pedestal signals are left out, and it is not necessary to process all the pedestal data before doing analysis. It solved the problem of non-zero signals in towers far from an e.m. shower, and thus reduced fluctuations in the signal. The test beam set-up was automated, making the electron calibration of the calorimeter possible at five energies for both the high and low ADC range in less than two weeks. An improved support control system aided the process greatly by providing reliable service and position measurements. From the test beam data, the calorimeter electron signal was found to be linear between 10 and 50 GeV. Finally, the neutron trigger was tested. It consisted of four requirements, all but the last programmed into a digital signal processor (DSP) for this run:

i. The sum of the 91 inner towers was more than 30 GeV.

ii. At least two charged particles resulted from the interaction.

iii. No second particle entered within 150 ns before or after the beam trigger, as described above.

iv. No signal was observed in the scintillating tiles corresponding to the towers containing the bulk of the shower. These towers were determined by calculating the center of gravity of the shower based on the number of towers above 10 GeV. This was tested only by a software version.

The trigger worked well on-line, with a full analysis to be done later.

Therefore, some interesting particles should be studied with the 1993 data, not to be limited by statistics or instrumental problems as in 1991. The energy and position of neutrons should be measured with better accuracy and resolution, providing a better identification and momentum measurement of the $\Sigma^{\pm}$. The running of the SPACAL has improved by profiting from what was learned in the beam tests and WA89 run in 1991 and in the research and development program earlier. However, the SPACAL detector performed well even in 1991 for the reconstruction of $\Sigma^- \rightarrow n\pi^-$, as shown in the last sections, and the contributions of the measurement uncertainties to the invariant mass were understood.

Bibliography

[1] Y.S. Tsai, *Rev. Mod. Phys.* **46** (1974) 815.

[2] W.R. Leo, *Techniques for Nuclear and Particle Physics Experiments* (Springer-Verlag, Berlin, 1987).

[3] H. Enge, *Introduction to Nuclear Physics* (Addison-Wesley, Reading, MA, 1966).

[4] B. Rossi, *High-Energy Particles* (Prentice Hall, Englewood Cliffs, NJ, 1952).

[5] Particle Data Group, "Review of particle properties," *Phys. Rev.* **D45** (1992).

[6] R. Wigmans, "Calorimetry in high energy physics," *Techniques and Concepts of High-Energy Physics VI*, ed. T. Ferbel, (Plenum, New York, 1991) 325.

[7] R. Wigmans, "Energy loss of particles in dense matter calorimetry," *Proc. of the ICFA School on Instrumentation in Elementary Particle Physics* (Trieste, June 1987), ed. C.W. Fabjan and J.E. Pilcher, (World Scientific, Singapore, 1988) 41.

[8] U. Amaldi, *Physica Scripta* **23** (1981) 409.

[9] W.R. Nelson, H. Hirayama and D.W.O. Rogers, SLAC 265 (1985).

[10] T. Yuda, *Nucl. Instr. and Meth.* **73** (1969) 301.

[11] R. Wigmans, *Nucl. Instr. and Meth.* **A259** (1987) 389.

[12] The *nuclear interaction length* λ_I is defined here in the same way in ref. [5], page III.5, 6. It is the mean free path for protons between inelastic interactions. Since the inelastic cross sections for protons are 50% larger than for pions, $\lambda_\pi \approx 1.5\lambda_I$.

[13] M.J. Berger and S.M. Seltzer, "Tables of energy losses and ranges of electrons and positrons," NASA SP-3012 (1964).

[14] C.W. Fabjan, "Calorimetry in high-energy physics," *Experimental techniques in high-energy nuclear and particle physics*, 2nd ed., ed. T. Ferbel, (World Scientific, Singapore, 1991) 257.

[15] E. Bernardi, "On the Optimization of the Energy Resolution of Hadron Calorimeters," DESY F1-87-01 (1987).

[16] M.G. Catanesi *et. al.*, *Nucl. Instr. and Meth.* **A260** (1987) 43.

[17] F. Barreiro *et. al.*, *Nucl. Instr. and Meth.* **A292** (1990) 259.

[18] R. Wigmans, *Nucl. Instr. and Meth.* **A265** (1988) 273.

[19] H. Brückmann, B. Anders and U. Behrens, *Nucl. Instr. and Meth.* **A263** (1988) 136.

[20] C.W. Fabjan and T. Ludlam, *Ann. Rev. Nucl. Part. Sci.* **32** (1982) 335.

[21] D. Groom, "Energy scaling of low-energy neutron yield, the e/π ratio, and hadron response in a calorimeter," *Proc. of the Workshop on Calorimetry for the Superconducting Supercollider* (Tuscaloosa, Alabama, 1989), ed. R. Donaldson and M. Gilchriese, (World Scientific, Singapore, 1990) 59.

[22] R. Wigmans, "Performance and limitations of hadron calorimeters," *Proc. of the 2nd International Conference on Calorimetry in High Energy Physics* (Capri, Italy, 1991), ed. A. Ereditato, (World Scientific, Singapore, 1992) 24.

[23] C.W. Fabjan *et. al.*, *Nucl. Instr. and Meth.* **141** (1977) 61.

[24] G. Drews *et. al.*, *Nucl. Instr. and Meth.* **A290** (1990) 335.

[25] G.R. Young *et. al.*, *Nucl. Instr. and Meth.* **A279** (1989) 503.

[26] D.E. Groom, "Four-component approximation to calorimeter resolution," *Proc. of the 2nd International Conference on Calorimetry in High Energy Physics* (Capri, Italy, 1991), ed. A. Ereditato, (World Scientific, Singapore, 1992) 376.

[27] T. Åkesson *et. al.*, *Nucl. Instr. and Meth.* **A241** (1985) 17.

[28] H. Brückmann, "On the theoretical understanding and calculation of sampling calorimeters," DESY 87-064 (1987).

[29] J.E. Brau and T.A. Gabriel, *Nucl. Instr. and Meth.* **A279** (1989) 40.

[30] J.E. Brau and T.A. Gabriel, *Nucl. Instr. and Meth.* **A238** (1985) 489.

[31] H. Gordon and P. Grannis, "Calorimetry for the SSC," *Proc. of the 1984 Summer Study on the Design and Utilization of the SSC* (Snowmass, Colorado, 1984) ed. R. Donaldson and J.G. Morfín, 541.

[32] E. Bernardi *et. al.*, *Nucl. Instr. and Meth.* **A262** (1987) 229.

[33] T. Åkesson *et. al.*, *Nucl. Instr. and Meth.* **A262** (1987) 243.

[34] G. D'Agostini *et. al.*, *Nucl. Instr. and Meth.* **A274** (1989) 134.

[35] R. Wigmans, "Lead/scintillating-fibre calorimetry," *Proc. of the Workshop on Calorimetry for the Superconducting Supercollider* (Tuscaloosa, Alabama, 1989), ed. R. Donaldson and M. Gilchriese, (World Scientific, Singapore, 1990) 345.

[36] P. Jenni *et. al.*, "The high resolution spaghetti hadron calorimeter," NIKHEF-H/87-7 (1987).

[37] J. Kirkby, "Today and tomorrow for scintillating fibre (SCIFI) detectors," *Vertex detectors: Proc. of the INFN Eloisatron Project Workshop on Vertex Detectors,* (Erice, Italy, 1986) ed. F. Villa, (Plenum, New York, 1988) 225.

[38] A. Simon, "Scintillating fibre detectors in particle physics," CERN-PPE/92-95 (1992). Also *Proc. of the Photon Club Workshop* (Edinburgh, May 1991) 140.

[39] J.B. Birks, *Theory and Practice of Scintillation Counting* (Pergammon, Oxford, 1964).

[40] Kuraray Co., Ltd., Tokyo, Japan, private communication.

[41] N.A. Amos *et. al.*, *Nucl. Instr. and Meth.* **A297** (1990) 396.

[42] C.M. Hawkes *et. al.*, *Nucl. Instr. and Meth.* **A292** (1990) 329.

[43] D. Perrin and P. Sonderegger, "Electromagnetic calorimeter with scintillating optical fibers," CERN-OM-SPS/81-7.
H. Burmeister *et. al.*, *Nucl. Instr. and Meth.* **A225** (1984) 530.
P. Sonderegger, *Nucl. Instr. and Meth.* **A257** (1987) 523.
C. Baglin *et. al.*, *Phys. Lett.* **B220** (1989) 471.
H. Blumenfeld *et. al.*, *Nucl. Instr. and Meth.* **A225** (1984) 518.
A. Klovning, "Small angle tagger (SAT) for Delphi/LEP," *Proc. of the Workshop on Scintillating Fiber Detector Development for the SSC* (Fermilab, Batavia, IL, USA, November 1988) 415.
F. Takasaki *et. al.*, "Performance of a lead scintillation fiber calorimeter designed as an active shield for the VENUS detector," KEK 91-58 (1991).
D.W. Hertzog *et. al.*, *Nucl. Instr. and Meth.* **A294** (1990) 446.

[44] D. Babusci *et. al.*, *Nucl. Instr. and Meth.* **A332** (1993) 444.

[45] J. Badier *et. al.*, *Nucl. Instr. and Meth.* **A337** (1994) 326.

[46] A. Para *et. al.*, "An investigation of the effects of glue on light transmission in scintillating fibers," FERMILAB Pub 91-329 (1991).

[47] F.G. Hartjes and R. Wigmans, *Nucl. Instr. and Meth.* **A277** (1989) 379.

[48] D. Acosta, "Consequences of an attenuation length to the hadronic performance of a fiber calorimeter," SPACAL internal note.

[49] D. Acosta *et. al.*, "Results of prototype studies for a spaghetti calorimeter," *Nucl. Instr. and Meth.* **A294** (1990) 193.

[50] D. Acosta *et. al.*, "Effects of radiation damage on scintillating fibre calorimetry," *Nucl. Instr. and Meth.* **B62** (1991) 116.

[51] G.R. Stevenson, "New dose calculations for LHC detectors," *Proc. of the ECFA Large Hadron Collider Workshop, vol. III* (Aachen, Germany, October 1990) ed. G. Jarlskog and D. Rein, CERN 90-10 (1990) 566.

[52] A. Ferrari *et. al.*, "Can we predict radiation levels in calorimeters?" *Proc. of the 2nd International Conference on Calorimetry in High Energy Physics* (Capri, Italy, 1991), ed. A. Ereditato, (World Scientific, Singapore, 1992) 101.

[53] G. Anzivino *et. al.*, *Radiat. Phys. Chem.* **41** (1993) 283.

[54] K.F. Johnson *et. al.*, *Nucl. Instr. and Meth.* **A317** (1992) 502.

[55] R. DeSalvo *et. al.*, "A novel way of electron identification in calorimeters," *Nucl. Instr. and Meth.* **A279** (1989) 467.

[56] D. Acosta *et. al.*, "Electron-pion discrimination with a scintillating fiber calorimeter," *Nucl. Instr. and Meth.* **A302** (1991) 36.

[57] D. Acosta *et. al.*, "Localizing particles showering in a spaghetti calorimeter," *Nucl. Instr. and Meth.* **A305** (1991) 55.

[58] D. Acosta *et. al.*, "Electron, pion and multiparticle detection with a lead/scintillating-fiber calorimeter," *Nucl. Instr. and Meth.* **A308** (1991) 481.

[59] D. Acosta *et. al.*, "On muon production and other leakage aspects of pion absorption in a lead/scintillating-fiber calorimeter," *Nucl. Instr. and Meth.* **A309** (1991) 143.

[60] D. Acosta *et. al.*, "Performance of a lead/scintillating-fiber calorimeter at LHC/SSC compatible gate widths," *Nucl. Instr. and Meth.* **A314** (1992) 431.

[61] D. Acosta *et. al.*, "Lateral shower profiles in a lead/scintillating-fiber calorimeter," *Nucl. Instr. and Meth.* **A316** (1992) 184.

[62] D. Acosta *et. al.*, "Detection of muons with a lead/scintillating-fiber calorimeter," *Nucl. Instr. and Meth.* **A320** (1992) 128.

[63] A. Forino *et. al.*, "Proposal for a new hyperon beam experiment at the CERN-SPS using the Omega facility," CERN-SPSC/87-43/P-233 (1987).

[64] H.W. Siebert, *Nucl. Phys.* **B21** (Proc. Suppl.) (1991) 223, and references therein.

[65] S. Fleck and J.M. Richard, *Particle World* **1**:3 (1990) 67.

[66] J. Appel, *Ann. Rev. Nucl. Part. Sci.* **42** (1992) 367.

[67] M. Bourquin *et. al.*, *Phys. Lett.* **B172** (1986) 113.
H.W. Siebert, *Nucl. Phys.* **B21** (Proc. Suppl.) (1991) 183.

[68] S.M. Paul, *Inst. Phys. Conf. Ser.* No. 124 (1992) 159. (Contribution to the Workshop on Physics at SuperLEAR, Zurich, October 1991.)

[69] P. Grafström, "A Σ^-beam for the Omega spectrometer in the West Hall at CERN," CERN/SL/90-104 (EA) (1991). (Contribution to the 1990 Summer Study on High Energy Physics, Research Directions for the Decade, Snowmass, Colorado, June 1990.)

[70] S. Paul, "Particle identification using transition radiation detectors," CERN-PPE/91-199 (1991). Also *Proc. of the Photon Club Workshop* (Edinburgh, May 1991).

[71] A. Trombini, "Inclusive production of Ξ^* resonances in Σ^-C and Σ^-Cu interactions at 330 GeV/c," Ph.D. thesis, Universität Heidelberg (1992).

[72] W. Beusch *et. al.*, *Nucl. Instr. and Meth.* **A323** (1992) 373.

[73] U. Müller *et. al.*, *Nucl. Instr. and Meth.* **A343** (1994) 279.

[74] W. Brückner *et. al.*, *Nucl. Instr. and Meth.* **A313** (1992) 345.

[75] A. Simon, "Detecting and triggering on neutrons using the SPACAL Pb-Scintillating Fiber Calorimeter," *Proc. of the 2nd International Conference on Calorimetry in High Energy Physics* (Capri, Italy, 1991), ed. A. Ereditato, (World Scientific, Singapore, 1992) 157.

[76] WA89 Collaboration, "Use of a hadron calorimeter in WA89," CERN/SPSLC/91-9, SPSLC M-461 (1991).

[77] S. Barlag *et. al.*, *Phys. Lett.* **B233** (1989) 522.

[78] S. Paul, *Nucl. Phys.* **B21** (Proc. Suppl.) (1991) 243.

[79] K.-H. Brenzinger, "Das Monitorsystem für das hadronische Spaghetti Kalorimeter im Experiment WA89 am CERN," diploma thesis, Universität Heidelberg (1991).

[80] D.E. Plane, "The West Area beams," CERN/SPS/83-22 (1983).

[81] A. Manarin and G. Vismara, "The delay wire chamber (DWC) description," CERN/LEP/BI-TA/85-3 (1985).

[82] L. Poggioli, private communication.

[83] R. DeSalvo, private communication.
RCA Photomultiplier Manual (RCA Electronic Components, Harrison, NJ, 1970) 49-50.

[84] A. Simon, private communication.

[85] F. Dropmann and M. Godbersen, "The V0–Package in PHYNIX," WA89 internal note.

[86] L. Lyons, *Statistics for nuclear and particle physicists* (Cambridge University Press, Cambridge, 1986) 142-152.

[87] M. Beck, "Reconstruction of Σ^- final states with an hadronic spaghetti calorimeter," poster presented at the Spring Session of the DPG (German Physical Society), Mainz, March 1993. (No proc.)

[88] A. Wenzel, "Ein Szintillatorhodoskop mit WLS-Faser-Auslese für das Hyperonenstrahlexperiment WA89 am CERN," diploma thesis, Universität Heidelberg (1992).
M. Beck *et. al.*, "A Scintillating Tile Hodoscope with WLS Fibre Readout," MPIH-V22-1994 (1994) (submitted to *Nucl. Instr. and Meth.*).

Summary

Particle physics is the study of the fundamental constituents of matter and the forces that hold them together. Experimentally, this is accomplished by colliding particles at high energy and detecting the particles coming out of the collision. Specially-designed instruments are used to detect (usually by electronic means) these particles. Developing and building detectors form an important area of particle physics research.

The Spaghetti Calorimeter (SPACAL) is a detector intended primarily for the energy measurement of high-energy particles, but also provides spatial information and particle identification. It is a sampling calorimeter composed of plastic scintillating fibers, oriented in the direction of the particle, embedded in lead. The scintillation light is read out by photomultipliers, which are coupled to bunches of fibers through light guides, each forming a tower. It was developed as an electromagnetic (e.m.) and compensating hadronic calorimeter for use in future multi-TeV collider experiments. The largest prototype was installed for an alternative application as an hadronic calorimeter in the WA89 experiment, where it is used for the detection of neutrons resulting from Σ^- decays.

A calorimeter is an instrumented block of matter that absorbs the energy of a particle and produces an observable signal, which provides a measure of this energy. It consists of a material (such as lead) in which a particle interacts and loses its energy by producing a shower of more and more particles of lower energies. In a sampling calorimeter, part of this energy is deposited in an active material (such as scintillator), which produces the signal. This signal is proportional to the particle energy for an e.m. shower, initiated by electrons and photons.

The showering process for hadrons is quite different. In particular, the energy spent on nuclear breakup shows large fluctuations, and it is not visible to the calorimeter. However, there is a correlation between this energy and the production of low energy neutrons. It the active material has a suitable response to these neutrons, the fluctuations no longer degrade the resolution on the energy measurement. Optimal resolution is obtained if the hadronic energy loss is "compensated" for in a such a way that electrons and hadrons of equal energy give equal response, *i.e.*, $e/h = 1$.

Several techniques are used to obtain a compensating calorimeter. Hydrogenous materials, such as scintillator, have a high cross-section for neutron collisions, therefore producing a higher response to the non-e.m. part of the shower. The volume ratio of lead to scintillator necessary to achieve compensation is 4:1. These and other basic

concepts behind calorimetry are discussed in detail in chap. 2.

Such a small amount of sampling material in a compensating lead and scintillator calorimeter results in high sampling fluctuations. When scintillating fibers are used instead of plates, the sampling frequency increases while the total amount of active material is maintained. In this way, sampling fluctuations are reduced, and the energy resolution (particularly for e.m. showers) is improved. This was the motivation for e.m. fiber calorimeters. With the Spaghetti Calorimeter geometry, the fibers run almost parallel to the particle direction. The calorimeter can therefore be made hermetic by having all the readout in the back. In addition, the use of fibers allows fine granularity needed for good position resolution.

In order to keep instrumental contributions to the energy resolution at a minimum, the scintillating fibers must have the following features. High uniformity from fiber to fiber within a tower is necessary to maintain good e.m. energy resolution. In addition, the fibers should have a large attenuation length in order to limit the effects of fluctuations in shower depth, which contribute to the hadronic energy resolution. SCSF38 fibers were chosen to meet these requirements as best as possible, and their properties were extensively measured. These results are included in chap. 3.

Several prototypes were tested in beams of electrons and pions with energies up to 150 GeV. Reasonable e.m. energy resolution, at $\sigma/E = 12.9\%/\sqrt{E[\mathrm{GeV}]} + 1.23\%$, was measured. Excellent hadronic energy resolution was found, at $30.6\%/\sqrt{E[\mathrm{GeV}]} + 1.0\%$, but the calorimeter was found to be slightly undercompensating, with $e/h = 1.15$. The position of the shower barycenter for both electrons and pions was easily found according to the relative energy deposits in the calorimeter towers. The calorimeter was also found to be able to provide effective discrimination between electrons and hadrons. This is most commonly done by exploiting the differences in the lateral shower dimensions, but the longitudinal shower information may also be utilized through the signal time structure. These results and more are presented detail in chap. 4.

The performance of SPACAL in the WA89 experiment at the Omega spectrometer at CERN was studied with the reconstruction of beam Σ^- particles via its decay $\Sigma^- \rightarrow \mathrm{n}\pi^-$. These results are presented in chap. 5, in addition to details of the calibration of SPACAL with electrons and protons.

Samenvatting

De deeltjesfysica houdt zich bezig met de studie van de fundamentele bouwstenen van de materie en de krachten daartussen. Experimenteel wordt dit bereikt door deeltjes bij hoge energie te laten botsen en de deeltjes die uit de botsing tevoorschijn komen te detecteren. Speciaal ontworpen instrumenten worden gebruikt om deze deeltjes (gewoonlijk met elektronische middelen) te detecteren. Ontwikkeling en bouw van detectoren vormen een belangrijk terrein van onderzoek in de deeltjesfysica.

De Spaghetti Calorimeter (SPACAL) is een detector die in de eerste plaats bedoeld is voor de meting van de energie van hoogenergetische deeltjes, maar verschaft ook ruimtelijke informatie en deeltjesidentificatie. Het is een 'sampling' calorimeter samengesteld uit scintillerende plastic fibers, geörienteerd in de richting van het deeltje, gevat in lood. Het scintillatielicht wordt uitgelezen via photomultiplicatoren, die via lichtgeleiders gekoppeld zijn aan fiberbundels, die ieder een 'toren' vormen. SPACAL is ontwikkeld als een elektromagnetische (e.m.) en compenserende hadronische calorimeter voor gebruik in toekomstige experimenten met multi-TeV botsende bundels. Het grootste prototype werd geïnstalleerd voor een alternatieve toepassing als hadronische calorimeter in experiment WA89, waar het gebruikt is voor de detectie van neutronen afkomstig van Σ^- verval.

Een calorimeter is een geïnstrumenteerd blok materiaal dat de energie van een deeltje absorbeert en een waarneembaar signaal produceert, dat een maat is voor deze energie. In het materiaal (zoals lood) interageert het deeltje en verliest het energie door een sproeier ('shower') van meer en meer deeltjes van lagere energie te produceren. In een 'sampling' calorimeter wordt een deel van deze energie afgegeven in een actief materiaal (zoals scintillator), waarin het signaal wordt geproduceerd. Dit signaal is evenredig met de energie van het deeltje in het geval van een e.m. 'shower', geïnitieerd door elektronen en fotonen.

Het ontstaan van een hadronische 'shower' verloopt anders. In het bijzonder zijn er grote fluctuaties op de hoeveelheid energie die besteed wordt aan het splijten van kernen en die niet zichtbaar is in de calorimeter. Er bestaat echter een correlatie tussen deze energie en de productie van laag energetische neutronen. Indien het actieve materiaal een geschikte respons geeft op deze neutronen, veroorzaken de fluctuaties niet langer een verslechtering van de energiemeting. Een optimale resolutie wordt verkregen als het hadronische energieverlies wordt 'gecompenseerd' en wel op zodanige wijze dat elektronen en hadronen van gelijke energie gelijke respons geven, d.w.z. $e/h = 1$.

Diverse technieken worden gebruikt om een compenserende calorimeter te verkrijgen. Waterstofrijke materialen, zoals scintillator, hebben een hoge werkzame doorsnede voor neutronbotsingen en produceren daardoor een hogere respons voor het niet-e.m. deel van de 'shower'. De verhouding van de volumes van lood en scintillator nodig om compensatie te bereiken is 4:1. Deze en andere basisconcepten ten grondslag liggend aan calorimetrie worden in detail besproken in hoofdstuk 2.

Een zo kleine hoeveelheid actief materiaal in een compenserende lood-scintillator calorimeter kan resulteren in grote statistische ('sampling') fluctuaties. Indien scintillerende fibers worden gebruikt in plaats plakken van scintillator, wordt de 'shower' vaker bemonsterd bij gelijke hoeveelheid actief materiaal. Op deze wijze worden statistische fluctuaties onderdrukt en de energieresolutie (in het bijzonder voor e.m. 'showers') verbeterd. Hierin ligt de motivatie voor e.m. fiber calorimeters. In de SPACAL lay-out lopen de fibers vrijwel parallel aan de deeltjesrichting. Het is daarom mogelijk de calorimeter hermetisch te maken door de uitlezing aan de achterkant te situeren. Bovendien maakt het gebruik van fibers een fijne granulariteit mogelijk, die nodig is voor een goede ruimtelijke resolutie.

Om de instrumentele bijdragen aan de energieresolutie tot een minimum te beperken, moeten de scintillerende fibers de volgende kenmerken hebben. Hoge uniformiteit van fiber tot fiber binnen een 'toren' is noodzakelijk voor een goede e.m. energieresolutie. Bovendien moeten de fibers een grote verzwakkingslengte hebben om effecten van fluctuaties in 'shower' diepte te beperken, die bijdragen aan de hadronische energieresolutie. SCSF38 fibers werden gekozen om aan deze eisen zo goed mogelijk tegemoet te komen, en hun eigenschappen werden uitvoerig gemeten. De resultaten zijn opgenomen in hoofdstuk 3.

Diverse prototypes zijn getest in bundels van elektronen en pionen met energieën tot 150 GeV. Een redelijk goede e.m. energieresolutie van $\sigma/E = 12.9\%/\sqrt{E[\mathrm{GeV}]}+1.23\%$ werd gevonden. Een uitstekende hadronische energieresolutie van $30.6\%/\sqrt{E[\mathrm{GeV}]} + 1.0\%$ werd bereikt, maar de calorimeter bleek licht ondercompenserend, met $e/h = 1.15$. De positie van het zwaartepunt van de 'shower' van zowel elektronen als pionen werd gemakkelijk gevonden gebruikmakend van de relatieve energiedepositie in de calorimeter 'torens'. Ook bleek het mogelijk efficiënt onderscheid te maken tussen elektronen en hadronen. Gewoonlijk wordt dit gedaan door gebruik te maken van verschillen in laterale 'shower' afmetingen, maar het is ook mogelijk de longitudinale structuur van de 'shower' te benutten via de tijdstructuur van het signaal. Deze en andere resultaten worden in detail gepresenteerd in hoofdstuk 4.

De werking van SPACAL in het WA89 experiment bij de Omega spectrometer van CERN werd bestudeerd aan de hand van de reconstructie van Σ^- bundeldeeltjes via $\Sigma^- \rightarrow \mathrm{n}\pi^-$. Deze resultaten worden gepresenteerd in hoofdstuk 5, evenals details betreffende de calibratie van SPACAL met elektronen en protonen.

Acknowledgements

In the strange and wonderful world of high energy physics, most experiments are impossible without a large amount of international collaboration between researchers. My experience has been no exception. I have been involved with the Spaghetti Calorimeter, almost since its inception, when I arrived at CERN as a summer student in 1988. During my four years in Geneva, I worked on the SPACAL R&D project (as part of the LAA project) and on the SPACAL detector in the WA89 experiment. I did most of my research and some of the writing at CERN. Then I finished writing my thesis, after some fine tuning of my analysis, in Amsterdam at NIKHEF/H. During this time I have had the pleasure to meet and work with many people, some of whom I will try to acknowledge here. My apologies to those I have unwittingly forgotten to mention.

I am grateful Richard Wigmans for taking me on as a Ph.D. student and for supporting me in this work as an advisor, teacher, and colleague. Jos Engelen has been an outstanding advisor, both for his careful and constructive reading of this thesis and for dealing with many administrative difficulties. He also translated the summary into Dutch.

I am indebted to Riccardo DeSalvo, for introducing me to the world of high-energy physics at Cornell and then giving me the opportunity to come to CERN. I have learned much from him, especially on the hardware side of detector building. I was lucky to share an office in the famous LAA building with Lucie Linssen. I thank her for the fruitful discussions, useful comments on the manuscript, and for obtaining good copies of many figures for the printed version. On WA89, I worked most closely with Armand Simon. Much of the last chapter is the result of our many discussions and of his constructive comments on the manuscript.

I thank all my colleagues from the SPACAL project for the open exchange of information, helpful discussions, and the pleasant atmosphere. Without them, there wouldn't have been a Spaghetti Calorimeter. In particular, I have learned a lot from Luc Poggioli, Ana Henriques, and Manoel Seixas.

My work in WA89 had its base in equipment, software and personal effort provided by members of the collaboration. I thank all my colleagues for the smooth experimental run in 1991. The beam tests for the calorimeter calibration went as smoothly as they possibly could due to the hard work and persistence of Karl-Heinz Brenziger and Alexander Wenzel. The work on SPACAL in WA89 continues in the able hands

of Thomas Haller and Mathias Beck, with whom I have had useful discussions of results since I left CERN. I also thank Bob Michaels for helping me get set up in the WA89 analysis programs and for his helpful suggestions when I got stuck. The color coordination of Elisabeth Albertson brightened up the work in WA89, as did our numerous discussions about the experiment, physics, computers, and life. Her endless supply of tea and cookies also helped to sustain me through many evenings of work.

Life at CERN mixes work with pleasure in a unique, stimulating environment. Therefore, many of my friends provided practical support for my work, as well as moral support. I am grateful to Dan Hubbard, for sharing his expertise with PAW, and for being a source of all knowledge (and not a bad frisbee player either). I appreciate the discussions with and encouragement from Pratibha Vikas. Many thanks to my Ultimate frisbee collaborators for keeping me running. I also thank Randy Mantooth & the Jaws of Life, for sanity (and a lot of insanity, too) through music. My collaboration with physicists (and others) from the former Soviet Union, as directed by Victor Kim, was also a source of motivation. I appreciate the encouragement I received from Bernie Sutton. My first few years at CERN would have been difficult and much less pleasant without the unflagging support and friendship of Dave Parrott. I thank Hal Evans, for answering many questions on physics and English usage and for sharing many wonderful dinners.

The helpful administrative and computer staff at NIKHEF helped me settle in and get working. Without a group of my own, I relied on colleagues from all the experiments for discussions and support. I am grateful to Nichol Brümmer for, among other things, many fruitful discussions on physics and the mysteries of LaTeX, for the use of his style file, and for the valuable discussions about kinematic fitting.

While in Amsterdam, my many friends made my stay here much more than bearable (and provided occasional computer support as well). I wish to thank Sjoerd Mullender especially, for his help with the final layout of this thesis and for unraveling some of the mysteries of Unix and of Dutch language and culture for me. Also, I thank Aly Syed for his sympathetic ear and good company in both Geneva and the Netherlands.

The cover of this thesis was made possible by the amazing efforts of Zhang Dehong, who also improved many of the PostScript figures. Robert van Liere also gave valuable input into the design and production of the cover.

Mostly, I would like to thank my family for believing in me and for giving me the confidence to finish this work, even though they have only a vague idea of what I'm doing.